ALMA MATER STUDIORUM - UNIVERSITÀ DI BOLOGNA

FACOLTÀ DI CHIMICA INDUSTRIALE

Dipartimento di Chimica Industriale e dei Materiali

Master of Science in Advanced Spectroscopy in Chemistry

Classe LM/71 - Scienze e Tecnologie della Chimica Industriale

NEW CATALYSTS FOR THE WATER GAS SHIFT REACTION AT MIDDLE-TEMPERATURE

EXPERIMENTAL THESIS

Presented by

TRAN Quang Nguyen

Supervisor:

Prof. Angelo Vaccari

Co-Supervisors:

Dr. Giuseppe Brenna

Dr. Matteo Paris

First Session

Academic Year 2011-2012

CONTENTS

Aim of the work

H_2 demand is continuously increasing since its many relevant applications, for example, the ammonia production or the refinery processes. Moreover, H_2 may also be used as an energy carrier for fuel cells, which convert it to produce electricity and heat. Its industrial production exceeded 550 billion Nm^3/y in 2010, mainly from steam reforming and cracking of heavy oils, while a smaller part from gasification of coal and electrolysis of water.

The <u>W</u>ater <u>G</u>as <u>S</u>hift (WGS) reaction ($CO + H_2O$ " $CO_2 + H_2$ r H = -41.1 kJ.mol^{-1}) is a step in the H_2 production, reducing significantly the CO content in the gas mixtures obtained from steam reforming and increasing the H_2 content. Industrially, the reaction is carried out in two stages with different temperature: the first stage operates at high temperature (350-450 °C) using Fe-based catalysts, while the second one is performed at lower temperature (190-250 °C) over Cu-based catalysts. However, recently, an increasing interest emerges to develop new catalytic formulations, operating in a single-stage at middle temperature, while maintaining optimum characteristics of activity and stability. These formulations may be obtained by improving activity and selectivity of Fe-based catalysts, or increasing thermal stability of Cu-based catalysts.

In the present work, Cu-based catalysts ($Cu/ZnO/Al_2O_3$) were prepared from hydrotalcite-type (HT) precursors, which are able to provide catalysts with high surface area, chemical homogeneity, and small crystal size. The catalysts with various compositions were investigated by studying their physical properties, WGS activity and stability, in order to evidence optimum composition for the reaction at middle temperature and the role of each component on the catalytic performances.

4

1.   Introduction

According to the International Energy Agency (IEA) in 2009, the Total Primary Energy Supply (TPES) was dominated by 80.9 % of fossil fuels, 2.3 % of hydro, 10.2 % of biofuels and waste, 5.8 % of nuclear, and a small amount of other sources (Fig. 1.1). Hydro-energy demand was continuously increasing from 1.8 % in 1973 to 2.3 % in 2009 [1].

(*Other includes geothermal, solar, wind, heat, etc.)
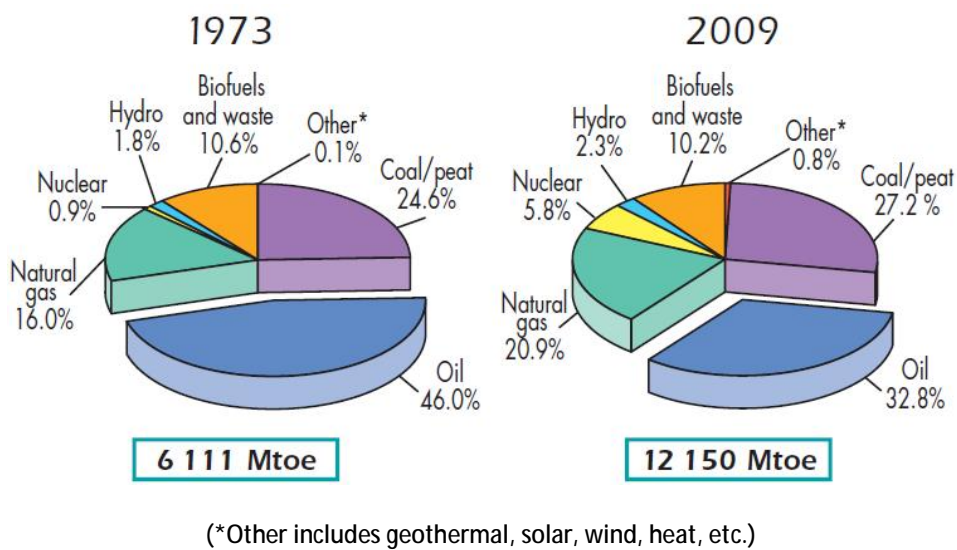
Figure 1.1 1973 and 2009 fuel shares of TPES [1].

Synthesis gas (syngas) is a mixture of H_2 and CO in various compositions, corresponding to specific applications. Syngas can be produced by coke and biomass gasification, steam reforming [2] or partial oxidation of hydrocarbons [3], usually natural gas. Syngas has been employed to produce ammonia [2,4–12] and methanol [13–16], but is also used to prepare synthetic petroleum to be used as a fuel or lubricant via the Fischer–Tropsch or the Mobil methanol to gasoline processes [11,17–20]. Furthermore, H_2 is a building block product of remarkable industrial interest and is claimed to replace hydrocarbons and provide a clean fuel without carbon oxide emissions, to be used in stationary and mobile applications as well (Fig. 1.2).
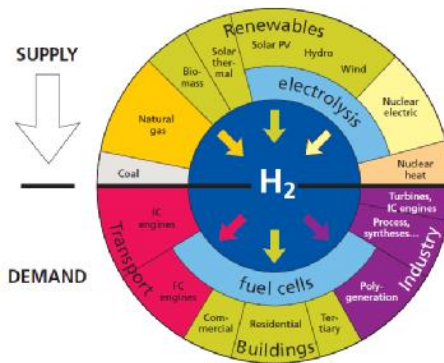
Figure 1.2 Hydrogen: primary energy sources, energy converters and applications (size of "sectors" has no connection with current or expected markets) [26].

Nowadays, worldwide production of H_2 exceeded 550 billion Nm^3/y in 2010, of which about 60 % by reforming of light fractions of hydrocarbons, 30 % by cracking of heavy oils, 7 % by gasification of coal, and 3 % by electrolysis of water. Steam reforming of natural gas is the main source of H_2 production, while some of the others still in laboratory phase, with small scale production by steam reforming [2] and/or gasification of biomasses, possibly in combination with electrolysis [3].

In the chemical industry, about 50 % of H_2 produced in the world is used for the ammonia synthesis, while the demand of the refinery, including hydro-treatment and hydro-cracking (Table 1.1), is continuously increasing to respect the stringent regulations (about 37 % of the H_2 production) [2,21,22]. Further uses are the methanol and light hydrocarbons production (about 5 %) and the production of plastics and reduced metals (Fig. 1.3) [2,23].

Figure 1.3 Hydrogen role in the chemical industry [1].

Table 1.1 Hydrogen consumption in the main hydrotreating and hydrocracking processes [2].

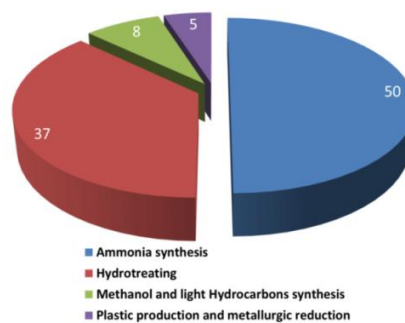| PROCESS	MAIN AIM OF TREATMENT	CONSUMPTION (Kg_{H2}/tonn$_{feed}$)
HYDROTREATING		
Hydrotreating of gasoline	Elimination of poisons (mainly sulphur and nitrogen) for the reforming and isomerisation catalysts. Compliance with the specifications related to sulphur content in gasolines	0.5-10.0
Hydrodesulphurization of kerosene	Compliance with specifications related to sulphur content in middle distillates	1.0-3.0
Hydrodesulphurization of diesel	Compliance with specifications related to sulphur content in middle distillates	3.0-12.0
Hydrotreating of middle distillates	Pre-treatment of feedstock for the upgrading processes, such as FCC (Fluid Catalytic Cracking) and hydrocracking	5.0-15.0
Dearomatization	Compliance with the specifications related to aromatic content in various fractions (for example in middle distillates)	3.0-15.0
HYDROCRACKING		
Conversion of middle distillates	Conversion of heavy vacuum fractions into lighter products such as LPG, virgin naphtha, kerosene, diesel (upgrading of the feed)	15.0-25.0
Hydrotreating and conversion of fuel oils	Reduction of content of undesired elements (metals, sulphur, nitrogen, etc.) to improve the quality of fuel oil. Partial upgrading of the residue to be fed	10.0-25.0

Actually, H_2 interest is due to its application for fuel cells [24,25] that convert it to produce electricity and heat. Fuel cells are able to achieve efficiencies of about 60% compared to 33-35% of electricity generation plants by combustion [10]. Various types of fuel cells are described in the Table 1.2.

Table 1.2 Summary of fuel cell types [24].

FUEL CELL	PEMFC	AFC	PAFC	MCFC	SOFC
Electrolyte	Ion-exchange membrane	$KOH_{(aq)}$ in solid asbestos	H_3PO_4	Li_2CO_3/K_2CO_3	ZrO_2-Y_2O_3
Temperature [°C]	70-90	120-250	180-230	650-700	800-1000
Transmitted charge	H^+	OH^-	H^+	CO_3^{2-}	O^{2-}
Anode catalyst	Pt	Non-noble metals (i.e. Ni)	Pt	Ni	Ni
Fuel	H_2	H_2	H_2	Reformate, CO/H_2	Reformate, CH_4, CO/H_2

The development of H_2 production technologies requires the identification of the potential markets and the constraints associated with them; existing and potential H_2 markets may be identified as follows [11]:

- Industrial: the main industrial markets for H_2 are fertilizer production (ammonia), steel, methanol and H_2 for cracking and hydrodesulphurization.

- Vehicles: transportation requirements may be met by different fuels (methanol, dimethyl ether, Fischer-Tropsch fuels or gasoline, diesel, jet fuel and, in the future, H_2 itself).

- Power: H_2 is a candidate for power production, mainly as a vector for storage and use to produce when necessary.

- Commercial: H_2 is being considered for commercial applications in the buildings, by the co-generation of power and heat.

References

[1]   IEA, *Key World Energy Statics*, International Energy Agency, Paris (F), 2011.

[2]   M. di Luozzo, *Encyclopaedia of Hydrocarbons*, Treccani, Milano (I), 2006.

[3]   B. van Ruijven, D.P. van Vuuren, B. de Vries, *Int. J. Hydr. En.* 32 (2007) 1655.

[4]   A. Hellman, K. Honkala, I.N. Remediakis, Á. Logadóttir, A. Carlsson, S. Dahl, C.H. Christensen, J.K. Nørskov, *Surf. Sci.* 600 (2006) 4264.

[5]   M.V. Twigg, *Catalyst Handbook*, Wolfe, London (UK), 1996.

[6]   C. Liang, Z. Wei, Q. Xin, C. Li, *Appl. Catal.* A 208 (2001) 193.

[7]   S.M. Yunusov, E.S. Kalyuzhnaya, B.L. Moroz, A.S. Ivanova, T.V. Reshetenko, L.B. Avdeeva, V.A. Likholobov, V.B. Shur, *J. Mol. Catal. A: Chemical* 219 (2004) 149.

[8]   Q.-C. Xu, J.-D. Lin, J. Li, X.-Z. Fu, Z.-W. Yang, W.-M. Guo, D.-W. Liao, *J. Mol. Catal. A: Chemical* 259 (2006) 218.

[9]   P. Seetharamulu, V. Siva Kumar, A.H. Padmasri, B. David Raju, K.S. Rama Rao, *J. Mol. Catal. A: Chemical* 263 (2007) 253.

[10]   N.N. Greenwood, A. Earnshaw, *Chemistry of the Elements*, Butterworth-Heinemann, Oxford (UK), 1998.

[11]   C.W. Forsberg, *Int. J. Hydr. En.* 32 (2007) 431.

[12]   S.A. Noe, US Patent 4,735,780 (1998) to Kellogg M. W.

[13]   X.-M. Liu, G.Q. Lu, Z.-F. Yan, J. Beltramini, *Ind. Eng. Chem. Res.* 42 (2003) 6518.

[14]   T.V. Choudhary, D.W. Goodman, *J. Mol. Catal. A :Chemical* 163 (2000) 9.

[15]   F.J. Keil, *Microp. Mesop. Mater.* 29 (1999) 49.

[16]   M. Stöcker, *Microp. Mesop. Mater.* 29 (1999) 3.

[17]   A.D. Klerk, WO Patent 144,782 (2008) to Sasol Tech.

[18]   J. V. Berge, S. Loosdrecht, J. V. D. Barradas, WO Patent 012,008 (2003) to Sasol Tech.

[19]   M. Krumpelt, T.R. Krause, J.D. Carter, J.P. Kopasz, S. Ahmed, *Catal. Today* 77 (2002) 3.

[20]   P.L. Spath, D.C. Dayton, *Preliminary Screening - Technical and Economic Assessment of Synthesis Gas to Fuels and Chemicals with Emphasis on the Potential for Biomass-Derived Syngas*, Technical report, National Renewable Energy Laboratory, Colorado (USA), 2003.

[21]   M.F. Alì, B.M.E. Alì, J.G. Speight, *Handbook of Industrial Chemistry*, Mcgraw-Hill, New York (USA), 2005.

[22]   I.V. Babich, J.A. Moulijn, *Fuel* 82 (2003) 607.

[23]   A.I. Molina, *Catalizadores de cobalto soportados sobre sòlidos mesoporosos para reacciones de hidrotratamiento*, PhD Thesis, Malaga University (E), 2006.

[24]   J.H. Hirschenhofer, D.B. Stauffer, R.R. Engleman, M.G. Klett, *Fuel Cell Handbook*, U.S. Department of Energy, Federal Energy Technology Center, West Virginia (USA), 1998.

[25]   C. Song, *Catal. Today* 77 (2002) 17.

2. Water Gas Shift Reaction

2.1 General

The <u>W</u>ater-<u>G</u>as <u>S</u>hift (WGS) reaction (equation 2.1) is an important step in the industrial production of H_2, used to remove the CO produced in gas reforming and increase H_2 content by reaction with steam to form CO_2 [1]. Currently, H_2 produced by this reaction may be applied for ammonia synthesis, Fischer–Tropsch synthesis and fuel cell systems.

$$CO \ + \ H_2O \ D \ H_2 \ + \ CO_2 \qquad\qquad \Delta H = \text{-41.1 kJ.mol}^{-1} \qquad\qquad (2.1)$$

The WGS reaction is slightly exothermic, with an equilibrium constant that decreases as the temperature increases, high conversions being favored at low temperatures (Fig. 2.1). The equilibrium constant dependence on temperature may be calculated by different equations described in Table 2.1 [1–3].
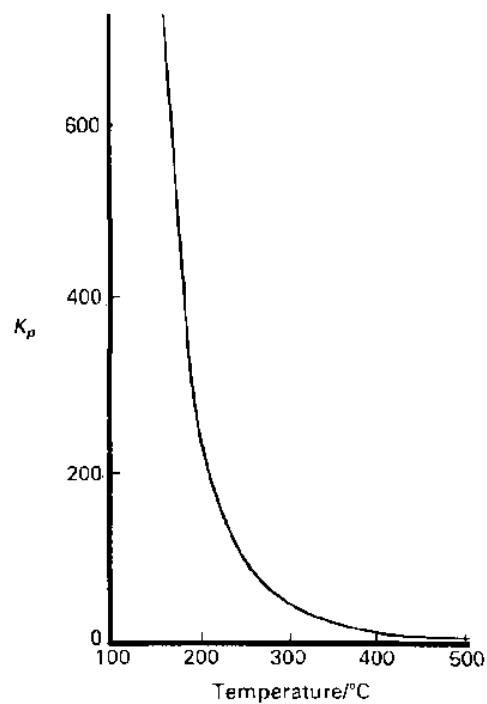

Figure 2.1 Equilibrium constant (Kp) as a function of the temperature for the WGS reaction [1].

Table 2.1 Equilibrium constant for the WGS reaction.

Equilibrium constant: $K_{eq} \cong \dfrac{P_{CO_2} P_{H_2}}{P_{H_2O} P_{CO}}$	Ref.	
$K_{eq} = \exp(T(T(0.63508-0.29353Z)+4.1778)+0.31688)$	[1]	(2.2)
$\ln(K_{eq}) = 5693.5/T + 1.077 \ln T + 5.44 \times 10^{-4} T - 1.125 \times 10^{-7} T^2 - 49170/T^2 - 13.148$	[2]	(2.3)
$K_{eq} = \exp(4577.8/T - 4.33)$	[3]	(2.4)

where T (K) is temperature

Under adiabatic conditions, as the reaction proceeds the released heat increases the reaction temperature and, therefore, restricts the CO conversion, achieving the exit CO level at single converter in a range from 2 to 4 vol.%. In order to reduce the thermodynamic limitations, two or more beds with inner bed cooling are used, may be with removal of CO_2 between the stages. In this way, CO level can achieve less than 1 vol.%. Therefore, the limitation of CO conversion depends on catalyst activity [1].

A significant improvement in CO conversion may be obtained by applying two-bed system, with the second bed operating at lowest possible temperature (about 200 °C). Industrially, the reaction is performed in two stages with different temperatures to achieve a desired CO content for further applications: i) the first stage employs Fe-based catalyst in a range of 350-450 °C and is known as High Temperature Shift (HTS); ii) the second one is performed at lower temperature (190-250 °C) over Cu-based catalysts (Low Temperature Shift or LTS). This is explained by the fact that the shift reaction is thermodynamically favored at low temperature and kinetically at high temperature. Secondly, Fe-based catalysts are active at high temperature and resistant to poisons, while Cu-based catalysts operate only at lower temperature due to sintering tendency of active phase. So, it is necessary to lower the temperature of process gas at outlet of HTS converter from 400 to about 200 °C, in which Cu-based catalysts operate effectively, by using heat-exchange systems between converters [1]. As shown in figure 2.2, the two-stage system may reduce CO content to less than 0.3 vol.%, lower than that in the single-stage (CO conc. > 1 vol.%). However, recently, there is an increasing interest to develop

new Cu-based catalysts to carry out the process in intermediate temperature at 250-350 °C (Middle Temperature Shift or MTS) in order to decrease operation cost.
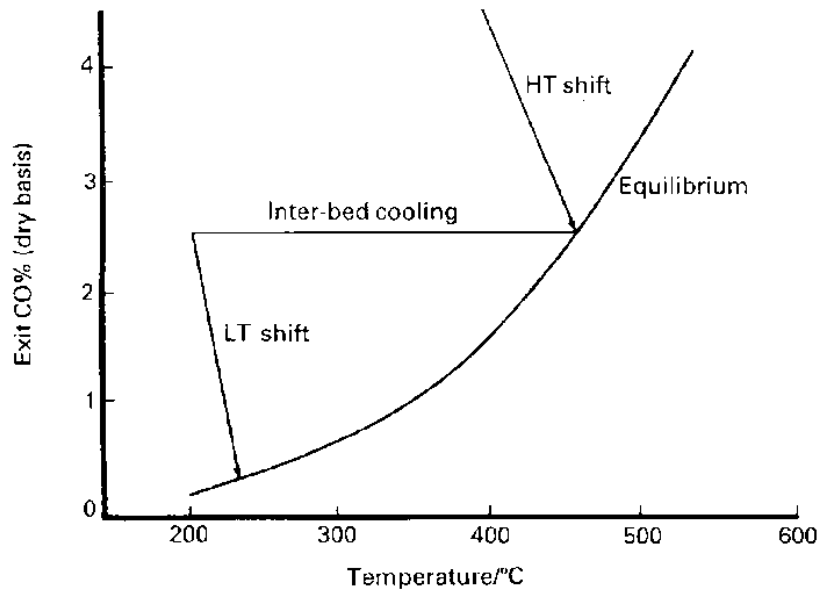

Figure 2.2 Typical variations of CO levels in HTS and LTS catalyst beds [1].

2.2   Kinetics and mechanism

The mechanism of shift reaction remains in dispute for both Cu- and Fe-based catalysts. In general, two mechanisms have been derived and are known as "adsorptive" and "regenerative (or redox)". The WGS reaction involves the H_2O dissociation that may occur on the metal, the support or both. Similarly, the CO may react with the O-containing species (H_2O, OH or O) of the gas phase, adsorbed state or surface lattice [1].

In the "regenerative" mechanism, adsorption and splitting of H_2O molecules to H_2 gas and oxygen atoms occur on the catalyst surface. The oxygen atoms still adsorbed on catalyst sites react with CO to produce CO_2 (Fig. 2.3) as described in equations (2.5) and (2.6). In the conventional "redox" mechanism, the dissociation of H_2O and the production of H_2 occur separately, however, Callaghan et al. [4] suggested modified "redox" mechanism for Cu-based catalysts, in which the production of both O and H_2 takes place in a single-step. Furthermore, the Rate Determining Step (RDS) critically depends on

12

composition of feed gas [5], catalysts [3,6], reaction conditions such as pressure [7], and temperature [7,8].

$$H_2O \ + \ * \ \rightleftharpoons \ H_2 \ + \ O_{(a)} \tag{2.5}$$

$$CO \ + \ O_{(a)} \ \rightleftharpoons \ CO_2 \ + \ * \tag{2.6}$$

where $*$ is a vacant site.

In the "adsorptive" mechanism, it is assumed that the two reactants (CO and H_2O) are first adsorbed on the catalyst surface and react to form surface intermediates, such as formate (HCOO), carboxyl (HOCO) species, following the decomposition to products and desorption from the surface (Fig. 2.3) [1]. Supporting the formate intermediate mechanism, some authors [8,9] concluded that formate decomposition is RDS for Cu-based catalysts. Moreover, Shido and Iwasawa [10,11] confirmed that the WGS reaction on ZnO catalytically proceeds through bidentate and bridge formates converted to products, or unidentate carbonates in absence of H_2O. On the other hand, some authors [12–16] supposed that surface carboxylic species are the dominant intermediates of the WGS reaction, fitting the previous experimental results [8,17] to confirm that there is no possibility of formation of formate intermediates on Cu(111). In recent years, other authors [18,19] showed that the carboxyl intermediate formed from adsorbed OH and surface CO reacts with another adsorbed OH to give CO_2. Such as in the "redox" mechanism, the RDS depends on reaction conditions, specifically the temperature, H_2O concentration [20–23], and pressure [7,12].

The rate of the reaction depends on various parameters including: catalyst properties and reaction conditions such as operating temperature, pressure, and the composition of feed gas. Therefore, there is a large number of mechanistic models and rate equations for the WGS reaction [1]. Langmuir-Hinshelwood (LH) models (equation 2.7 and 2.8) suggest "adsorptive" mechanism with intermediate formation to better describe the WGS kinetics for a wide range of temperature and have a good fitting with the experimental results [24–26]. Furthermore, Ayastuy and Amadeo [25,27] reported that

the LH model is the best one describing the kinetics of the LTS reaction over commercial Cu/ZnO/Al$_2$O$_3$ catalyst. Moreover, in 2011, by using Computation Fluid Dynamic (CFD) for different models of rate expressions, Smith et al. [28] confirmed that LH models are able to predict the CO conversion with minimum deviation from the experimental results. In the "redox" mechanism, H$_2$O dissociation on reduced sites is assumed to be RDS and the rate equations (equation 2.9 and 2.10) for this model are described in Table 2.2 [29,30].

In contrast to rate expressions obtained from detailed reactions, the empirical reaction rate models (equations 2.11-2.13) do not consider any mechanisms, but they are useful for reactor design and optimization. However, these models are only valid for concentration and temperature ranges in which the kinetic studies have been carried out [3,7,26,27,31]. In 2005, Choise and Stenger [32] suggested an empirical rate expression (equation 2.13) fitting experimental data with a high degree of accuracy.
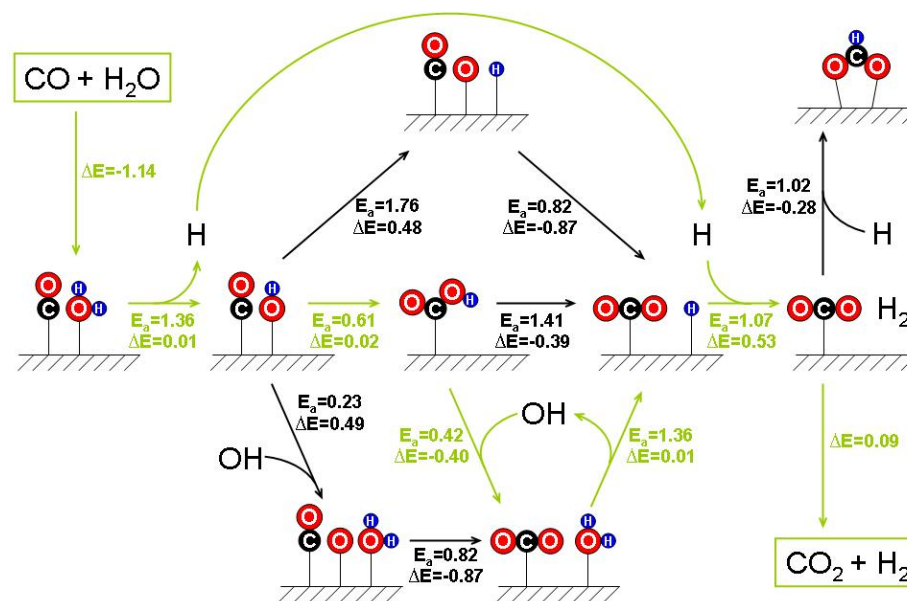

Figure 2.3 Reaction scheme including both the "redox" and the "adsorptive" (carboxyl) mechanism (steps in eV). Minimum energy pathway for the WGS reaction is highlighted with light grey.

Table 2.2 Model kinetic equations for the WGS reaction.

Model	Rate equation	Ref.	
Langmuir-Hinshelwood	$$r_{CO} = k \frac{P_{CO}P_{H_2O} - P_{CO_2}P_{H_2}/K_e}{\left(1 + K_{CO}P_{CO} + K_{H_2O}P_{H_2O} + K_{H_2}P_{H_2} + K_{CO_2}P_{CO_2}\right)^2}$$	[7]	(2.7)
	$$(-r_{CO}) = \frac{k(P_{CO}P_{H_2O} - \dfrac{P_{CO_2}P_{H_2}}{K_e})}{(1 + K_{CO}P_{CO} + K_{H_2O}P_{H_2O} + K_{CO_2}P_{CO_2}P_{H_2}^{0.5} + K_{H_2}^{0.5}P_{H_2}^{0.5})^2}$$		(2.8)
Redox	$$r_{CO} = k \frac{P_{H_2O} - P_{CO_2}P_{H_2}/K_e P_{CO}}{1 + K_{CO_2}\dfrac{P_{CO_2}}{P_{CO}}}$$	[29]	(2.9)
	$$r_{CO} = k \frac{K_{CO}K_{H_2O}\left(P_{CO}P_{H_2O} - P_{CO_2}P_{H_2}/K_e\right)}{K_{CO}P_{CO} + K_{H_2O}P_{H_2O} + \left(K_{CO_2} + K_{H_2}\right)P_{CO_2}}$$	[30]	(2.10)
Power-law	$$r_{CO} = k\left(P_{CO}P_{H_2O} - P_{CO_2}P_{H_2}/K_e\right) = kP_{CO}P_{H_2O}(1-b)$$	[3]	(2.11)
	$$r_{CO} = kP_{CO}^a P_{H_2O}^b P_{H_2}^c P_{CO_2}^d (1-b)$$	[9]	(2.12)
	$$(-r_{CO}) = 2.96.10^5 \exp(-\frac{47400}{RT})(p_{CO}p_{H_2O} - \frac{p_{CO_2}p_{H_2}}{K_e})$$	[13]	(2.13)
	where $\quad b = P_{CO_2}P_{H_2}/P_{CO}P_{H_2O}K_e$	[3,9]	(2.14)
	$$k = 1.85.10^{-5}\exp(12.88 - \frac{1855.5}{T})$$	[3]	(2.15)

Nomenclature

(r_{CO})	reaction rate
k	rate constant for the WGS reaction
K_e	equilibrium constant
K_i	equilibrium adsorption constant of species i
p_i	partial pressure of species i
a, b, c, d	reaction orders of the components CO, H_2O, H_2 and CO_2
T(K)	temperature
R	gas constant R= 8.3145 J/mol·K

2.3   Reactors

A single-bed adiabatic shift reactor is often used, either in HTS or LTS units to minimize thermodynamic limit of the WGS reaction. However, multi-bed catalyst shift reactor (Fig. 2.4) is employed where the outlet gas from the first unit is cooled down to suitable temperature by heat-exchange system [33]. Some companies proposed radial flow reactor which allows to use catalyst with small dimensions of grains, with minimized charge losses. This is particularly advantageous for the big installations, to limit catalyst volume and reactor size.
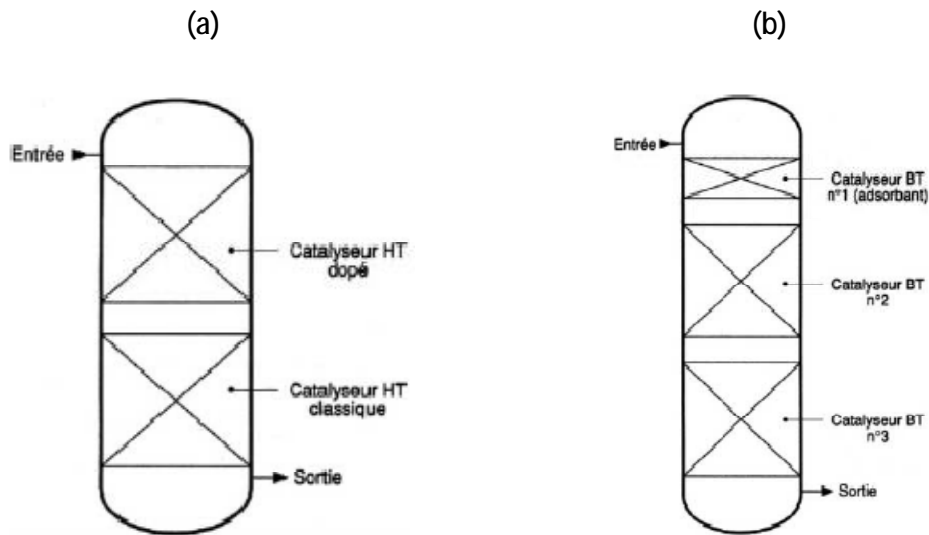

Figure 2.4 Adiabatic HTS (a) and LTS (b) converters [33].

More recently, Membrane Reactors (MR) (Fig. 2.5) have been used to combine reaction and separation processes in a single-step. The MR consists of a multi-tubular device, where the catalytic bed can be situated inside or outside the tubes. The tubes are constructed in a composite material formed by different layers, one of them being selective for the permeation of H_2. It is reported that Pd-based membranes are the most permeable and selective to H_2 [33–37]. Pd-based MR show satisfactory performance also at a high Gas Hourly Space Velocity (GHSV) values, achieving a CO conversion at least three times higher than traditional reactors [39]. Among Pd-based MR, Pd-Ag alloy is

considered as a potential candidate for WGS due to relatively high H_2 permeability, good separation selectivity, high mechanical integrity and hydrothermal stability [39–41].
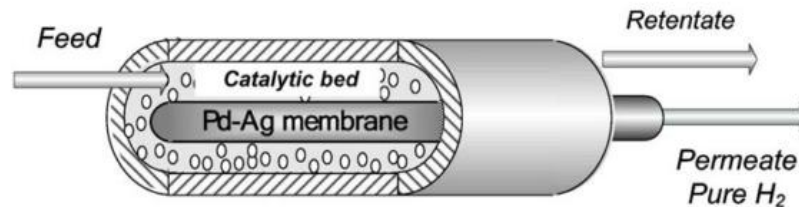

Figure 2.5 Scheme of tube in a tube membrane reactor [39].

2.4 Catalyst formulations

2.4.1 Commercial catalysts

2.4.1.1 HTS formulations

In industrial plants, Fe-based catalysts have been used in high temperature converter due to their high activity, thermal stability and poison resistance. Operating conditions are: T=350-450 °C, P = 1-80 atm. The temperature must be minimized to obtain desired CO conversion, resulting in an increase in catalyst life by limiting the sintering. The catalysts operate also with a wide range of <u>S</u>team/<u>D</u>ry <u>G</u>as (S/DG) ratios and with moderately high impurity level. In fact, Fe-based catalysts are not very sensitive to poisoning by sulphur, which is commonly present in feed gas derived from coal or fuel oil. The Fe-based catalysts may work with high CO inlet concentration [1].

Catalyst site is considered to be the spinel of magnetite Fe_3O_4 or $FeO \cdot Fe_2O_3$. A small amount of added Cr increases thermal stability and Fe dispersion in the catalyst, since the Cr substitution in Fe oxide lattice improves the Fe distribution and as well as the catalyst activity [43]. Fe-Cr oxide catalysts have been used industrially in HTS unit and generally higher content of Cr leads to higher resistance to the sintering, but with reduction of activity, thus a Cr-content of 8 wt.% is a good compromise [44]. They are usually prepared by precipitation of aqueous solution of Fe and modifier (for instance, Cr)

salts by a base, preferably an alkali metal aqueous solutions, hydroxide or carbonate, to improve the homogeneity of the precipitate composition. Sulfate salts are preferred due to their availability and low cost. The precipitation is carried out at 30-80 °C and a pH of 6-9, and the precipitate is normally filtered, washed and dried [43]. It is important that any traces of sulfates are removed by washing since they may be converted to H_2S during reduction, which is a source of catalyst poisoning [1]. Drying should be carried out at low temperature (< 200 °C) to prevent any oxidation of Fe_3O_4 to Fe_2O_3 [43]. Care must be taken during calcination to avoid formation of large quantities of CrO_3 from the air-oxidation of Cr_2O_3 by the following reaction:

$$2Cr_2O_3 \ + \ 3O_2 \ '' \ 4CrO_3 \tag{2.16}$$

It should be noted that traces of CrO_3 cause some risk to operators [1]. Therefore, before the start-up, Fe_2O_3 must be converted to Fe_3O_4 and any CrO_3 present to Cr_2O_3 by reduction process (equations 2.17-2.20). Industrially, reduction is carried out by process gas (CO/H_2) at about 400 °C with suitable H_2O/H_2 and CO_2/CO ratios [44–46]. These conditions and additional H_2O in process gas are reported to prevent formation of metallic Fe, that promotes the methanation of carbon oxides which could give to a rise of reactor temperature and reduce H_2 yield [1].

$$3Fe_2O_3 \ + \ H_2 \ '' \ 2Fe_3O_4 \ + \ H_2O \qquad \Delta H^0_{298} = - 16.3 \ kJ \ mol^{-1} \tag{2.17}$$

$$3Fe_2O_3 \ + \ CO \ '' \ 2Fe_3O_4 \ + \ CO_2 \qquad \Delta H^0_{298} = + 24.8 \ kJ \ mol^{-1} \tag{2.18}$$

$$2CrO_3 \ + \ 3H_2 \ '' \ Cr_2O_3 \ + \ 3H_2O \qquad \Delta H^0_{298} = - 684.7 \ kJ \ mol^{-1} \tag{2.19}$$

$$2CrO_3 \ + \ 3CO \ '' \ Cr_2O_3 \ + \ 3CO_2 \qquad \Delta H^0_{298} = - 808.2 \ kJ \ mol^{-1} \tag{2.20}$$

In the H_2-TPR analysis (Fig. 2.6), the Fe_2O_3/Cr_2O_3 catalyst exhibits 4 peaks corresponding to the reductions of Fe and Cr oxides in a range from 250 to 800 °C [48]. It is reported that the reducibility of the catalyst depends on dopants: Cu promotes the Fe_3O_4 to FeO transformation to a lower temperature, while addition of Cr to hematite increases the transformation temperature of Fe_2O_3 to Fe_3O_4 [47,48].
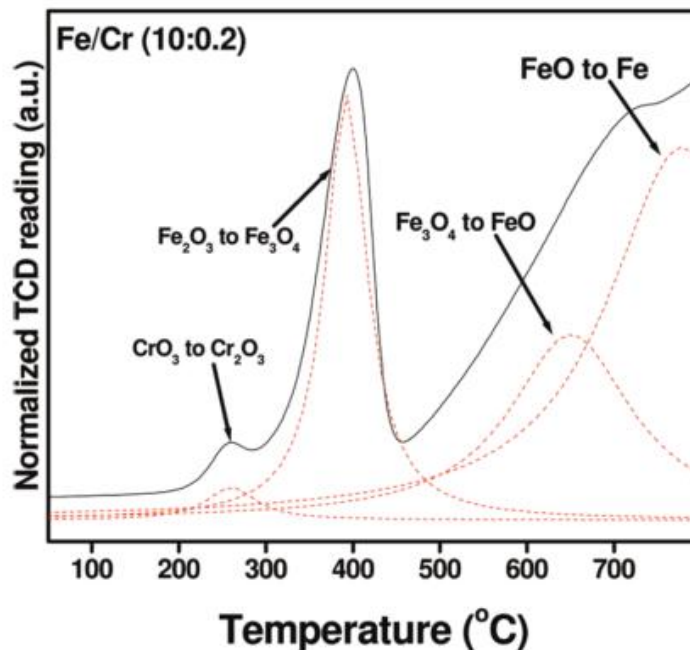
Figure 2.6 H_2-TPR profiles for a Fe_2O_3/Cr_2O_3 catalyst [48].

Reduced HTS catalyst is easily oxidized by the air and, consequently, releases a large amount of heat, leading to raise the catalyst bed temperature. Therefore, reduced HTS catalyst must not be exposed to air, except under carefully controlled conditions. Spent catalyst must be removed under N_2 flow and, then, deposited in a safe place where it may slowly oxidize. Alternatively, the converter may be filled with H_2O and the wet catalyst is removed [1].

In recent years, a small amount of Cu was added to commercial HTS catalysts (Cr/Fe-based catalysts) to improve their activity and selectivity. These catalysts have been industrially used in more severe condition (i.e. lower S/C ratios without being reduced to Fe^0), offering greater operating flexibility than the classical HTS formulations [42,49]. Practically, Cu has the role to increase the activity and Cr is a catalyst stabilizer, while Fe still remains the active phase. However, Cu favors the sintering, leading to low surface areas. The increase in the catalytic activity and surface area of the catalysts reflects the synergetic effects required to the dopants [50].

It has been found that commercial Fe-based catalysts with as high as 8-14 wt.% Cr promoter generally contain about 2 wt.% Cr^{6+} compounds, which are highly toxic to humans and environment, during their manufacture and deposition [50,51]. Thus, it has drawn considerable attention to study Cr-free HTS catalysts by investigating various kinds of oxides, e.g. PbO, La_2O_3, CaO, ZrO_2 Al_2O_3, etc., to replace Cr_2O_3 [50,52–54]. Recently, many studies [42,55–58] have shown that ceria is promising for the WGS reaction by increasing the reducibility of metals and inhibiting metal sintering.

Supporting the Cr-free HTS catalysts, Lee et al. [60] studied Ni and Co to replace Cr in Fe-based catalysts and investigated the activities at LPG reformate conditions. Two catalysts with 20 wt.% of Ni (Zn5FeNi20 and Co5FeNi20) showed a good activity, higher than that of a commercial catalyst (Fe/Cr/Cu by Johnson Matthey) (Fig. 2.7). Fe/Ni catalysts also exhibit higher CO removal activities than Cr-containing catalysts in condition of no addition of H_2O to LPG reformate [61].
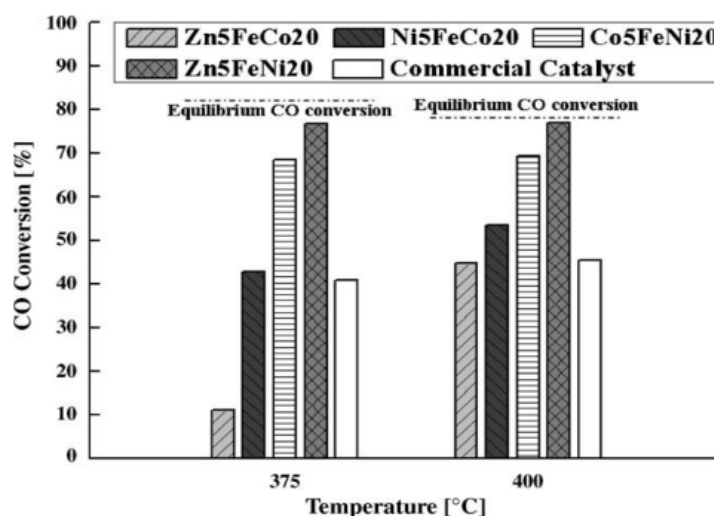

Figure 2.7 CO conversions of three component catalysts at 375 and 400 °C [60].

Fe-Al-Cu catalysts have been recently studied in order to overcome the limits of the LTS/HTS catalysts and operate at MTS. The catalysts possess a good activity at a wide range of temperature [61–65] and the highest CO conversion efficiency is 97.8 % at 300 °C (Fig. 2.8) [62]. It should be noted that Cu plays as an active site at lower temperature,

while magnetite has catalytic effect at higher temperature, and, at this temperature Cu is an electronic promoter in the solid solution [62]. Moreover, the influence of Cu loading on catalyst physical and chemical properties has been investigated [63–65]. According to Zhang and coworkers, Cu promotes formation of maghemite (γ-Fe_2O_3) [65] and the highest CO conversion rate is achieved when Cu/Fe ratio is equal to 1 [62]. It is obvious that the method of preparation plays an important role in catalytic performance; sol-gel is reported as an appropriate technique for Fe-Al-Cu catalysts, which is superior to precipitation/ impregnation routes [63–65]. Moreover, sol-gel method with gelation agents such as propylene oxide or citric acid provides a catalyst with high homogeneity, purity, surface area [66], and better sulfur tolerance than a commercial catalyst [67].
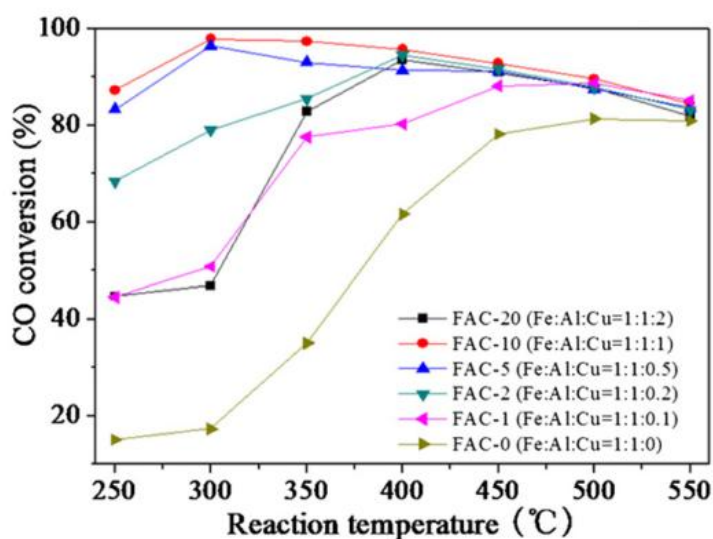

Figure 2.8 CO conversions at various temperatures of the Fe-Al-Cu catalysts, with Fe/Al =1:1 and different Fe/Cu molar ratios [62].

2.4.1.2 LTS formulations

The commercial LTS catalysts ($CuO/ZnO/Al_2O_3$) have gained a wide industrial acceptance. These catalysts possess a good activity at 200-250 °C and are attractive since CO equilibrium is more favored at low temperature. Notwithstanding the high activity, with CO exit concentrations between 0.1 and 0.3 vol.% achieved under LTS conditions, and the other claimed advantages, as the higher selectivity and fewer side reactions at

high pressure, they are highly sensitive to poisoning and thermal sintering. In addition to higher activity [1], the catalyst performance strongly depends on the reaction conditions, such as S/C ratio, contact time, temperature, feed gas composition and pressure [32,67–69]. The maximum CO conversion rate is reached at 250 °C for any condition [68], a large amount of H_2O being necessary to favor the direct WGS reaction [32,67]. Furthermore, the CO conversion changes with the contact time at different S/DG ratios [69]: at lower values of contact time, the LTS catalyst shows higher CO conversion at higher S/DG ratios; differently, the CO conversion decreases with the S/DG ratio at higher values of contact time. Moreover, Utaka et al. [71] observed that a small amount of O_2 (1.3 vol.%) added to reformed fuels accelerates the shift reaction over the Cu-Al_2O_3-ZnO catalyst.

Commercial LTS catalysts ($CuO/ZnO/Al_2O_3$) are produced by co-precipitation method from aqueous solutions of metallic nitrates with sodium carbonate solutions at 30-60 °C and constant pH of 7-9. The precipitates are filtered, washed with deionized water, dried in air at 100 °C and, then, calcined from 300 to 500 °C [71,72]. During the preparation, Al not only stabilizes the metallic Cu crystallites, but may contribute to form hydrotalcite-type precursors which lead to more active catalysts [72]. Hence, the activity of LTS catalyst may depend on the Cu dispersion, Cu particles size and interaction with the support, which are probably related to method of preparation [73,74]. According to Figueiredo and coworkers [68,75], changes in the sequence of co-precipitation of metal nitrates during the preparation of the precursor of $Cu/ZnO/Al_2O_3$ catalysts affect the final properties of Cu^0 at the surface of the catalysts. CZ-A (co-precipitation of two first metals at first and then mixing with the third precipitated metal) performs the best catalytic activity due to the highest surface area. In another study on $Cu/ZnO/Al_2O_3$ catalysts, Tanaka and coworkers [77] showed how the activity of the catalysts prepared by impregnation of γ-Al_2O_3 by nitrate solutions of Cu and Zn (IMP) was lower than those of the samples prepared by co-precipitation of these three solutions (COP) (Fig. 2.9). Therefore, it is clear that the catalyst performance strongly depends on the catalyst composition. Sekizawa and coworkers [68] tried various compositions of Cu/Al_2O_3–MO_x where M = Al, Ce, Co, Cr, Fe, Mg, Mn, Sn, Zn, and Zr; M/Al = 1 (Fig. 2.10). They showed

that Cu/Al_2O_3 with Zn performs an excellent activity and reaches the equilibrium values of CO-CO_2-H_2O at 250 °C. Moreover, they also showed that the activity increases by increasing of Cu amount with maximum at 30 wt.% of Cu. However, overloading Cu amount causes low dispersion, forming large agglomerate particles.
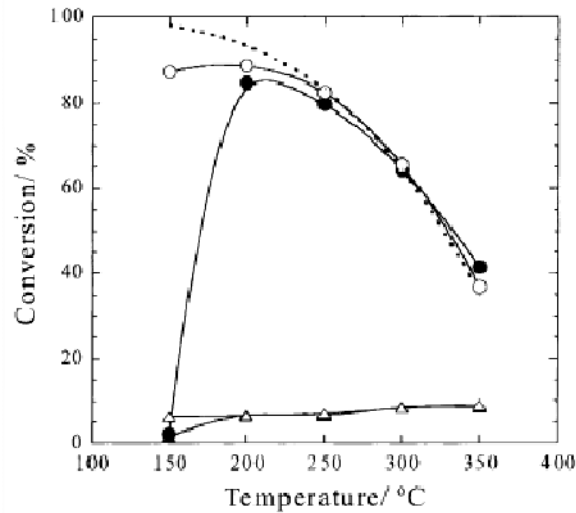

Figure 2.9 $Cu/ZnO/Al_2O_3$ catalysts activity: (™,˜) CO conv. and (r ,p) H_2 conv. over COP-30-30 (open symbol) and IMP-5-5 (closed symbol), (- - -) equilibrium conv. (H_2 37.50%; CO, 1.25%; H_2O, 25.00%; CO_2, 12.50%; O_2, 1.25%; space velocity, 6,400h^{-1})[77].
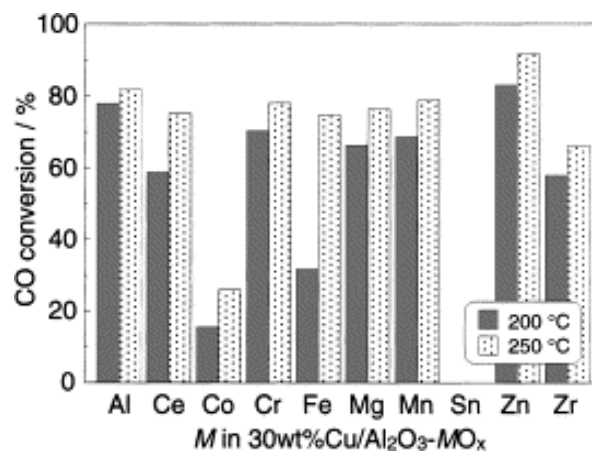

Figure 2.10 CO-shift reaction over 30 wt.% Cu/Al_2O_3–MO_x (CO 12.5 vol.%; H_2O 12.5 vol.%; N_2 balance; GHSV = 7,200 h^{-1}; T = 200 and 250 °C)[68].

It was not demonstrated if the active sites in Cu-based catalysts are either metallic Cu or Cu^+, or both. However, the commercial catalysts (Cu^{2+}) are reduced with a low concentration of H_2 in inert gas, being reaction (21) highly exothermic, that may raise the temperature of catalyst bed, leading to the sintering and, consequently, loss of activity [1]. Gines et al. [72] found that, before the start-up, the catalyst is completely reduced by using a H_2/N_2 flow and maximum temperature of 220 °C without any sintering. The catalyst reduction is completed when the inlet and exit H_2 concentrations are the same, or with a difference lower 0.5 vol.% for 4 h, and the catalyst bed is at temperature of 225-230 °C [1]. When process gas is first introduced, the temperature usually increases rapidly as the catalyst comes to equilibrium with the process conditions.

$$CuO \ + \ H_2 \ " \ Cu \ + \ H_2O \qquad\qquad \Delta H^0_{298} = -80.8 \, kJ \, mol^{-1} \qquad (2.21)$$

Moreover, Fierro et al. [78] showed the correlation between the reduction behavior and calcination temperature: a double peak is replaced by a single and symmetrical peak when the catalyst is calcined at higher temperature, consequence of the sintering of the CuO species in a less reducible Cu-containing fraction. In another study, Fleisch and Mieville [79] reported that the CuO reducibility is higher in the ternary than binary systems. The TPR profile of the $Cu/ZnO/Al_2O_3$ catalyst indicates a superposition of two or three peaks, that may represent the reduction of different Cu^{2+} species (Fig. 2.11) [69]: (a) Cu in the ZnO lattice, (b) amorphous Cu oxide phase, (c) crystalline CuO, and (d) Cu^{2+} in the Al_2O_3 phase. The peaks at 160-170 °C, may be assigned to reduction of Cu^{2+} to Cu^{1+} and Cu^{2+} and/or Cu^{1+} to Cu^0 species, whereas the shoulder at higher temperature may be assigned to Cu species interacting with the Al-containing phase, which is more difficult to reduce.

It should be noted that the reduced catalyst may undergo oxidation in presence of air, leading to release a huge amount of heat, and a temperature raising between 800 and 900 °C. Therefore, the usual procedure to discharge the LTS catalyst is to depressurize the reactor, purge the N_2, cool down to less than 50 °C and discharge the catalyst under a N_2 flow [1].
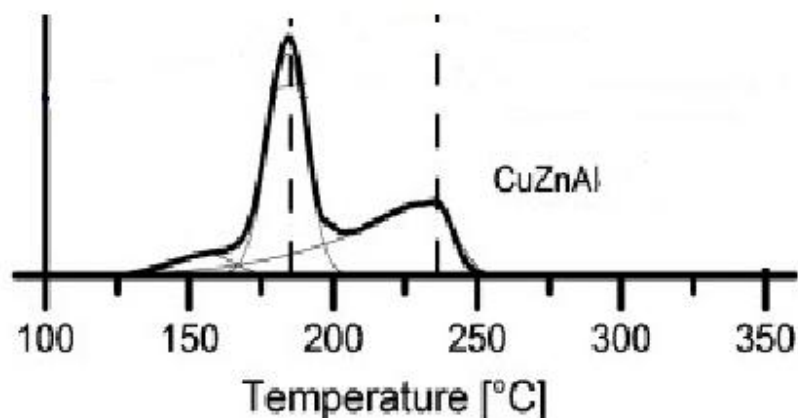
Figure 2.11 Temperature-programmed reduction (TPR) profile of a calcined $Cu/ZnO/Al_2O_3$ catalysts (measured as H_2 consumption in a TCD) [80].

The Cu-based formulations have good activity, but are susceptible of poisoning and operate in a limited temperature range because of problems with Cu sintering. Hence, many studied have been focused on modifications of commercial LTS catalysts to overcome these limits, by introducing additional promoters or changing the method of preparation. Saito and Murata [81] indicate that the activity of $Cu/ZnO/ZrO_2/Al_2O_3$ catalyst for the WGS reaction at 250 °C is less affected by the pre-treatments such as calcinations and treatment in H_2 at higher temperature than that of the $Cu/ZnO/Al_2O_3$ catalyst (Fig. 2.12). Other authors [71] found that addition of a small amount (0.8 wt.%) of colloidal silica to a Cu/ZnO-based catalyst significantly enhances its stability for the WGS reaction compared to the catalyst without SiO_2 (Fig. 2.13). Differently, Shishido et al. [82] showed that the highest activity is obtained over homogeneously precipitated $Cu/MgO/ZnO$ due to the enhanced formation of Cu^+ species as active sites, with even an addition of 0.1 wt.% of Mg, which leads to greatly increase in CO conversion and Cu metal surface. Additionally, a trace amount of MgO-doping on Cu/Zn/Al has been the most effective among the alkaline-earth metals and exhibits higher activity and sustainability than commercial $Cu/ZnO/Al_2O_3$ catalyst [83].
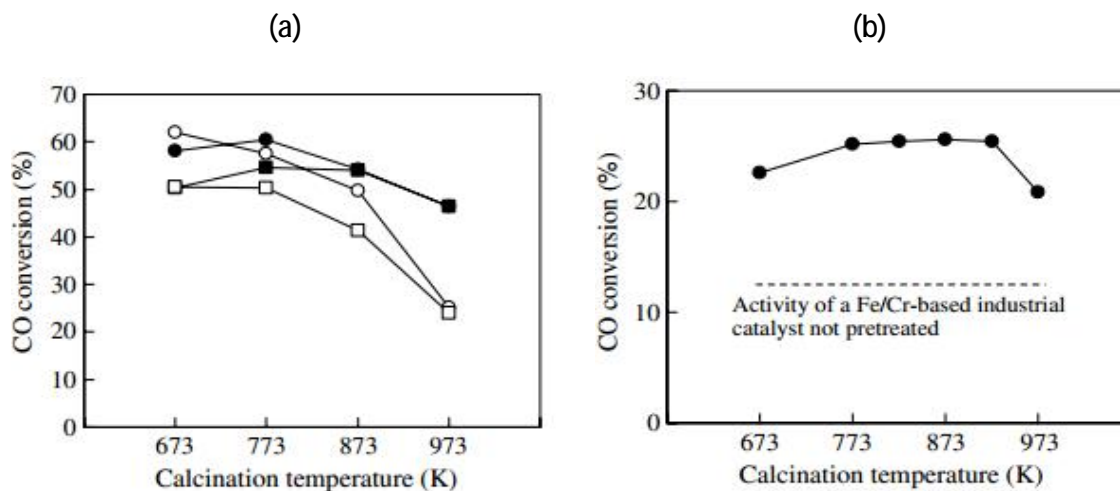
(a)   (b)

Figure 2.12 (a) WGS activity of a Cu/ZnO/Al$_2$O$_3$ (O,□) and a Cu/ZnO/ZrO$_2$/Al$_2$O$_3$ (<,=) catalysts treated in H$_2$ at 300 °C (O,=) or at 500 °C (□,<) as a function of calcination temperature; (b) Cu surface areas of the post-reaction catalysts used for the WGS reaction as a function of calcination temperature. The symbols are the same as shown in figure (a). Reaction conditions: 250 °C, 1.5 atm, feed gas (CO 10%; CO$_2$ 18% ; H$_2$ 72%), H$_2$O/CO = 2.7, SV (except water) = 36,000 h^{-1} [81].
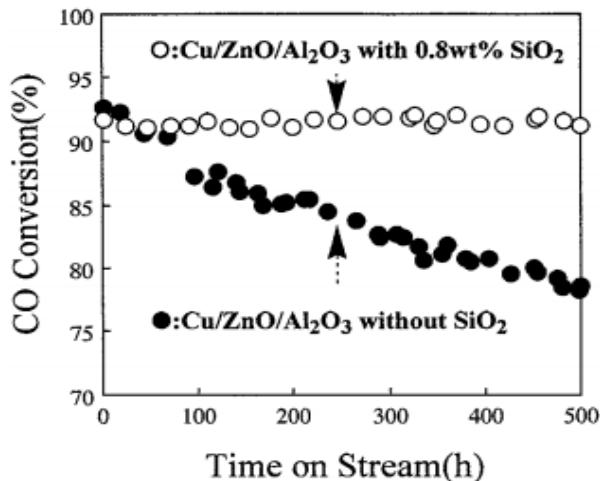

Figure 2.13 Effect of addition of colloidal silica into a Cu/ZnO/Al$_2$O$_3$ catalyst on the long-term stability in the CO shift reaction. Reaction conditions: 11 atm, 205 °C, GHSV(dry) 11,250 h^{-1}, steam/gas= 1.5, and CO/CO$_2$/H$_2$ = 3/22/75. (o) Cu/ZnO/Al$_2$O$_3$ catalyst with 0.8 wt.% silica; (●) Cu/ZnO/Al$_2$O$_3$ catalyst without silica [71].

It has been found that Cu/CeO_2 catalysts exhibit high catalytic activities for the WGS reaction at both high and low temperature [55,82], but not at middle temperature. Many authors tried to enhance the catalyst performance by changing the composition, adding other metals or changing the method of preparation. In 2011, Li et al. [85] investigated the effect of CeO_2 supports prepared using different precipitants ($NH_3.H_2O$; $(NH_4)_2CO_3$; K_2CO_3) on the catalytic performance. They found that Cu/CeO_2 prepared using $NH_3.H_2O$ presents the highest Cu dispersion, best thermal stability, and, therefore, highest CO conversion. Furthermore, they [84] reported that Cu/CeO_2 prepared by urea co-precipitation-gelation method [86] shows greater surface area than conventionally co-precipitated sample, due to a long boiling step and the slow decomposition of urea [70,85]. Djinović et al. [88] reported that the activity of Cu/CeO_2 catalysts in the WGS reaction is related to the extent of surface CeO_2 reduction and the synergetic interactions between CuO and CeO_2; the catalyst activity can be positively modified by adding La as structure stabilizer [84] or Zr to avoid formation of Ce(III) hydroxycarbonate [87,88]. Moreover, Gunawardana et al. [91] found that 80% of Cu loading exhibits the best activity for the WGS reaction in the range 150-360 °C (Fig. 2.14).
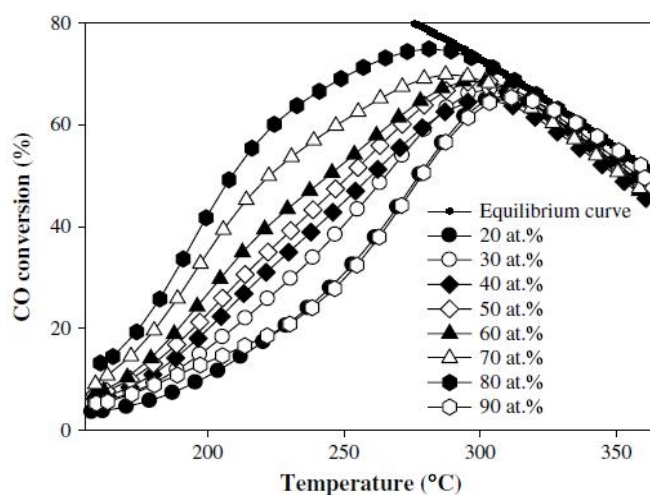

Figure 2.14 The effect of Cu loading on the WGS reaction over copper–ceria catalyst during the third run in 150–360 °C range. Feed gas composition, CO-5%, CO_2-10%, H_2O-15%, H_2-40% and He-30% (vol.%), total flow 50 ml/min [91].

2.4.2 Recent Developments

In recent years, a new generation of catalyst for the WGS reaction has been developed to operate at intermediate temperature, overcoming the thermodynamic limits and improving the thermal stability of commercial catalysts [92]. Moreover, this type of catalysts may operate in one converter instead of the two HTS and LTS reactors, and therefore, reduce the operation cost. Also, these catalysts provide some benefits:

- a lower S/C ratio in the reformer is possible, without sintering and Fisher-Tropsch reactions from Fe-based (HTS) catalysts;

- no by-pass control on the PG boiler is needed; this controller is prone to metal dusting problems.

Other considerations are similar to LTS process, except that another reactor is needed and an additional exchanger is required to reach MTS process temperatures [92].

Noble metal-containing catalysts have been reported as active and non-pyrophoric, with activity higher than those of conventional WGS catalysts in the MTS range, thus potential candidates for the WGS process [93]. The use of supported noble metal catalysts may offer significant advantages, including operation at higher temperatures, where kinetics are more favorable, no need of activation prior to the use, no degradation by exposure to air or temperature cycles and availability of conventional wash-coating technologies [94]. These catalysts are prepared by the impregnation method and the effect of the nature of the metallic phase (Pt, Rh, Ru, and Pd) has been investigated when supported on CeO_2 [86,92–102], Al_2O_3 [92,94], ZrO_2 [102–105] and TiO_2 [92,106–111], and the activity follows the order (Fig. 2.15):

$$Pt > Rh \approx Ru > Pd$$

However, some differences in results may be attributed to the different nature of the support used [92,112,113]. The reducibility of the support plays a crucial role on the catalytic performances of dispersed noble metal catalysts [94]. On the other hand, it is very important to note that Pt–containing catalysts exhibit significantly higher activities when supported on "reducible" (TiO_2, CeO_2, La_2O_3, and YSZ) rather than on "non-reducible" oxides (Al_2O_3, MgO, and SiO_2) [94]. Pt/CeO_2 catalysts are 15 times more active

than Pt/Al_2O_3 catalysts [97]. The catalytic performance of supported Pt catalysts for the single-stage WGS decreases with the order [116]:

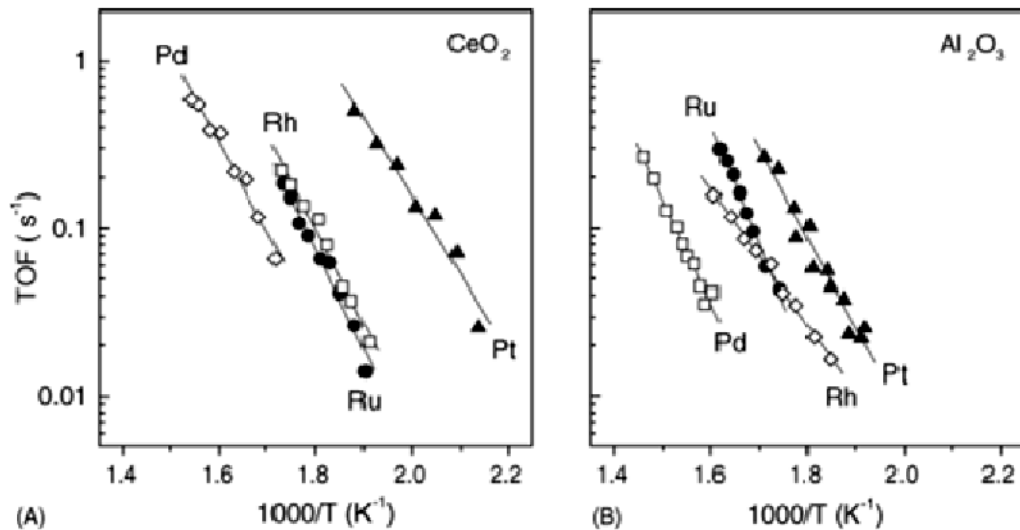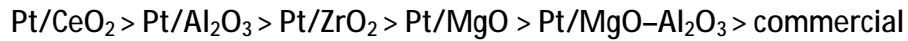$$Pt/CeO_2 > Pt/Al_2O_3 > Pt/ZrO_2 > Pt/MgO > Pt/MgO–Al_2O_3 > commercial$$

Figure 2.15 Arrhenius plots of rates (TOF values) of CO conversion obtained for Pt-, Rh-, Ru-, and Pd-containing catalysts (0.5 wt.%) supported on (A) CeO_2 and (B) Al_2O_3 [94].

In fact, introduction of noble metals onto the ceria creates surface defects, which promote the decomposition of the surface intermediates [14]. Therefore, Ce-supported precious metals have great potential to be used as WGS catalysts [95,115,116]. Some experiments on Pt/CeO_2 catalysts by Johnson Matthey (UK) [43] showed that the catalysts perform high activity in a range of temperature of 325-400 °C (Fig. 2.16). On the other hand, the catalysts lose activity under synthetic and real reformate tests due to a further gradual decrease in the total BET surface area and to the occlusion by Pt particles of the support. Johnson Matthey also developed a new formulation catalyst (JM8) which consists of non-pyrophoric Pt-containing species, with improved durability and no methanation activity between 200 and 500 °C [91,117]. Some authors [96,118–121] reported Pt ions substituted into CeO_2 framework to form solid solution catalysts, showing high activity for the WGS reaction. It is indicated that Pt and Au ions in 10-20 % La^{3+} doped CeO_2 catalyst exhibits high CO conversion rate for the WGS reaction at the

intermediate temperature [118,119]. This type of catalyst is deactivated during a long time test because of formation of surface carbonate as a result of the interaction of La^{3+} with CO_2. Fortunately, addition of Ti in Pt/CeO_2 leads to a solid solution, which is a highly active, and to a non-deactivating catalyst for the WGS reaction, due to the presence of strongly acid Ti^{4+} ion leading to no carbonate formation [56]. In addition to Pt/CeO_2 catalysts, nano-sized Pt particles stabilize CeO_2 support against sintering and loss of surface area [122,123]. Roh et al. [124,125] developed a new method to synthesize nano-sized CeO_2 support based on a simultaneous precipitation and digestion of cerium carbonate. The catalyst prepared by this new method shows a Pt dispersion (79.3 %) much higher than that previously reported (54.0 %) [126]. Many researchers [92–95] showed that Pt-based catalysts show higher CO conversion than other metals supported on CeO_2. Therefore, nano-sized Pt/CeO_2 catalysts may be considered to be promising candidates for WGS catalyst.
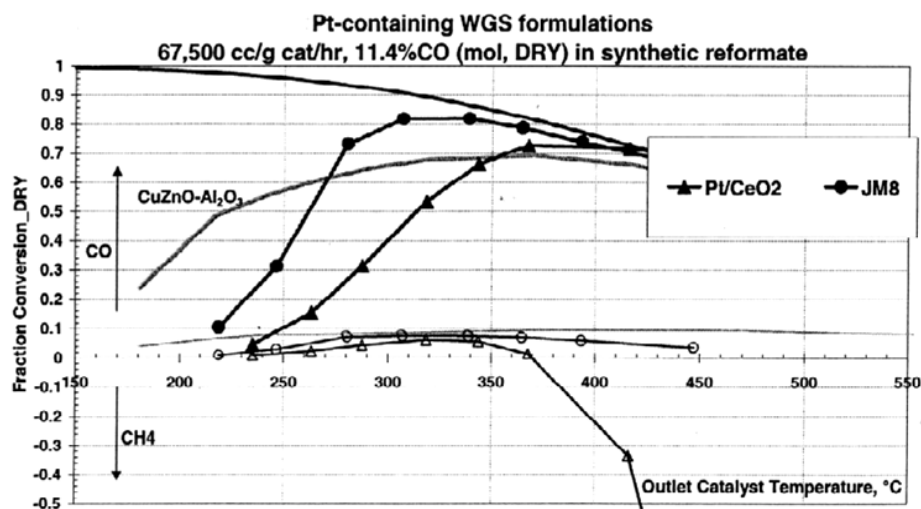

Figure 2.16 Performance of a new Johnson Matthey Pt-containing WGS catalyst (JM8) compared to a Pt/CeO_2 catalyst at the same metal content [43].

Moreover, Jeong and coworkers [107] found that the addition a small amount of Na (about 2 wt.%) enhances the activity of nano-sized Pt/CeO_2 catalyst for the WGS reaction at low temperature. Table 2.3 shows that the addition of Na reduces the Pt crystallite size from 3.0 nm to 2.2 nm, resulting in a better dispersion of 51.7 % in Na-

added catalyst compared to that of 37.6 % in a catalyst without Na. In addition, small amount of silica (5–10 wt.%) greatly improves the catalytic performance of Pt/CeO_2 [128].

Table 2.3 Characteristics of $Pt-Na/CeO_2$ and Pt/CeO_2 catalysts [107].

Catalyst	S.A.[a] (m^2/g)	Dispersion[b] (%)	Pt S.A.[b] (m^2/g)	Pt Size[b] (nm)
$1Pt-2Na/CeO_2$	109	51.7	1.28	2.2
$1Pt/CeO_2$	104	37.6	0.92	3.0

[a]Estimated from N_2 adsorption at −196 °C. [b]Estimated from CO-chemisorption at 50 °C

It should be noted that a small amount of Fe added into 1 wt.% Pd/CeO_2 catalyst significantly increases the WGS reaction rate [93]. Mahadevaiah et al. [118] studied Fe-Pt supported on CeO_2 ($Ce_{0.65}Fe_{0.33}Pt_{0.02}O_{2-b}$) and free-Pt catalyst ($Ce_{0.67}Fe_{0.33}O_{2-b}$) obtained by low-temperature sonochemical method (Fig. 2.17). Complete CO conversion is observed at 285 °C for Pt-containing catalyst, while Ce-Fe catalyst achieves the total conversion at higher temperature. No by-products such as CH_3OH, HCHO and CH_4 are detected. The authors finally concluded that Fe substituted ceria ($Ce_{0.67}Fe_{0.33}O_{2-b}$) acts as a good candidate, but the addition of Pt is necessary to have a much higher activity for the WGS reaction at moderate temperature.
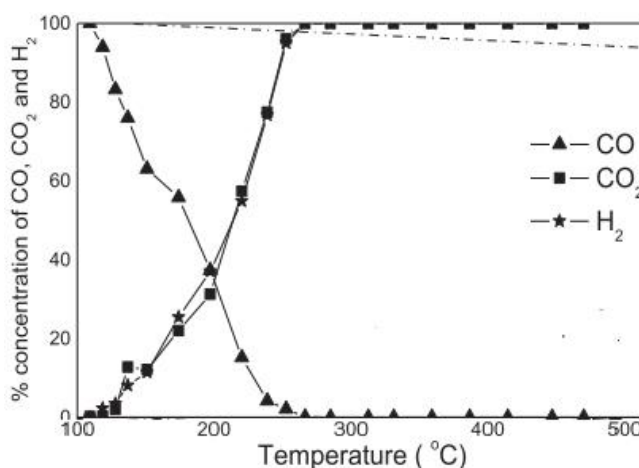

Figure 2.17 % CO, CO_2 and H_2 concentrations in the WGS reaction (gas composition: 2 cm^3/min CO, 30 cm^3/min H_2O balance with N2 keeping total gas flow 130 cm^3/min) over $Ce_{0.65}Fe_{0.33}Pt_{0.02}O_{2-6}$ [118].

Recently, Au-based catalysts received attention due to their high activity at low temperature for the WGS reaction [127–135]. Performance of Au-containing catalysts depends on both Au particle properties and supports [127,136,137]. The high catalytic performance of Au-containing catalysts is generally related to synergetic effects between Au and support which involves the formation of intermediates as a result of interaction between adsorbed reactants and active phase [21,128,129,138]. However, it is still uncertain if the catalytically active species are metal Au or oxidized Au species [141]. The final properties are strongly related to the Au particle size and intimate metal-support interactions in the catalysts, depending on the method of preparation [66,87,131,136,137,140–147]. The preferred technique for the preparation of highly dispersed Au-based catalysts is the deposition-precipitation method [129,131,148,149], that involves the deposition of Au hydroxide onto the support through a chemical reaction in aqueous solution between $HAuCl_4 \cdot 3H_2O$ and Na_2CO_3. This technique allows to produce catalysts with narrower particle size distribution, where Au is mainly localized on the surface of the supports [130,149].

Ceria was previously demonstrated as a suitable support for noble metal containing catalysts. Au deposited on ceria shows a great activity for the WGS reaction, moreover, high stability over a long-term test was recorded for this type of Au-containing catalysts by Andreeva et al. [134]. Furthermore, the performance of Au/CeO_2 catalyst is greatly improved by adding rare earth metals (Nd, Eu, Sm, Y, La) [66,146,150,151], Zr [87,152], Ga [155], Al [147,154], and Fe [155,156]. Fe oxide is also considered as a good support for Au-containing catalysts, which shows high activity at low temperature due to specific interaction between Au and ferric oxide support [149,157]; however, deactivation is observed as a result of sintering of Fe oxide, leading to a significant decrease in the support surface area [88,158]. Andreeva et al. [134] observed the deactivation of Au-based catalysts during stability tests, due to agglomeration of Au particles; in this study, three different catalysts: Pt/CeO_2, Au/CeO_2 and Au/Fe_2O_3 catalysts were tested for 48 h. Pt-containing sample shows a good stability while the activity of two Au-containing catalysts rapidly decreases, with higher average size of the Au particles after reaction (Fig.

2.18) [151]. Whereas CeO_2 is inactive for the WGS reaction, the Au/CeO_2 catalyst is initially very active, with rates that are in some cases superior to those of a commercial Cu/Zn/Al (Süd-Chemie) catalyst [161].
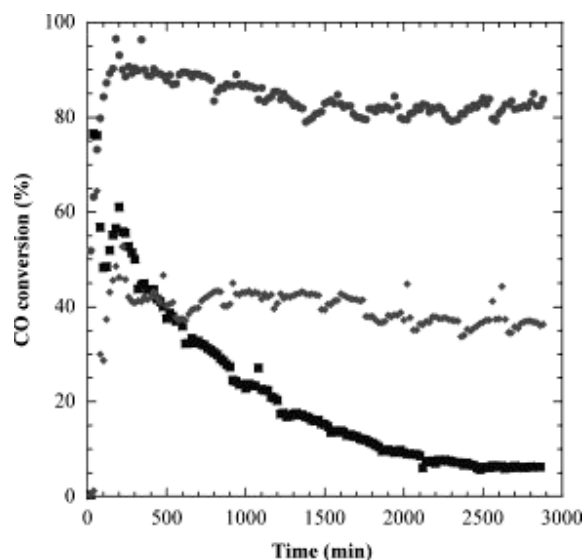

Figure 2.18 Deactivation tests for the Pt/CeO_2 sol–gel, Au/CeO_2 co-precipitation, and Au/Fe_2O_3 deposition–precipitation catalysts; (●) Pt/CeO_2; (ᴜ) Au/CeO2; (n) Au/Fe_2O_3 [151].

Fuentes and coworkers [162] studied Ni-based catalysts obtained from hydrotalcite-type compounds to find a catalyst able to operate effectively at intermediate temperature. It was found that Al-Ni-based catalyst ($N_{0.66}A_{0.33}$) is more active than Cu-based catalyst (Fig. 2.19); however, Ni-based catalyst shows a low selectivity in the WGS reaction, which is enhanced by adding small amount of Zn. Furthermore, the activity is increased with Ni content. The authors concluded that the most promising catalyst for the WGS reaction is the $Ni_{0.44}Zn_{0.22}A_{0.3}$ sample, which shows the highest activity in the range of 250-350 °C and does not produce methane [162].

In the past years, some authors focused on Cu-supported on silica catalysts (Cu/SiO_2) displaying high activity for WGS and H_2O dissociation reactions [161–163]. The catalysts may be prepared by different methods: thermal decomposition of silica-supported precursor [164], impregnation [166] or Atomic Layer Epitaxy (ALE) technique [163], which strongly affect the catalyst performance. ALE is a surface-controlled, layer-

by-layer process that deposits thin films at an atomic scale through self-limiting surface reactions [167], and recently used for preparation of nano-scale metal catalysts. Chen et al. [163] reported that ALE-Cu/SiO$_2$ catalyst has higher activity than impregnated Cu-based catalysts (IM-Cu/SiO$_2$) in the WGS reaction (Fig. 2.20). On the other hand, bimetallic catalyst supported on SiO$_2$ (Cu-Ni/SiO$_2$ or Zn-Ni/SiO$_2$) prepared by thermal decomposition shows higher surface area than those on other supports and better WGS activity than those prepared by impregnation or coprecipitation methods [151,162].
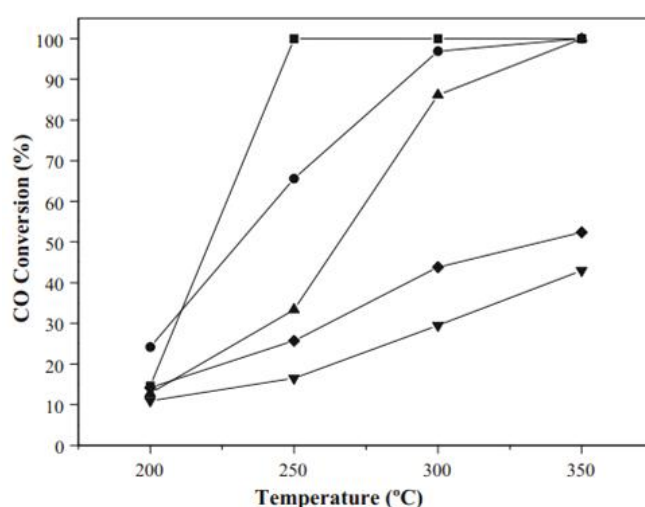

Figure 2.19 Conversion of CO over Ni- Cu-containing catalysts as a function of the reaction temperature: $N_{0.66}A_{0.33}$ ($<$); $N_{0.44}Z_{0.22}A_{0.33}$ ($=$); $N_{0.33}Z_{0.33}A_{0.33}T$ (▲); $C_{0.44}Z_{0.22}A_{0.33}$ (,); $C_{0.33}Z_{0.33}A_{0.33}$ (ᴗ) [162].
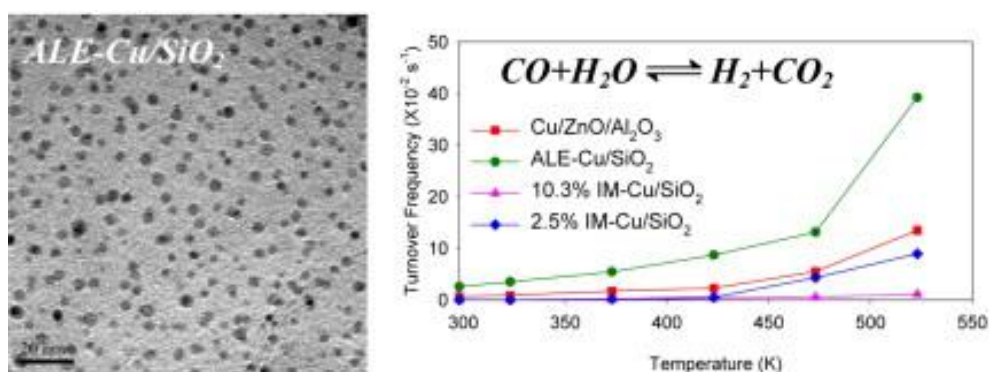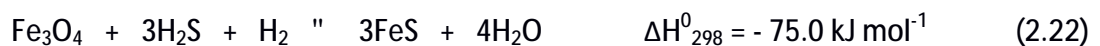

Figure 2.20 TEM images of ALE-Cu/SiO$_2$ and TOF values versus temperature for ALE-Cu/SiO$_2$; 20% Cu/ZnO/Al$_2$O$_3$; 10.3% IM-Cu/SiO$_2$; 2.5% IM-Cu/SiO$_2$ [163].

2.5 Deactivation and Poisoning

It has been demonstrated that deactivation is a multi-step process, with a rapid decrease in activity occurring during the first 150 h of use, followed by a slow decay over extended periods of several years [166,167]. The initial decay has been attributed to particle growth, by two simultaneous but different mechanisms, or to a rapid agglomeration of very small particles.

The main reason of Fe/Cr deactivation is a thermal sintering which leads to low surface area, reduction of porosity, increase of particle size and, of course, lower catalyst activity [169]. Susceptibility to thermal sintering is an intrinsic property of all dispersed heterogeneous catalysts. In general, Cu-based catalysts are more susceptible than other metallic catalysts. Early works always report a rapid deactivation, which is due to both poisoning and a rapid loss of Cu-surface area brought by sintering [1].

HTS catalysts do not normally suffer any problems from poisoning or coke formation. However, a large amount of H_2S and COS present in feed gas, especially in coal-based plants, may convert the iron oxides to iron sulphide blocking the active sites by the reactions [1]:

$$Fe_3O_4 \; + \; 3H_2S \; + \; H_2 \; " \; 3FeS \; + \; 4H_2O \qquad \Delta H^0_{298} = - 75.0 \, kJ \, mol^{-1} \qquad (2.22)$$

$$COS \; + \; H_2O \; " \; CO_2 \; + \; H_2S \qquad \Delta H^0_{298} = - 34.6 \, kJ \, mol^{-1} \qquad (2.23)$$

Moreover, if feed gas contains traces of unsaturated hydrocarbons and nitric oxide, the catalysts can be contaminated by gum containing a high C-content, which blocks the catalyst pores, and therefore, prevents access of gas to the catalytic sites [1]. These effects can be eliminated by installing a separate guard bed of HTS catalyst which may be regenerated, that may be done by treating the catalyst at 450 °C with steam containing 1-2 vol.% of O_2 [1].

Low poisoning resistance is considered as one of most relevant disadvantages of Cu-based catalysts. Both S- and Cl-containing compounds are main sources of deactivation of Cu-based catalysts, which can be originated from the feedstock or steam process. Care must be taken to avoid even very low levels of S in feed gas because sulphiding reaction is

very favored under LTS conditions (reaction 2.24). Moreover, ZnO can trap the sulphur at the top of the catalyst bed as zinc sulphide (reaction 2.25), which is more stable than copper sulphide [1].

$$2Cu \ + \ H_2S \ " \ \ Cu_2S \ + \ H_2 \qquad\qquad \Delta H^0_{298}= -59.4 \ kJ/mol \qquad (2.24)$$

$$ZnO \ + \ H_2S \ " \ \ ZnS \ + \ H_2O \qquad\qquad \Delta H^0_{298} = -76.6 \ kJ/mol \qquad (2.25)$$

Chlorides act as powerful poison decreasing the activity of LTS catalysts irreversibly. This is because both Zn and Cu react with HCl to form chloride salts which have high surface mobility resulting in a destructive destabilization of catalytic activity via structural changes. In addition, formation of chlorides results in low melting point of the catalyst (for instance melting point of CuCl is 430 °C). Consequently the catalyst lacks sufficient thermal stability by sintering during operation [1].

Besides, silica is considered to be a serious problem for LTS catalysts since it deposits on the surface and finally into the pores of the pellets, where it reacts to form zinc silicate. This formation reduces the quantity of available free ZnO at the top of the bed, which is used to absorb poisons such as sulphur and chloride. Consequently, the catalyst is less resistant to transfer these poisons into the catalyst bed, which deactivates more rapidly [1].

Other poisons for Cu-based catalysts include arsenic, which might come from some types of CO_2 removal systems, and trivalent phosphorous, which could originate from boiler H_2O feed, but in practice, these are rarely encountered in the process gas [1].

References

[1]   M.V. Twigg, *Catalyst Handbook*, Wolfe, London (UK), 1996.

[2]   G.C. Chinchen, P.J. Denny, J.R. Jennings, M.S. Spencer, *Appl. Catal.* 36 (1998) 1.

[3]   J.M. Moe, *Chem. Eng. Prog.* 58 (1962) 33.

[4]   C. Callaghan, I. Fishtik, R. Datta, M. Carpenter, M. Chmielewski, A. Lugo, *Surf. Sci.* 541 (2003) 21.

[5]   C.V. Ovesen, P. Stolze, J.K. Norskovand, C.T.A. Campbell, *J. Catal.* 134 (1992) 445.

[6]   C. Ratnasamy, J.P. Wagner, *Catal. Rev.* 51 (2009) 325.

[7]   C.V. Ovesen, B.S. Clausen, B.S. Hammershøi, G. Steffensen, I. Askgaard, T. Chorkendorff, J.K. Nørskov, P.B. Rasmussen, P. Stoltze, P. Taylor, *J. Catal.* 158 (1996) 170.

[8]   T. van Herwijnen, W.A. de Jong, *J. Catal.* 63 (1980) 83.

[9]   J.M. Campbell, J. Nakamura, C.T. Campbell, *J. Catal.* 136 (1992) 24.

[10]   T. Am Shido, A. Yamaguchi, K. Asakura, Y. Iawasawa, *J. Mol. Catal. A: Chemical* 16 (2000) 67.

[11]   T. Shido, Y. Iwasawa, *J. Catal.* 129 (1991) 343.

[12]   A.A. Gokhale, J.A. Dumesic, M.M. Mavrikakis, *J. Am. Chem. Soc.* 130 (2008) 1402.

[13]   T. Shido, Y. Iwasawa, *J. Catal.* 136 (1992) 493.

[14]   T. Shido, Y. Iwasawa, *J. Catal.* 141 (1993) 71.

[15]   A.B. Mhadeshwar, D.G. Vlachos, *Catal. Today* 105 (2005) 162.

[16]   A.B. Mhadeshwar, D.G. Vlachos, *J. Catal.* 231 (2005) 48.

[17]   N.A. Koryabkina, A.A. Phatak, W.F. Ruettinger, R.J. Farrauto, F.H. Rebeiro, *J. Catal.* 217 (2003) 233.

[18]   R.J. Madon, D. Braden, S. Kandoi, P. Nagel, M. Mavrikakis, J. a. Dumesic, *J. Catal.* 281 (2011) 1.

[19]   Q. Tang, Z. Chen, X. He, *Surf. Sci.* 603 (2009) 2138.

[20]   H. Nishimura, T. Yatsu, T. Fujitami, T. Uchijima, J. Nakamura, *J. Mol. Catal. A: Chemical* 155 (2000) 3.

[21]   L.I. Ilieva, D.H. Andreeva, A.A. Andreev, *Thermochim. Acta* 292 (1997) 169.

[22]   D. Tibiletti, A. Goguet, D. Reid, F.C. Meunier, R. Burch, *Catal. Today* 113 (2006) 94.

[23]   R. Burch, *Phys. Chem. Chem. Phys.* 8 (2006) 5483.

[24]   T. Shishido, M. Yamamoto, D. Li, Y. Tian, H. Morioka, M. Honda, T. Sano, K. Takehira, *Appl. Catal.* A 303 (2006) 62.

[25]   N.E. Amadeo, M.A. Laborde, *Int. J. Hydr. En.* 20 (1995) 949.

[26]   C. Rhodes, G.J. Hutchings, A.M. Ward, *Catal. Today* 23 (1995) 43.

[27]   J.L. Ayastuy, M.A. Gutiérrez-Ortiz, J.A. González-Marcos, A. Aranzabal, J.R. González-Velasco, *Ind. Eng. Chem. Res.* 44 (2005) 41.

[28]   R.J. Byron Smith, L. Muruganandam, S. Murthy Shekhar, *Comp. Chem. Eng.* 35 (2011) 2646.

[29]   D.S. Newsome, *Catal. Rev.* 21 (1980) 275.

[30]   E. Fiolitakis, H. Hofmann, *J. Catal.* 80 (1983) 328.

[31]   T. Salmi, R. Hakkarainen, *Appl. Catal.* 49 (1989) 285.

[32]   Y. Choi, H.G. Stenger, *J. Power Sources* 124 (2003) 432.

[33]   P. de Molliens, *In Technique De l'Ingénieur, Traité Génie Des Procédés,* J 4 080 (1993) 1.

[34]   A.S. Augustine, Y.H. Ma, N.K. Kazantzis, *Int. J. Hydr. En.* 36 (2011) 5350.

[35]   M.D. Falco, L. Marrelli, G. Iaquaniello, *Membrane Reactors for Hydrogen Production Processes,* Springer, London (UK), 2011.

[36]   M.D. Dolan, N.C. Dave, A.Y. Ilyushechkin, L.D. Morpeth, K.G. McLennan, *J. Membr. Sci.* 285 (2006) 30.

[37]   S. Tosti, *Int. J. Hydr. En.* 35 (2010) 12650.

[38]   R. Sanz, J.A. Calles, D. Alique, L. Furones, S. Ordóñez, P. Marín, P. Corengia, E. Fernandez, *Int. J. Hydr. En.* 36 (2011) 15783.

[39]   A. Brunetti, G. Barbieri, E. Drioli, *Chem. Eng. Sci.* 64 (2009) 3448.

[40] A.L. Mejdell, H. Klette, A. Ramachandran, A. Borg, R. Bredesen, *J. Membr. Sci.* 307 (2008) 96.

[41] G.Q. Lu, J.C. Diniz, M. Duke, S. Giessler, R. Socolow, R.H. Williams, T. Kreutz, *J. Coll. Interf. Sci.* 314 (2007) 589.

[42] K. Babita, S. Sridhar, K.V. Raghavan, *Int. J. Hydr. En.* 36 (2011) 6671.

[43] A.M. Ward, S.A. Axon, P.J. Murray, WO Patent 03,022,427 (2003) to Johnson Matthey.

[44] M.A. Edwards, D.M. Whittle, C. Rhodes, A.M. Ward, D. Rohan, M.D. Shannon, G.J. Hutchings, C.J. Kiely, *Phys. Chem. Chem. Phys.* 4 (2002) 3902.

[45] M.S. Batista, E.M. Assaf, J.M. Assaf, E.A. Ticianelli, *Int. J. Hydr. En.* 31 (2006) 1204.

[46] P.N. Hawker, *Hydr. Proc.* 61 (1982) 183.

[47] D.J. Borgas, G.W. Bridger, *Chem. Ind (London)* (1960) 1426.

[48] G.K. Reddy, K. Gunasekara, P. Boolchand, P.G. Smirniotis, *J. Phys. Chem. C* 115 (2011) 920.

[49] G.K. Reddy, P.G. Smirniotis, *Catal. Lett.* 141 (2011) 27.

[50] E.B. Quadro, M. de L.R. Dias, A.M.M. Amorim, M. do C. Rangel, *J. Braz. Chem. Soc.* 10 (1999) 51.

[51] G.C. Chinchen, WO Patent A-0,062,410 (1982) to Imperial Chemical Industries Ltd.

[52] G.C. Chinchen, M.S. Spencer, K.C. Waugh, D.A. Whan, *J. Chem. Soc. Faraday Trans. 1* 83 (1987) 2193.

[53] J. Tsagaroyannis, K.-J. Haralambous, Z. Loizos, G. Petroutsos, N. Spyrellis, *Mat. Lett.* 28 (1996) 393.

[54] G.C. de Araújo, M. do Carmo Rangel, *Catal. Today* 62 (2000) 201.

[55] C. Martos, J. Dufour, A. Ruiz, *Int. J. Hydr. En.* 34 (2009) 4475.

[56] X. Qi, M. Flytzani-Stephanopoulos, *Ind. Eng. Chem. Res.* 43 (2004) 3055.

[57] X. Wang, R.J. Gorte, J.P. Wagner, *J. Catal.* 212 (2002) 225.

[58] Y. Wang, S. Liang, A. Cao, R.L. Thompson, G. Veser, *Appl. Catal.* B 99 (2010) 89.

[59] Y. Zhang, G. Zhang, Y. Zhao, X. Li, Y. Sun, Y. Xu, *Int. J. Hydr. En.* 37 (2012) 6363.

[60] J.Y. Lee, D.-W. Lee, K.-Y. Lee, Y. Wang, *Catal. Today* 146 (2009) 260.

[61] J.Y. Lee, D.-W. Lee, Y.-K. Hong, K.-Y. Lee, *Int. J. Hydr. En.* 36 (2011) 8173.

[62] Z. Bao, W. Ding, Q. Li, *Int. J. Hydr. En.* 37 (2012) 951.

[63] S. Natesakhawat, X. Wang, L. Zhang, U.S. Ozkan, *J. Mol. Catal. A: Chemical* 260 (2006) 82.

[64] L. Zhang, X. Wang, J.-M.M. Millet, P.H. Matter, U.S. Ozkan, *Appl. Catal.* A 351 (2008) 1.

[65] L. Zhang, J.M. Millet, U.S. Ozkan, *Appl. Catal.* A 357 (2009) 66.

[66] P. Gawade, B. Mirkelamoglu, B. Tan, U.S. Ozkan, *J. Mol. Catal. A: Chemical* 321 (2010) 61.

[67] P. Gawade, B. Mirkelamoglu, B. Tan, L. Zhang, U. Ozkan, in *Conf. Proc.,* 09AIChE ,Tennessee (USA), 2009.

[68] K. Sekizawa, S.-Ichi Yano, K. Eguchi, H. Arai, *Appl. Catal.* A 169 (1998) 291.

[69] R.T. Figueiredo, A.L.D. Ramos, H.M.C. de Andrade, J.L.G. Fierro, *Catal. Today* 107–108 (2005) 671.

[70] D. Mendes, H. Garcia, V.B. Silva, L.M. Madeira, *Ind. Eng. Chem. Res.* 48 (2009) 430.

[71] T. Utaka, T. Takeguchi, R. Kikuchi, K. Eguchi, *Appl. Catal.* A 246 (2003) 117.

[72] M.J.L. Ginés, N. Amadeo, M. Laborde, C.R. Apesteguía, *Appl. Catal.* A 131 (1995) 283.

[73] A.A.G. Lima, M. Nele, E.L. Moreno, H.M. Andrade, *Appl. Catal.* A 171 (1998) 31.

[74]   T. Shishido, S. Nishimura, Y. Yoshinaga, K. Ebitani, K. Teramura, *Catal. Comm.* 10 (2009) 1057.

[75]   S. Nishimura, T. Shishido, K. Ebitani, K. Teramura, T. Tanaka, *Appl. Catal.* A 387 (2010) 185.

[76]   Figueiredo, H. Martins, C. Andrade, J.L.G. Fierro, *J. Mol. Catal. A: Chemical* 318 (2010) 15.

[77]   Y. Tanaka, T. Utaka, R. Kikuchi, K. Sasaki, K. Eguchi, *Appl. Catal.* A 238 (2002) 11.

[78]   G. Fierro, M.L. Jacono, M. Invers, P. Porta, F. Cioci, R. Lavecchia, *Appl. Catal.* 137 (1996) 327.

[79]   T.H. Fleisch, R.L. Mieville, *J. Catal.* 90 (1984) 165.

[80]   P. Kowalik, W. Próchniak, M. Konkol, T. Borowiecki, *Appl. Catal.* A (2012) in press.

[81]   M. Saito, K. Murata, *Catal. Surv. Asia* 8 (2004) 285.

[82]   T. Shishido, M. Yamamoto, I. Atake, D. Li, Y. Tian, H. Morioka, M. Honda, T. Sano, K. Takehira, *J. Mol. Catal. A: Chemical* 253 (2006) 270.

[83]   K. Nishida, D. Li, Y. Zhan, T. Shishido, Y. Oumi, T. Sano, K. Takehira, *Appl. Clay Sci.* 44 (2009) 211.

[84]   Y. Li, Q. Fu, M. Flytzani-Stephanopoulos, *Appl. Catal.* B 27 (2000) 179.

[85]   L. Li, L. Song, H. Wang, C. Chen, Y. She, Y. Zhan, X. Lin, Q. Zheng, *Int. J. Hydr. En.* 36 (2011) 8839.

[86]   Y. Amenomiya, I.A. Emesh, K. Oliver, G. Pleizie, *Proc.s of the Ninth International Congress Catal., Chemical Institute of Canada, Ottawa, Canada* (1988) 634.

[87]   L. Kundakovic, M. Flytzani-Stephanopoulos, *J. Catal.* 179 (1998) 203.

[88]   P. Djinović, J. Batista, A. Pintar, *Appl. Catal.* A 347 (2008) 23.

[89]   W. Ruettinger, X. Liu, R. Farrauto, WO Patent 0,141,938 (2002) to Engelhard Co.

[90]   W. Ruettinger, X. Liu, R.J. Farrauto, *Appl. Catal.* B 65 (2006) 135.

[91]   P.V.D.S. Gunawardana, H.C. Lee, D.H. Kim, *Int. J. Hydr. En.* 34 (2009) 1336.

[92]   S. Ratan, C.F. Vales, *Hydr. Proc.* 81 (2002) 57.

[93]   A. Faur Ghenciu, *Curr. Opin. Solid State Mater. Sci.* 6 (2002) 389.

[94]   P. Panagiotopoulou, D.I. Kondarides, *Catal. Today* 112 (2006) 49.

[95]   S. Hilaire, X. Wang, T. Luo, R.J. Gorte, J. Wagner, *Appl. Catal.* A 258 (2004) 271.

[96]   C. Wheeler, A. Jhalani, E.J. Klein, S. Tummala, L.D. Schmidt, *J. Catal.* 223 (2004) 191.

[97]   G. Kolb, H. Pennemann, R. Zapf, *Catal. Today* 110 (2005) 121.

[98]   S. Sharma, P.A. Deshpande, M.S. Hegde, G. Madras, *Ind. Eng. Chem. Res.* 48 (2009) 6535.

[99]   L. Sungkwang, B. Joongmyeon, K. Kihyun., *Int. J. Hydr. En.* 34 (2009) 870.

[100]   A.L. Brenno, G. Camilla, S. Stefania, *Int. J. Hydr. En.* 36 (2011) 7750.

[101]   J. Kugai, J.T. Miller, N. Guo, C. Song, *Appl. Catal.* B 105 (2011) 306.

[102]   C. Mei, Y. Yeung, S.C. Tsang, *J. Phys. Chem. C* 44 (2009) 6074.

[103]   C.M.Y. Yeung, S.C. Tsang, *J. Mol. Catal. A: Chemical* 322 (2010) 17.

[104]   P.A. Deshpande, G. Madras, *J. AIChE* 56 (2010) 2662.

[105]   M. Boaro, M. Vicario, J. Llorca, C. de Leitenburg, G. Dolcetti, A. Trovarelli, *Appl. Catal.* B 88 (2009) 272.

[106]   D.-Woon J. Hari, S.P.H.-Seog Roh, *Catal. Lett.* (2012) in press.

[107]   D.-Woon Jeong, H.S. Potdar, K.-Sun Kim, H.-Seog Roh, *Bull. Korean Chem. Soc.* 32 (2011) 3557.

[108] P. Panagiotopoulou, D.I. Kondarides, *J. Catal.* 225 (2004) 327.

[109] A. Gupta, M.S. Hegde, *Appl. Catal.* B 99 (2010) 279.

[110] C.M. Kalamaras, P. Panagiotopoulou, D.I. Kondarides, A.M. Efstathiou, *J. Catal.* 264 (2009) 117.

[111] P. Panagiotopoulou, D.I. Kondarides, *Appl. Catal.* B 101 (2011) 738.

[112] P. Panagiotopoulou, D.I. Kondarides, *J. Catal.* 267 (2009) 57.

[113] S.C. Ammal, A. Heyden, in *Conf. Proc.,* 09AIChE, Tennessee (USA), 2009.

[114] D.C. Grenoble, M.M. Estadt, D.F. Ollis, *J. Catal.* 67 (1981) 90.

[115] F. Rosa, J.L.G. Fierro, I.D. Gonza, *Catal. Today* 149 (2010) 372.

[116] H.-Seog Roh, D.-Woon Jeong, K.-Sun Kim, I.-Hwan Eum, K. Young, *Catal. Lett.* 141 (2011) 95.

[117] R.J. Gorte, S. Zhao, *Catal. Today* 104 (2005) 18.

[118] N. Mahadevaiah, P. Singh, B.D. Mukri, S.K. Parida, M.S. Hegde, *Appl. Catal.* B 108–109 (2011) 117.

[119] L. Mendelovici, M. Steinberg, *J. Catal.* 96 (1985) 285.

[120] Q. Fu, H. Saltsburg, M. Flytzani-Stephanopoulos, *Science* 301 (2003) 935.

[121] R. Si, M. Flytzani-Stephanopoulos, *Angew. Chem. Int. Ed.* 47 (2008) 2884.

[122] S. Roy, M.S. Hegde, S. Sharma, N.P. Lalla, A. Marimuthu, G. Madras, *Appl. Catal.* B 84 (2008) 341.

[123] P. Bera, K.C. Patil, V. Jayaram, G.N. Subbanna, M.S. Hegde, *J. Catal.* 196 (2000) 293.

[124] X. Wang, R.J. Gorte, *Appl. Catal.* A 247 (2003) 157.

[125] C.J. Shih, Y.J. Chen, M.H. Hon, *Mat. Chem. Phys.* 121 (2010) 99.

[126] H.-Seog Roh, H.S. Potdar, D.-Woon Jeong, K.-Sun Kim, J.-Oh Shim, W.-Jun Jang, *Catal. Today* (2011) 2.

[127] H.S. Potdar, D.W. Jeong, K.S. Kim, *Catal. Lett.* 141 (2011) 1268.

[128] K.-Ran Hwang, J.-Soo Park, S.-Ki Ihm, *Int. J. Hydr. En.* 36 (2011) 9685.

[129] T. Tabakova, V. Idakiev, D. Andreeva, I. Mitov, *Appl. Catal.* A 202 (2000) 91.

[130] D. Andreeva, V. Idakiev, T. Tabakova, A. Andreev, *J. Catal.* 158 (1996) 354.

[131] D. Andreeva, V. Idakiev, T. Tabakova, A. Andreev, R. Giovanoli, *Appl. Catal.* A 134 (1996) 275.

[132] D. Andreeva, V. Idakiev, T. Tabakova, R. Giovanoli, *Bulg. Chem. Comm.* 30 (1998) 64.

[133] D. Andreeva, T. Tabakova, V. Idakiev, P. Christov, R. Giovanoli, *Appl. Catal.* A 169 (1998) 9.

[134] D. Andreeva, V. Idakiev, T. Tabakova, L. Ilieva, P. Falaras, A. Bourlinos, A. Travlos, *Catal. Today* 72 (2002) 51.

[135] H. Sakurai, A. Ueda, T. Kobayashi, M. Haruta, *Chem. Comm.* (2012) 271.

[136] M. Haruta, M. Daté, *Appl. Catal.* A 222 (2001) 427.

[137] T.V. Choudhary, D.W. Goodman, *Top. Catal.* 21 (2002) 25.

[138] J. Hua, K. Wei, Q. Zheng, X. Lin, *Appl. Catal.* A 259 (2004) 121.

[139] T. Tabakova, F. Boccuzzi, M. Manzoli, J.W. Sobczak, V. Idakiev, *Appl. Catal.* B 49 (2004) 73.

[140] J.A. Rodríguez, J. Evans, J. Graciani, J.-B. Park, P. Liu, J. Hrbek, J.F. Sanz, *J. Phys. Chem. C* 113 (2009) 7364.

[141] N.A. Hodge, C.J. Kiely, R. Whyman, M.R.H. Siddiqui, G.J. Hutchings, Q.A. Pankhurst, F.E. Wagner, R.R. Rajaram, S.E. Golunski, *Catal. Today* 72 (2002) 133.

[142] M. Haruta, *Catal. Today* 36 (1997) 153.

[143] M. Shekhar, J. Wang, W.-Sheng Lee, W.D. Williams, S.M. Kim, E.A. Stach, J.T. Miller, W.N. Delgass, F.H. Ribeiro, *J. Am. Chem. Soc.* 134 (2012) 4700.

[144] R. Pilasombat, H. Daly, A. Goguet, J.P. Breen, R. Burch, C. Hardacre, D. Thompsett, *Catal. Today* 180 (2012) 131.

[145] N.K. Gamboa-Rosales, J.L. Ayastuy, M.P. González-Marcos, M.A. Gutiérrez-Ortiz, *Int. J. Hydr. En.* (2012) 1.

[146] D. Andreeva, I. Ivanov, L. Ilieva, M.V. Abrashev, R. Zanella, J.W. Sobczak, W. Lisowski, M. Kantcheva, G. Avdeev, K. Petrov, *Appl. Catal.* A 357 (2009) 159.

[147] B.S. Çağlayan, A.E. Aksoylu, *Catal. Comm.* 12 (2011) 1206.

[148] D. Andreeva, M. Kantcheva, I. Ivanov, L. Ilieva, J.W. Sobczak, W. Lisowski, *Catal. Today* 158 (2010) 69.

[149] Q.-Q. Yu, Y.-Y. Dong, W.-P. Liao, M.-S. Jin, T. He, Z.-H. Suo, Ranliao Huaxue Xuebao, *J. Fuel Chem. Techn.* 38 (2010) 223.

[150] M. Haruta, S. Tsubota, T. Kobayashi, H. Kageyama, M.J. Genet, B. Delmon, *J. Catal.* 144 (1993) 175.

[151] A. Luengnaruemitchai, S. Osuwan, E. Gulari, *Catal. Comm.* 4 (2003) 215.

[152] S. Yang, Y. Zhan, C. Chen, Y. Cao, X. Lin, Q. Zheng, C. Xuebao, *Chinese J. Catal.* 30 (2009) 666.

[153] A.R.S. Rad, M.B. Khoshgouei, A.R. Rezvani, *J. Mol. Catal. A: Chemical* 344 (2011) 11.

[154] V. Idakiev, T. Tabakova, K. Tenchev, *J. Porous Mater.* 19 (2012) 15.

[155] J. Vecchietti, S. Collins, J. Delgado, M. Małecka, E. del Rio, X. Chen, S. Bernal, A. Bonivardi, *Top. Catal.* 54 (2011) 201.

[156] H. Gunes, R. Yildirim, *Int. J. Chem. React. Eng.* 8 (2010) in press.

[157] T. Tabakova, M. Manzoli, D. Paneva, F. Boccuzzi, V. Idakiev, I. Mitov, *Appl. Catal.* B 101 (2011) 266.

[158] T. Tabakova, G. Avgouropoulos, J. Papavasiliou, M. Manzoli, F. Boccuzzi, K. Tenchev, F. Vindigni, T. Ioannides, *Appl. Catal.* B 101 (2011) 256.

[159] A. Venugopal, M.S. Scurrell, *Appl. Catal.* A 258 (2004) 241.

[160] B. Silberova, M. Makkee, J. Moulijn, *Top. Catal.* 44 (2007) 209.

[161] C.H. Kim, L.T. Thompson, *J. Catal.* 230 (2005) 66.

[162] E.M. Fuentes, A. da Costa Faro Júnior, T. de Freitas Silva, J.M. Assaf, M. do C. Rangel, *Catal. Today* 171 (2011) 290.

[163] C.-S. Chen, J.-H. Lin, T.-W. Lai, B.-H. Li, *J. Catal.* 263 (2009) 155.

[164] A.R.S. Rad, M.B. Khoshgouei, S. Rezvani, A.R. Rezvani, *Fuel Proc. Techn.* 96 (2012) 9.

[165] C.-S. Chen, T.-W. Lai, C.-C. Chen, *J. Catal.* 273 (2010) 18.

[166] C.-S. Chen, J.-H. Lin, T.-W. Lai, *Chem. Comm.* 40 (2008) 4983.

[167] B.S. Lim, A. Rahtu, R.G. Gordon, *Nat. Mater.* 2 (2003) 749.

[168] G.C. Chinchen, R.H. Logan, M.S. Spencer, *Appl. Catal.* 12 (1984) 69.

[169] R.L. Keiski, T. Salmi, *Appl. Catal.* A 87 (1992) 185.

3. Experimental session

3.1 Hydrotalcite-type (HT) structure

Hydrotalcite (HT) is an anionic clay also called Layered Double Hydroxide (LDH) containing exchangeable anions in the interlayer space, which was firstly reported with the formula $Mg_6Al_2(OH)_{16}CO_3$-$4H_2O$ in the year 1842 [1]. HT-type compounds have the general formula $[M^{2+}_{1-x} M^{3+}_x(OH)_2]^{x+}A^{n-}_{x/n}$-$mH_2O$, where M^{2+} is a divalent cation (Mg^{2+}, Ni^{2+}, Zn^{2+}, Cu^{2+}, etc.), while M^{3+} is a trivalent cation (Al^{3+}, Cr^{3+}, Fe^{3+}, etc.), and $A^{n-}_{b/n}$ is an anion (CO_3^{2-}, SiO_4^{4-}, NO_3^-, Cl^-, SO_4^{2-}, etc.). Its structure resembles that of brucite, $Mg(OH)_2$, in which Mg^{2+} cations are octahedrally coordinated by hydroxyl ions, sharing the edges and forming layers of octahedra. When the Mg^{2+} cations are replaced by trivalent ions with similar radius (for example, Al^{+3}), a positive charge is generated in the hydroxyl layer; this net positive charge is compensated by anions (for example, CO_3^{2-}), which are located between two brucite-type sheets (Fig. 3.1). Cations, having ionic radii not too different from that of Mg^{2+}, may form HT-type compounds with some exceptions, for example Cu^{2+} ions which form HT-type compounds only with another bivalent cation (Table 3.1). Furthermore, HT-type compounds may exist for the values of x in the range 0.1-0.5, while pure HT-type compounds may be obtained only for $0.20 \leq x \leq 0.33$. X values outside this range lead to an increase in number of neighboring octahedra of the same cation in the brucite-type sheet and formation of metal hydroxides [1].
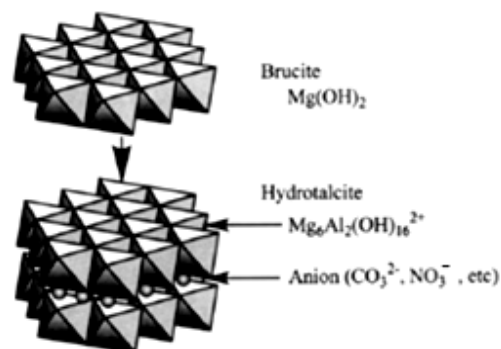

Figure 3.1 Crystal structure of HT-type precursor [1].

Table 3.1 Ionic radius of some cations [1].

M^{2+}	Mg^{2+}	Cu^{2+}	Ni^{2+}	Co^{2+}	Zn^{2+}	Fe^{2+}	Mn^{2+}	Cd^{2+}
Ionic radius (Å)	0.65	0.69	0.72	0.74	0.74	0.76	0.80	0.97
M^{3+}	Al^{3+}	Ga^{3+}	Ni^{3+}	Co^{3+}	Fe^{3+}	Mn^{3+}	Cr^{3+}	In^{3+}
Ionic radius (Å)	0.50	0.62	0.62	0.63	0.64	0.66	0.69	0.81

Recently, HT-type compounds have been intensively studied because of many potential applications, such as anti-acids, catalysts, flame retardants, acid scavengers in polymer composites and raw materials for high temperature insulating porous ceramics. This is due to the fact that they provide mixed oxides by calcination with [1–4]:

1) high surface area;
2) chemical homogeneity and strong Lewis basic sites;
3) very small crystal size, stable to thermal treatments, which may form thermally stable metal crystallites by reduction;
4) ''memory effect'', which allows the reconstruction, under mild conditions, of the original HT-type structure when the product of the thermal treatment is put in contact with water solutions containing various anions.

3.2   Preparation of samples from HT-type precursors

The Cu/Zn/Mg/Al HT-type precursors (Table 3.2) were prepared such as reported in figure 3.2.

1) Preparation of 2M nitrate solution of Cu, Zn, Mg and Al, in the compositions reported in Table 3.2, and 1M solution of sodium hydrocarbonate as precipitant.
2) Co-precipitation by adding slowly the nitrate solution of metals into sodium hydrocarbonate solution, stirred at 60 °C. The pH was carefully kept at 9.0 using drops of 3M NaOH solution. The precipitate was then aged at 60 °C for 45 min.

3) The obtained precipitate was filtered, washed carefully by a large amount of distilled water (400 mL/gHT) at 70 °C, and dried for 12 h at 70 °C.

4) The HT-type precipitate was then ground into powder and calcined at 550 °C for 6 h.

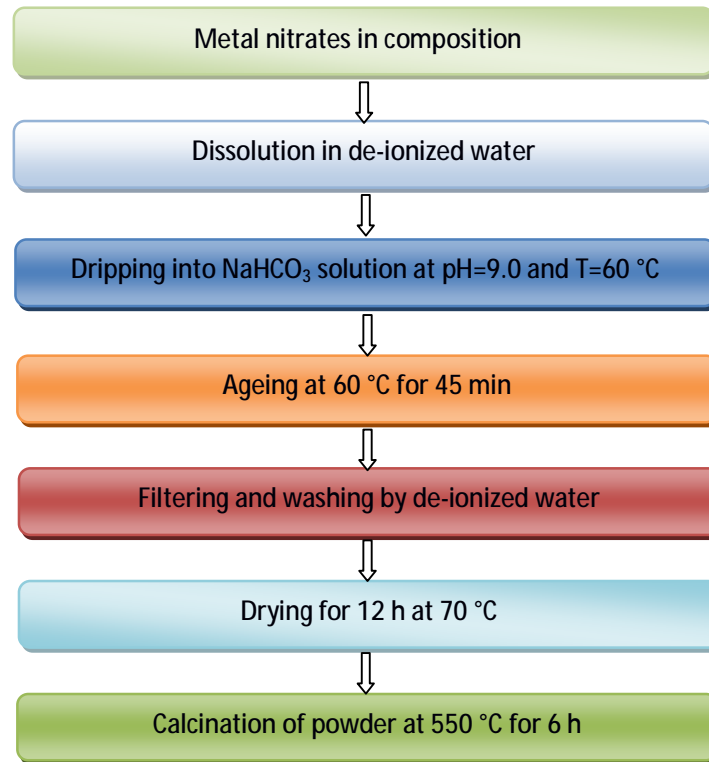

Figure 3.2 Schematic diagram of the sample preparation.

Table 3.2 Nominal composition of the HT-type precursors (the anions are always carbonates).

Sample	Cu/Zn/Mg/Al (at. ratio %)	M^{II}/M^{III}	Zn/Mg	Cu (wt.%)	Zn (wt.%)	Mg (wt.%)	Al (wt.%)
HT-ZAC13c	11.6/63.4/0/25.0	3	–	10.0	56.4	–	9.2
HT-ZAC23c	23.1/51.9/0/25.0	3	–	20.0	46.3	–	9.2
HT-ZAC33c	34.5/40.5/0/25.0	3	–	30.0	36.2	–	9.2
HT-ZAC22c	22.3/44.4/0/33.3	2	–	20.0	41.0	–	12.7
HT-ZAC23cM1	19.6/27.7/27.7/25.0	3	1	20.0	21.2	10.9	10.9

3.3 Characterization methods

3.3.1 X-Ray diffraction analysis (XRD)

The XRD powder analysis has been carried out using a Philips PW1050/81 diffractometer equipped with a graphite monochromator in the diffracted beam and controlled by a PW1710 unit (Cu K_α, λ = 0.15418 nm) (Fig. 3.3). A 2θ range from 5° to 80° has been investigated, using a step size of 0.1° and a time per step of 2 sec.
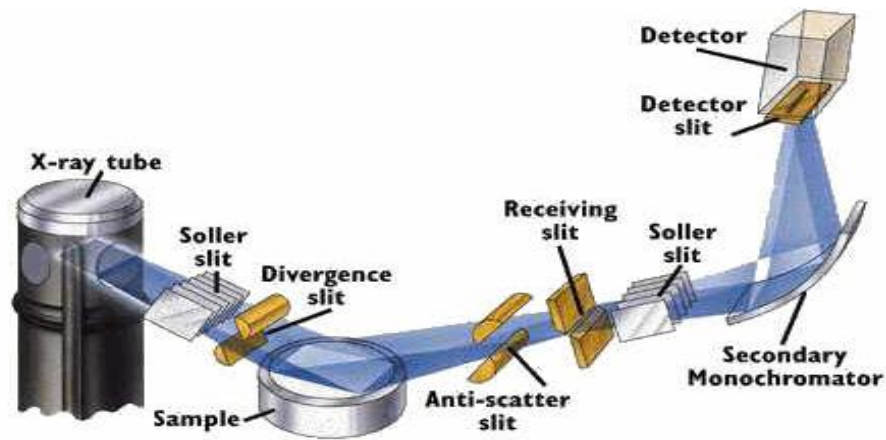

Figure 3.3 Scheme of the instrument for the X-ray diffraction analysis [5].

The phases present in the patterns have been analyzed using the Bragg's law (Equation 3.1 and Fig. 3.4), in order to calculate the d values to be compared with those reported in the literature [4,5] and collected in a database X'Pert Highscore software.

$$n\lambda = 2d\sin\theta \qquad (3.1)$$

where:
- n = order of the reflection (an integer);
- l = wavelength of the X-ray beam incident on a crystal with lattice planes;
- d = distance between atomic layers in a crystal;
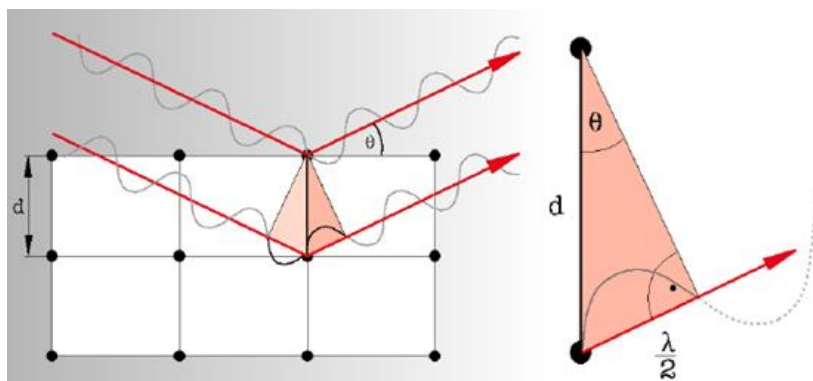- q = diffraction angle.

Figure 3.4 Scheme of X-ray diffraction phenomena [5].

The particle size (*D*) has been calculated using the Debye-Scherrer's formula (Equation 3.2).

$$D = \frac{k\lambda}{\beta \cos \theta}$$

(3.2)

where:

- *k* = a dimensionless constant that may range from 0.89 to 1.39 depending on the specific geometry of the scattering objects, but assumed ≈ 1 because its exact calculation requires a fitting between the obtained diffractograms and that of a perfect crystalline sample;
- λ = wavelength of the incident X-ray beam;
- *b* = *B-b*, the integral breadth of a reflection at the 2θ value, B is the FWHM, while b is the instrumental distortion (i.e. FWHM in the same conditions for a material with crystallite size > 1000 Å);
- *q* = diffraction angle.

3.3.2 Temperature programmed analysis (TPR)

The reduction profiles have been measured using a ThermoQuest Instrument TPD/R/O 1100 Catalytic Surface Analyser, equipped by a Thermal Conductivity Detector (TCD) (Fig. 3.5). The analysis was carried out loading 0.05 g of sample and using the following procedure:

46

1) Pre-treatment: the sample was pre-treated under N_2 (20 mL/min) from room temperature to 150 °C (20 °C/min) and hold for 30 min at 150 °C.

2) Reduction: after cooling until 60 °C, the reduction analysis was performed using a 5 % v/v H_2/Ar gas mixture (20 mL/min) up to 550 °C (10 °C/min) and hold for 60 min at this temperature.
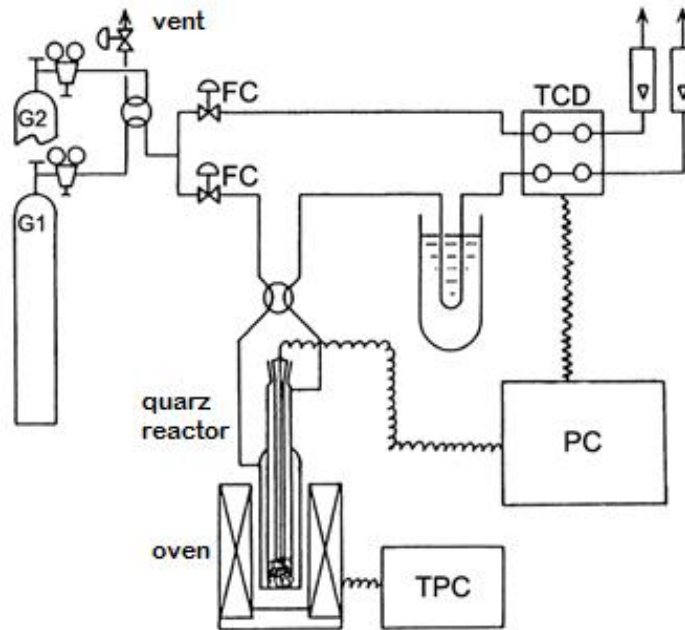

Figure 3.5 Scheme of TPD/R/O instrument.

3.3.3 Surface area and porosity analysis

The surface area values of the catalysts were determined by N_2-physisorption at –196 °C by the Brunauer-Emmet-Teller (BET) method (Equation 3.3) [7], using a Micromeritics ASAP 2020 (Accelerated Surface Area and Porosimetry System). The sample (0.25 g) was pre-treated at 200 °C under vacuum to eliminate impurities and water superficial adsorbed; subsequently, it was analyzed in a liquid N_2 bath.

$$\frac{P}{V(P_0 - P)} = \frac{1}{V_m C} + \frac{C-1}{V_m C} \cdot \frac{P}{P_0}$$

(3.3)

where:

- P = equilibrium pressure;

- P_0 = saturation pressure of adsorbate at the temperature of adsorption;
- V = adsorbed gas quantity (i.e. volume of adsorbed gas per gram of solid at P);
- V_m = monolayer adsorbed gas quantity (adsorbed N_2 volume per gram);
- C = $(E_1\text{-}E_L/RT)$ is the BET constant; E_1 is the heat of adsorption for the first layer, and E_L is that for the second (or higher) layer, assumed to be equal to the heat of liquefaction.

This equation is linear in the range 0.05 < P/P_0 < 0.35 of relative pressure; V_m and C are calculated from the slope value $(C\text{-}1/V_mC)$ and the y-intercept $(1/V_mC)$. The specific surface (S_{BET}, m^2/g) is calculated by the following equation:

$$S_{BET} = \frac{V_m}{V_0} N_A \frac{k}{g_{CAT}}$$
(3.4)

where:
- V_m = monolayer adsorbed gas quantity (adsorbed N_2 volume per gram);
- V_0 = molar adsorbed gas volume;
- N_A = 6.0221418×10^{23} mol^{-1}, Avogadro number;
- k = conversion factor, takes into account also density and molar weight of adsorbed gas;
- g_{CAT} = sample weight.

The porosity analysis has also been carried out using the Micromeritics ASAP 2020. All samples (0.25 g) were previously degassed under vacuum at 150 °C until a pressure of 30 μm Hg was reached and maintained for 30 min. Finally, they were heated up to 250 °C and maintained for 30 min. After the pre-treatment, the sample holder was moved to the analysis section. The N_2 adsorption/desorption analysis at -196 °C followed a protocol that consisted in establishing of list of target pressure at which data were collected. In this case, the instrument uses desorption isothermal curve, i.e. the volume of desorbed N_2, as a function of the relative pressure, calculating the pore volume and size distribution applying the BJH equation (Table 3.3) [7].

Table 3.3 Classification of pore size distribution and appropriate method of analysis.

TYPE	SIZE (nm)	ANALYSIS
Micropores	<2	Gas Physisorption
Mesopores	2-50	Gas Physisorption
Macropores	50-400	Gas Physisorption
Macropores and Interparticle voids	>400	Hg Intrusion

3.3.4 Determination of the specific Cu surface area

The specific Cu surface area was measured using N_2O-chemisorption on the Cu metal surface together with its decomposition (reaction 3.5) [9–16]. The amounts of unreacted N_2O and formed N_2 were determined by a Pulse Chromatography (PC) [11,13].

$$2Cu_s + N_2O \quad " \quad N_2 + Cu_s\text{-}O\text{-}Cu_s \qquad (3.5)$$
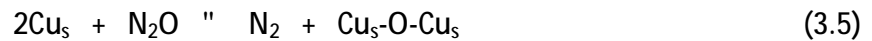
where "s" is a surface atom.

The results strongly depend on the operating conditions (temperature, contact time, concentration of N_2O, size of the particles of Cu, degassing pressure and time, etc.); therefore, they cannot be directly compared with those reported in literature. In this study, the specific area of metallic Cu was calculated from the total amount of N_2O consumption, using a Cu density of 1.46×10^{19} Cu atoms/m^2 and a molar stoichiometry Cu/N_2O=2. The measurement was carried out by loading 100 mg of sample in a small stainless-steel reactor placed inside a GC with a TCD, equipped with a Porapak Q column to separate N_2 and N_2O. The analysis was operated at ambient pressure and described by the following steps (Fig. 3.6):

1) The sample was reduced with a flow of 5 % v/v H_2/N_2 from 40 to 220 °C (10 °C/min) and subsequent hold for 1 h at this temperature.

2) Possible presence of H_2 on sample surface was completely removed by flushing a He stream through the reactor for 20 min and then cooling the catalyst at 60 °C (10 °C / min).

3) The analysis was carried out by introducing successive pulses of 1.0 mL of N_2O into a He flow by a 6-port valve until the N_2O area was constant (10 pulses ca.).
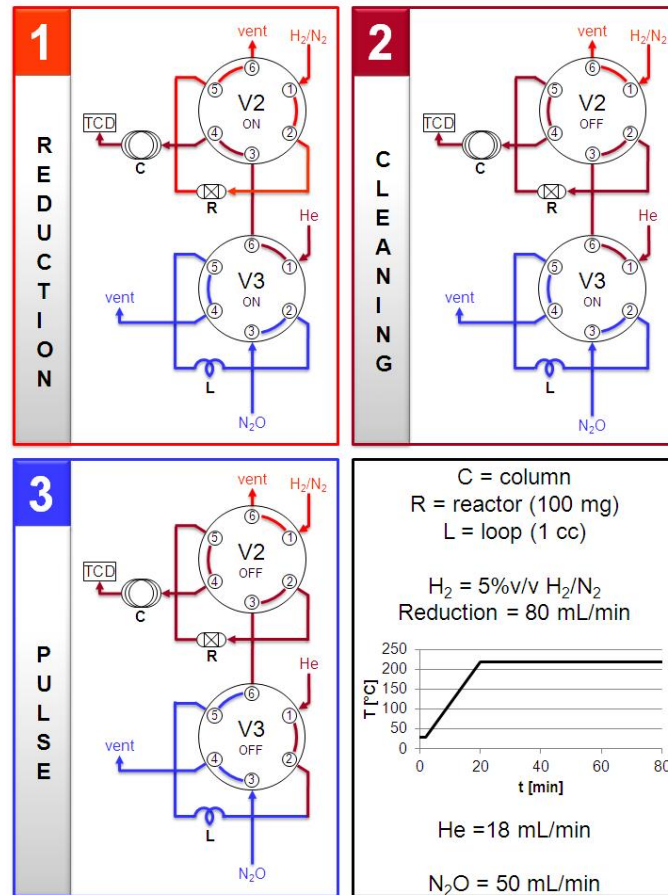

Figure 3.6 Configuration of 6-port valve for the metallic Cu surface analysis (L=loop; R=reactor; C=column).

3.4   Plant specifications

3.4.1 Catalyst shape

The powder of mixed oxides obtained by calcination of HT-type precursors was pressed at 10 tons for 15 min to obtain a tablet, crashed and pelletized to 30-40 mesh to optimize the radial temperature gradient, reducing the diffusion effect ($d_{reactor}/d_{catalyst} \geq 5$). Moreover, the minimum length of catalytic bed was selected to prevent preferential paths, which may change the contact time in real conditions ($d_{reactor}/d_{catalyst} \geq 10$) [16].

3.4.2 Reduction step

Before the catalytic test, the MTS catalyst must be activated by reduction. The activation was performed feeding a mixture of H_2/N_2 at 10 bars, with a Gas Hourly Space Velocity (GHSV) between 300 and 400 h^{-1}. The reduction was described by the following procedure (Fig. 3.7):

1) O_2 present in the reactor was removed completely using flow of N_2 and heating up to 175 °C (1 °C/min) in 90 min.

2) At 175 °C, the reduction started using a flow of 1.2 % v/v H_2/N_2 and hold for 2 h at this temperature.

3) The temperature was then increased to 220 °C (1 °C/min) without changing the composition of the flow gas.

4) At 220 °C, H_2 was added up to 4 % v/v H_2/N_2 and hold for 20 h.

5) The reduction was considered to be finished when a consumption of H_2 less than 0.2 % for a time longer than 2 h was observed, measured by gas chromatography.
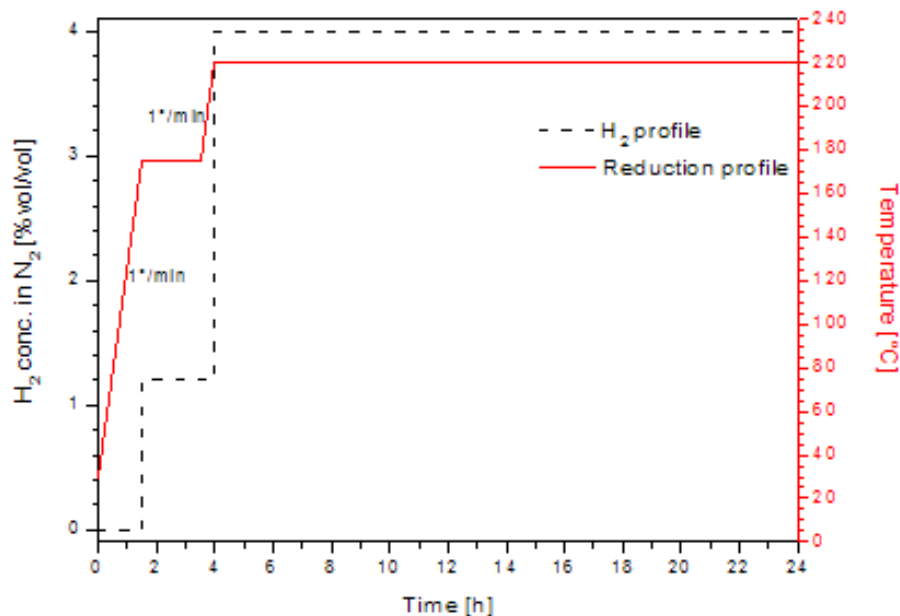

Figure 3.7 Reduction procedure of the MTS catalysts.

3.4.3 Lab-scale Pilot Plant

The catalytic tests were carried out in a laboratory pilot plant, which can be schematized into 4 sections: feed, reaction, separation and analysis section (Fig. 3.8).
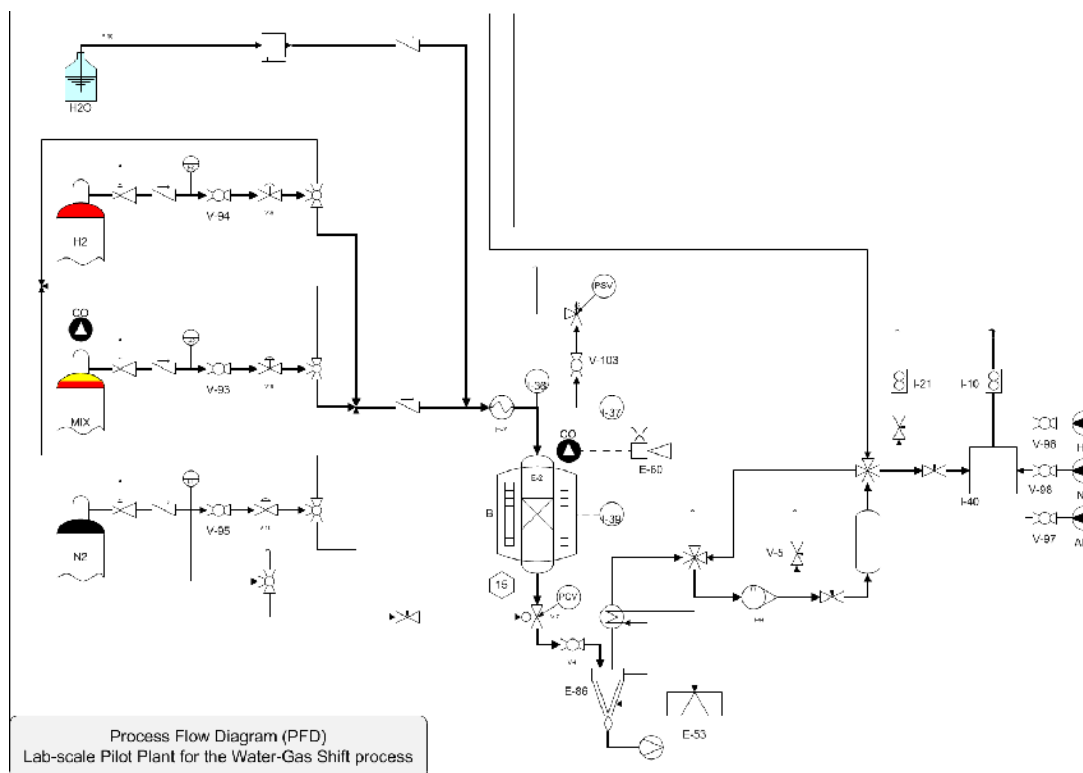

Figure 3.8 Process Flow Diagram (PFD) of the lab-scale pilot plant.

The feed section consisted of three gas lines [N_2, H_2 and Dry Gas (DG)] and one line to feed H_2O. Gas flow rates were controlled by thermal Mass Flow Controllers (MFC), while the flow of distilled H_2O was fed by a HPLC pump. Before being mixed with the DG, H_2O was vaporized at 215 °C. The total gas flow rate was checked again at the exit by drum-type gas-meter to confirm the accuracy of set-up values. Moreover, a by-pass line was used to analyze the composition of inlet gas without crossing the catalyst bed.

The reaction section was composed of a fixed bed tubular reactor (INCOLOY 800HT: 19-23% Cr/30-35% Ni/39.5% Fe/0.06-0.1% C) with an internal diameter of 10 mm, placed vertically inside an electric oven. The temperature profile of catalyst was measured using a thermocouple (cromel/alumel, d = 0.8 mm) inserted inside the reactor. The

catalyst was loaded in the isothermal zone between two layers of inert material (corundum 20 mesh) (Fig. 3.9). The pressure was controlled and maintained constant by a controller placed at the exit of the reactor. The unreacted water was completely separated from the outlet stream by a cooled gas-liquid separator maintained at 0 °C, followed by a trap system filled with a dehydrator agent (drierite, $CaSO_4$, impregnated with a salt of Co as indicator). Finally, the outlet stream was analyzed by a GC equipped with a needle valve to regulate the gas flow into the GC.
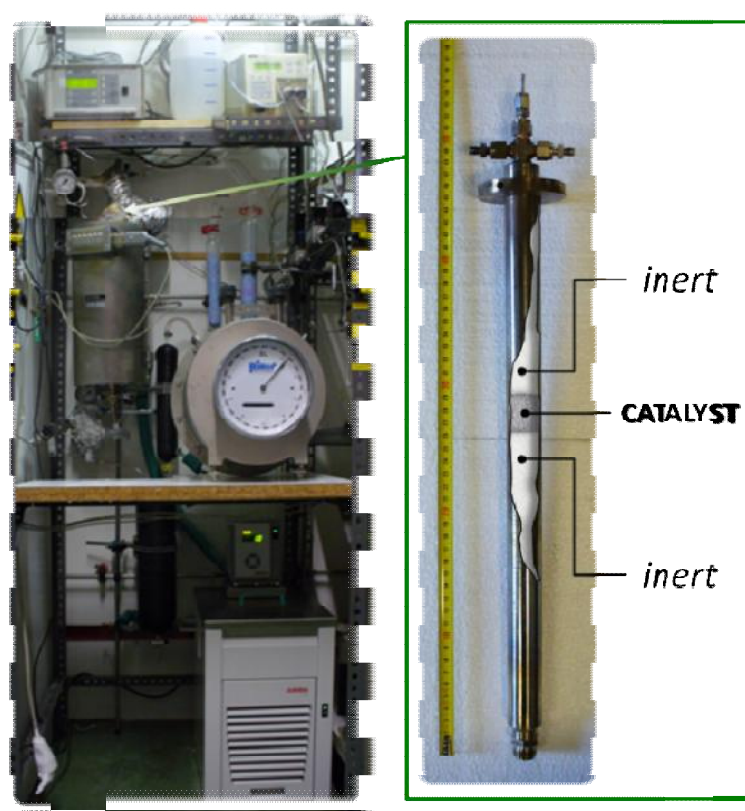

Figure 3.9 Pictures of the lab-scale pilot plant and tubular reactor.

3.4.4 Activity Tests

The activity tests simulated the industrial conditions, which depend on different parameters (Table 3.4): pressure (P), temperature measured at the outlet of the catalytic bed (T), Steam to Dry Gas ratio (S/DG) and contact time (τ). The study was focused not only on the activity test at middle temperature, but also to optimize the reaction

conditions with low S/DG ratio and contact time values, thus ensuring a lower overhead of the plant. Moreover, to evaluate the stability with Time-Of-Stream (TOS), all catalysts were tested for 100 h at 300 °C, τ = 1.0 sec and the lower S/DG ratio (0.25).

Table 3.4 List of the tests carried out for the WGS process.

OPERATING CONDITIONS		WET GAS		FLOW CONDITIONS	
T_{exp} (°C)	P_{exp} (°C)	S/DG (v/v)	S/C (v/v)	τ (s)	GHSV (h^{-1})
250	15	0,55	1,96	0,50	7200
250	15	0,55	1,96	1,00	3600
250	15	0,25	0,89	1,00	3600
300	15	0,55	1,96	0,25	14400
300	15	0,55	1,96	0,5	7200
300	15	0,55	1,96	1,00	3600
300	15	0,25	0,89	1,00	3600
350	15	0,55	1,96	0,50	7200
350	15	0,55	1,96	1,00	3600
350	15	0,25	0,89	1,00	3600

3.5   Quali-quantitative analysis

3.5.1   Gas Chromatography

The composition of outlet gas was determined using an online GC (PERKIN ELMER Auto System XL), equipped with a Carbosphere 80/100 packed column (6 ft x 1/8 in. outer diameter), able to separate H_2, CO, CO_2 and CH_4 at 120 °C. The H_2 amount was detected by a TCD (carrier gas = N_2) whereas CO, CO_2 and CH_4 were detected by a Flame Ionization Detector (FID), with a methanator before to convert CO and CO_2 into CH_4, detectable by the FID (Fig. 3.10). A six-port valve was used to inject a constant volume into the column using a sampling loop of 1.0 mL (Fig. 3.11).
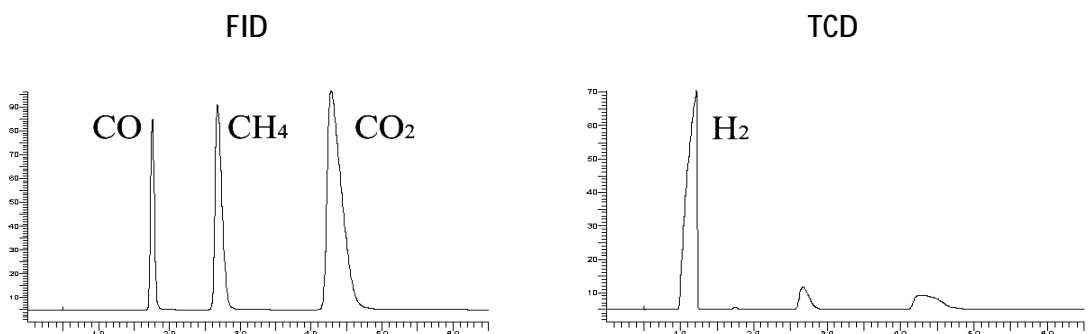
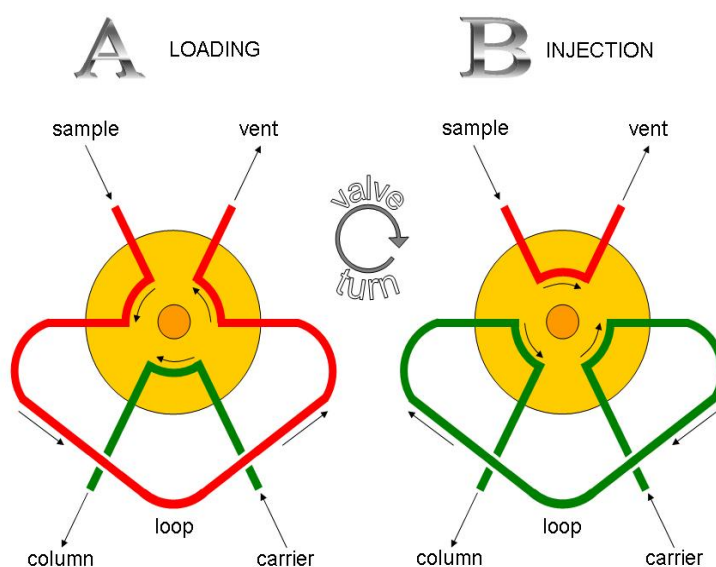Figure 3.10 Examples of typical FID and TCD chromatograms of outlet synthesis gas.

Figure 3.11 6-port valve to inject flow non-stop: (A) LOAD position; (B) INJECT position.

3.5.2 Data elaboration

The data obtained from the GC analysis showing the DG composition after reaction, together with the total amount of condensed water, allow to calculate the conversion (χ), selectivity (S), yield (Υ) and mass balance ($C_{OUT/IN}$) values, by using the following formulas:

CO conversion
$$\chi_{CO} = \frac{[CO]^{IN} - [CO]^{OUT}}{[CO]^{IN}} \, 100 = 1 - \frac{[CO]^{OUT}}{[CO]^{IN}} \, 100 = \left(1 - \frac{\%CO^{OUT} F_{DG}^{OUT}}{\%CO^{IN} F_{DG}^{IN}}\right) 100$$
H$_2$O conversion
$$\chi_{H2O} = \frac{[H2O]^{IN} - [H2O]^{OUT}}{[H2O]^{IN}} \, 100 = 1 - \frac{[H2O]^{OUT}}{[H2O]^{IN}} \, 100 = \left(1 - \frac{V_{H2O}^{OUT} \, 1{,}006}{F_{H2O}^{IN} t_{STREAM}}\right) 100$$
Selectivity
$$S_j = \frac{[j]}{[CO]^{IN} - [CO]^{OUT}} \, 100 = \frac{[j]^{OUT} - [j]^{IN}}{[CO]^{IN} - [CO]^{OUT}} \, 100 = \left(\frac{\%j^{OUT} F_{DG}^{OUT} - \%j^{IN} F_{DG}^{IN}}{\%CO^{IN} F_{DG}^{IN} - \%CO^{OUT} F_{DG}^{OUT}}\right) 100$$ *where j = CO$_2$,CH$_4$,H$_2$*
H$_2$ yield
$$\gamma_{H2} = \frac{[H2]}{[CO]^{IN}} \, 100 = \frac{[H2]^{OUT} - [H2]^{IN}}{[CO]^{IN}} \, 100 = \left(\frac{\%H2^{OUT} F_{DG}^{OUT} - \%H2^{IN} F_{DG}^{IN}}{\%CO^{IN} F_{DG}^{IN}}\right) 100$$ $$\gamma_{H2} = \frac{[H2]}{[CO]^{IN}} \, 100 = \frac{[H2]}{[CO]^{IN} - [CO]^{OUT}} \frac{[CO]^{IN} - [CO]^{OUT}}{[CO]^{IN}} \, 100 = \frac{\chi_{CO} S_{H2}}{100}$$
C balance
$$\%C_{OUT/IN} = \frac{[CO]^{OUT} + [CH4]^{OUT} + [CO2]^{OUT}}{[CO]^{IN} + [CH4]^{IN} + [CO2]^{IN}} \, 100$$ $$= \left(\frac{\%CO^{OUT} + \%CH4^{OUT} + \%CO2^{OUT}}{\%CO^{IN} + \%CH4^{IN} + \%CO2^{IN}} \frac{F_{DG}^{OUT}}{F_{DG}^{IN}}\right) 100$$

Nomenclature

%CO^{IN} = Inlet percentage of CO	%CO^{OUT} = Outlet percentage of CO
%CH$_4$^{IN} = Inlet percentage of CH$_4$	%CH$_4$^{OUT} = Outlet percentage of CH$_4$
%CO$_2$^{IN} = Inlet percentage of CO$_2$	%CO$_2$^{OUT} = Outlet percentage of CO$_2$
%H$_2$^{IN} = Inlet percentage of H$_2$	%H$_2$^{OUT} = Outlet percentage of H$_2$
F$_{DG}$^{IN} = Inlet flow of Dry Gas	F$_{DG}$^{OUT} = Outlet flow of Dry Gas
F$_{H2O}$^{IN} = Inlet flow of H$_2$O	V$_{H2O}$^{OUT} = Outlet volume of H$_2$O
t$_{STREAM}$ = time of stream	

References

[1]   F. Cavani, F. Trifirò, A. Vaccari, *Catal. Today* 11 (1991) 173.

[2]   J.I. Di Cosimo, V.K. Díez, M. Xu, E. Iglesia, C.R. Apesteguía, *J. Catal.* 178 (1998) 499.

[3]   M.J. Climent, A. Corma, S. Iborra, J. Primo, *J. Catal.* 151 (1995) 60.

[4]   K. Takehira, *Catal. Surv. Japan* 6 (2003) 19.

[5]   H.P. Klug, L.E. Alexander, *X-Ray Diffraction Procedures*, Wiley, New York (USA), 1974.

[6]   *Powder Diffraction File, Inorganic Phases*, International Centre for Diffraction Data, Swarthmore PA (USA), 1991.

[7]   J.S. Gregg, K.S.W. Sing, *Adsorption, Surface Area and Porosity*, New York (USA), 1982.

[8]   R.M. Dell, F.S. Stone, P.F. Tiley, *Trans. Farad. Soc.* 49 (1953) 195.

[9]   T.J. Osinga, B.G. Linsen, W.P. van Beek, *J. Catal.* 7 (1967) 277.

[10]   B. Dvořák, J. Pašek, *J. Catal.* 18 (1970) 108.

[11]   J.J.F. Scholten, J.A. Konvalinka, *Trans. Farad. Soc.* 65 (1969) 2465.

[12]   J.W. Evans, N.W. Cant, D.L. Trimm, M.S. Wainwright, *Appl. Catal.* 6 (1983) 355.

[13]   K. Narita, N. Takezawa, H. Kobayashi, I. Toyoshima, *React. Kinet. Catal. Lett.* 19 (1982) 91.

[14]   G. Sengupta, D.K. Gupta, M.L. Kundu, S.P. Sen, *J. Catal.* 67 (1981) 223.

[15]   G.C. Chinchen, C.M. Hay, H.D. Vandervell, K.C. Waugh, *J. Catal.* 103 (1987) 79.

[16]   D. Sanfilippo, *Catal. Today* 34 (1997) 259.

4.   Results and Discussion

It has been reported that the performances of the Cu/ZnO/Al$_2$O$_3$ catalysts in the WGS reaction are significantly affected by the Cu particle properties [1] and synergetic interactions between Cu and ZnO [2-4], probably depending on the Cu and Zn contents [5,6]. High amounts of Cu favor the WGS reaction at low temperature, while the increase of temperature favors the side reactions and sintering [7]. Furthermore, supported catalysts with a Cu content lower than 30 wt.% may show high activity, selectivity and resistance to sintering [8]. To evaluate the effect of Cu content on the WGS activity, three catalysts (ZAC13c, ZAC23c and ZAC33c) were prepared from HT-type precursors, maintaining the molar ratio (Cu+Zn)/Al = 3.00 and changing the Cu and Zn contents [9,10].

Al content affects the precursor structure and active phase availability [11], and an amount of Al from 0.20 to 0.33 mol/mol is necessary to obtain pure HT-type compounds [9,12]. Thus, the role of Al was investigated by studying two catalysts with molar ratios M^{II}/M^{III} of 2.00 and 3.00 (ZAC22c and ZAC23c), keeping the amount of Cu constant.

In order to define the role of the Cu surface area and ZnO, this latter was partially substituted by MgO in the HT-type precursor [13], to obtain a Zn/Mg molar ratio of 1.00 (ZAC23cM1), maintaining unchanged the Cu amount and M^{II}/M^{III} ratio.

4.1   Role of Cu content

4.1.1   Characterization of precursors and catalysts

Figure 4.1 shows the XRD patterns of the precursors with different Cu contents, presenting HT-type and ZnO phases in all the samples, while malachite [Cu$_2$(CO$_3$)(OH)$_2$] is only observed for HT-ZAC33c, with the highest Cu content. Furthermore, the HT-type peaks in HT-ZAC13c and HT-ZAC23c are more intense than those in ZAC33c, suggesting that the HT-type structure is better organized in the catalysts with lower Cu contents. However, the highest BET surface area (Table 4.1) is observed for HT-ZAC33c. The XRD patterns of the calcined HT-type precursors (Fig. 4.2) show the decomposition to ZnO,

without evidences of Cu-containing species, with the exception of ZAC33c, in which also CuO is formed. This may be justified by the fact that the high Cu amount is not stabilized inside the HT-type structure.
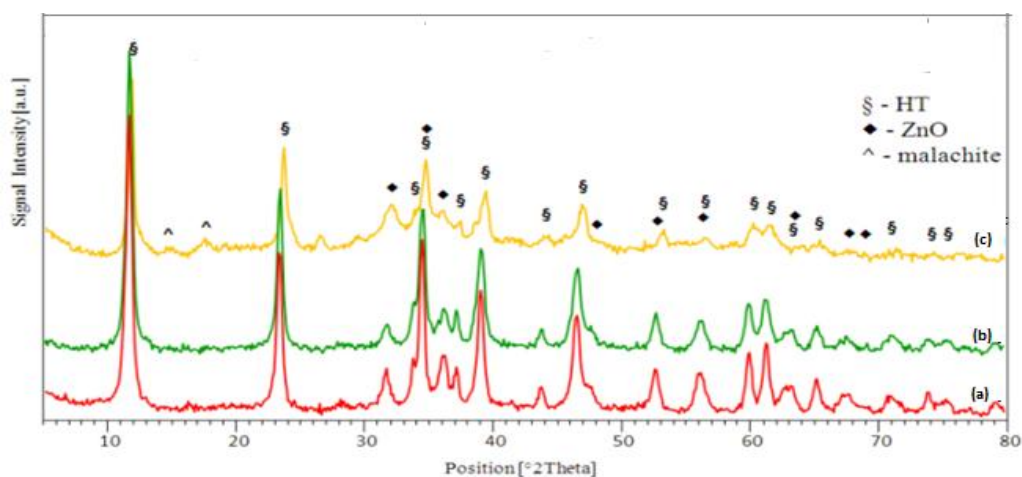

Figure 4.1 XRD patterns of the HT-type precursors: (a): HT-ZAC13c; (b): HT-ZAC23c; (c): HT-ZAC33c.

Table 4.1 Characterization of the HT-type precursors.

Sample	Cu (wt.%)	Phase detected by XRD	d_{HT} (003) (nm)	BET surface area (m^2/g)
HT-ZAC13c	10	HT and ZnO	31	26
HT-ZAC23c	20	HT and ZnO	33	32
HT-ZAC33c	30	HT, ZnO and malachite	35	42

Table 4.2 shows the surface area and porosity of the calcined samples (before and after reaction), determined by either BET or N_2O-chemisorption methods. Unlike to that previously reported for the HT-type precursors, the calcined samples exhibit decreases in BET surface area and Cu dispersion by increasing the Cu content.
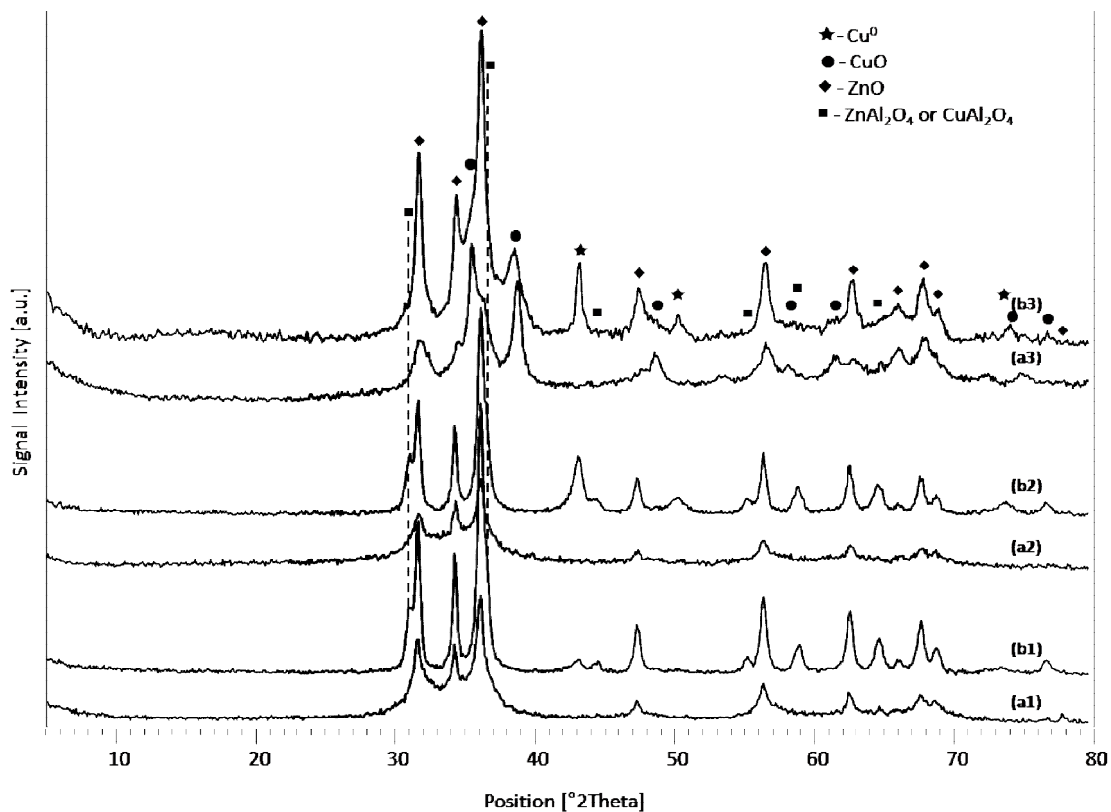
Figure 4.2 XRD patterns of the calcined HT-type precursors before and after reaction: (a1): ZAC13c before reaction; (a2): ZAC23c before reaction; (a3): ZAC33c before reaction; (b1): ZAC13c after reaction; (b2): ZAC23c after reaction; (b3): ZAC33c after reaction.

Table 4.2 Characterization of the calcined HT-type precursors before and after reaction.

Sample		Phase detected by XRD	BET surface area (m^2/g)	Cu surface area (m^2/g_{cat})	Cu surface area (m^2/g_{Cu})	D_{Cu} (%)	Pore volume (cm^3/g)	Pore diameter (nm)
ZAC13c	before	ZnO	62	3.5	35.0	5.4	0.34	20
	after	ZnO, spinel, CuO (trace), Cu^0(trace)	34	3.1	35.0	4.8	0.33	31
ZAC23c	before	ZnO	48	4.9	24.5	3.8	0.35	28
	after	ZnO, spinel, CuO (trace), Cu^0	34	5.1	25.5	3.9	0.35	34
ZAC33c	before	ZnO and CuO	22	3.9	13.0	2.0	0.16	27
	after	Cu^0, CuO, ZnO, spinel	18	3.9	13.0	2.0	0.14	24

The TPR profiles of Cu-based catalysts represent the reduction of different Cu^{2+} species, in interaction with various oxides (Table 4.3) [14-19]. The TPR profiles of the calcined HT-type precursors show a complete reduction at about 350 °C, attributed to the transformation of Cu^{2+} to Cu^0 (Figure 4.3). The reduction peak, asymmetric and with a tail towards lower temperature, may be assigned to the overlap of reduction processes of different Cu^{2+} species [20,21]. Maximum of the reduction peaks occurs between 280-320 °C and moves to higher temperature by increasing the Zn content. ZnO may enhance the reducibility of Cu phases by formation of highly dispersed Cu particles on ZnO or reduce it by strong interactions between Cu and the support (such as observed in the present catalysts). Moreover, ZnO does not show any reduction peak up to 350 °C [22].

Table 4.3 Reduction of the Cu species as a function of the temperature [14-19].

Cu species	Reduction temperature (°C)	Description	Reduction process
Surface CuO	160-250	well-dispersed metal particles	$Cu^{2+} \rightarrow Cu^{1+}$ Cu^{2+} or $Cu^{1+} \rightarrow Cu^0$
CuO	250-330	CuO dissolved in ZnO lattice, structural CuO	Cu^{2+} or $Cu^{1+} \rightarrow Cu^0$
Spinel of Cu	400-600	Cu^{2+} in the matrix	$Cu^{2+} \rightarrow Cu^0$

The reflections of ZnO, spinel, CuO and metallic Cu are observed in all the samples after reaction (Fig. 4.2). The lines of the spinel become broader from ZAC13c to ZAC23c and almost disappear in ZAC33c, suggesting that part of Cu is inside the spinel before reaction in the catalysts with low Cu contents. The small CuO and high Cu amounts for the spent ZAC33c suggest a surface reoxidation (passivation) of large Cu^0 particles.

The TPR profiles of the spent catalysts (Fig. 4.3) are shifted towards lower temperature (about 60-80 °C) than in the catalysts before reaction, due to weaker interactions between the Cu-containing species and the support after reaction. For all the samples, the peak at high temperature (about 550 °C) may be attributed to the reduction of Cu spinel ($CuAl_2O_4$), suggesting that it does not participate to the reaction [23].
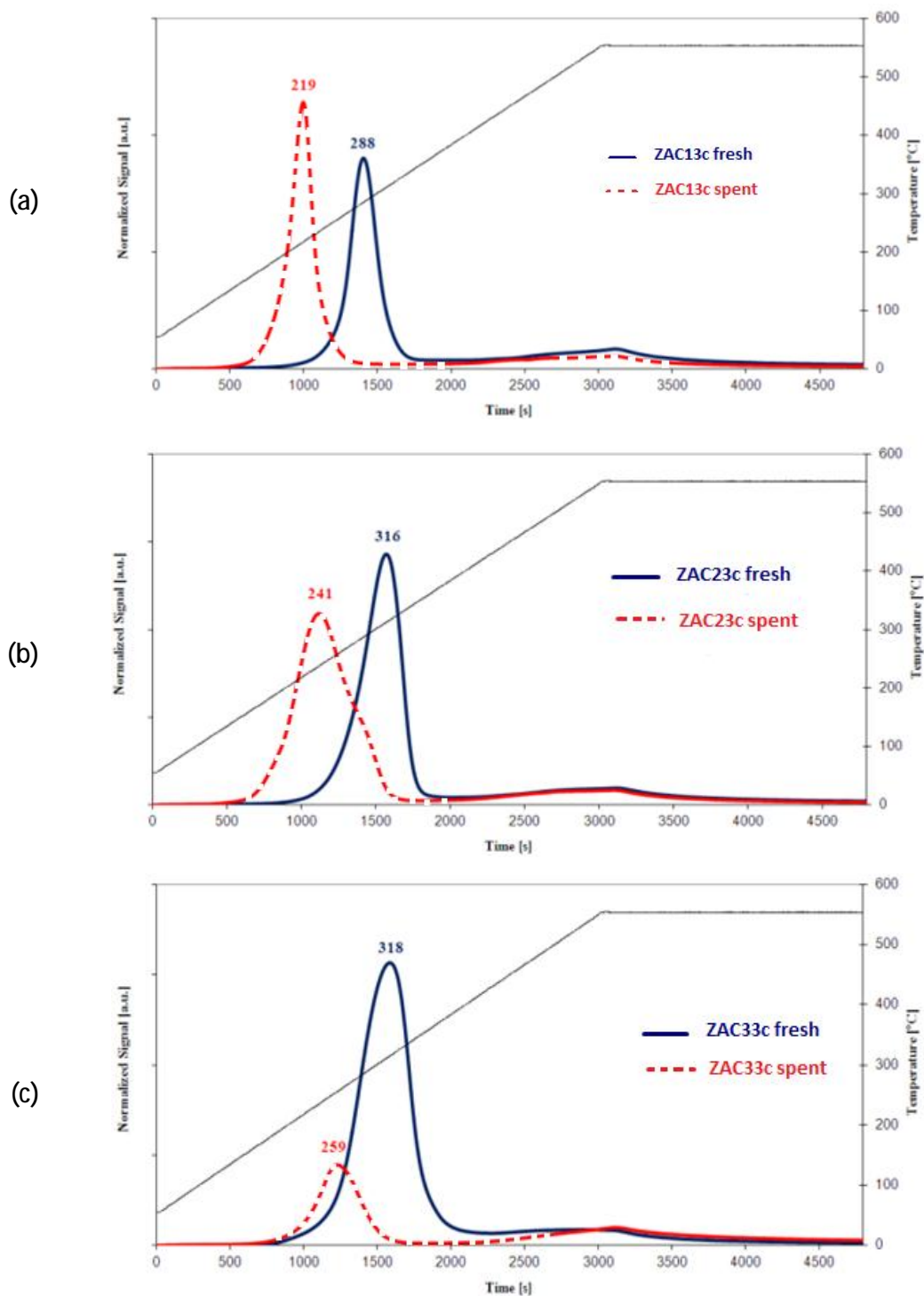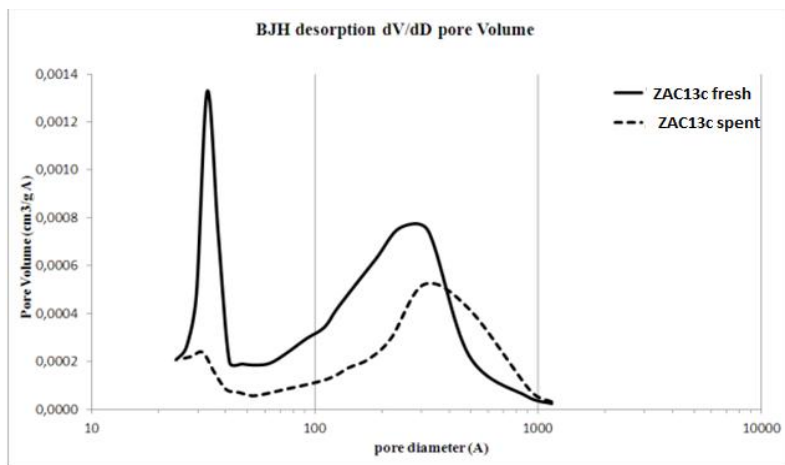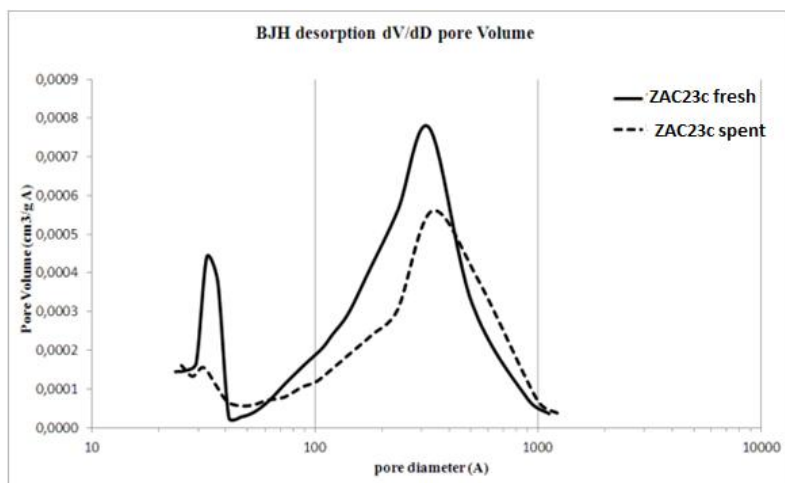
Figure 4.3 TPR profiles of the catalysts before (fresh) and after (spent) reaction: (a): ZAC13c; (b): ZAC23c; (c): ZAC33c
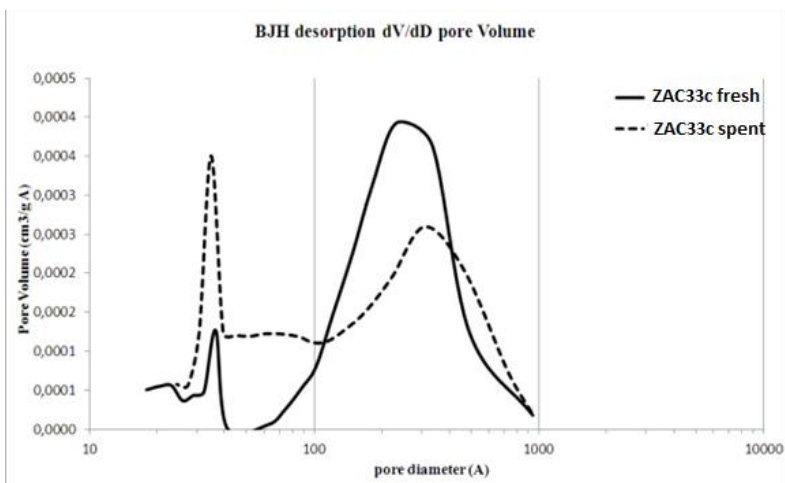
(a)

(b)

(c)

Figure 4.4 BJH pore distribution of the catalysts before (fresh) and after (spent) reaction: (a): ZAC13c; (b): ZAC23c; (c): ZAC33c.

All the catalysts show a decrease of BET surface area after reaction, may be due to the sintering phenomena (Table 4.2). Considering its low Cu^0 surface area per gram of catalyst (although with the best value per gram of Cu), the high catalytic activity of ZAC13c (see next section 4.1.2) may be mainly attributed to synergetic interactions between Cu and ZnO [24]. ZAC23c presents the highest Cu^0 surface area per gram of catalyst, leading to the highest CO conversion among the three catalysts (best compromise between Cu surface area and Cu/ZnO interactions), while the very low activity of ZAC33c may be due to the low Cu dispersion.

The pore distributions of the samples are shown in figure 4.4, in which the presence of small pores (2-4 nm) is significant in ZAC13c and decreases with the Cu content. After reaction, all the samples show the disappearance of the 3-4 nm pores, a decrease of pores with diameter of 10-40 nm and a corresponding formation of larger pores. The adsorption isotherms of the catalysts (not shown) belong to type 4 of IUPAC classification, characteristics of 2-50 nm mesopores. Notwithstanding the decrease in surface areas, the pore volumes remain constant in all the samples, showing a partial collapse of the small pores and formation of larger ones (Table 4.2).

4.1.2 Catalytic activity

The effect of Cu content on the catalytic activity is studied using the three catalysts, ZAC13c, ZAC23c and ZAC33c, (10, 20 and 30 wt.% of Cu, respectively), pelletized to 30-40 mesh. Before the tests, they were activated by reduction as described in section 3.4.2. The activity data are summarized in Table 4.4.

Table 4.4 CO conversion and H_2 yield for the catalysts with different Cu contents.

				250	250	250	300	300	300	300	350	350	350
	T	[°C]	250	250	250	300	300	300	300	350	350	350
	S/DG	[V/V]	0.55	0.25	0.55	0.55	0.55	0.25	0.55	0.55	0.25	0.55
	τ	[sec]	0.50	1.00	1.00	0.25	0.50	1.00	1.00	0.50	1.00	1.00
ZAC13c	CO Conv.	[%]	76	58	89	83	93	76	93	88	60	88
	H_2 Yield	[%]	76	55	89	83	91	73	92	86	58	86
ZAC23c	CO Conv.	[%]	86	68	92	82	92	77	92	87	69	87
	H_2 Yield	[%]	86	67	86	80	91	74	92	80	67	84
ZAC33c	CO Conv.	[%]	24	21	37	27	48	43	62	69	57	75
	H_2 Yield	[%]	24	24	37	25	45	42	64	69	57	75

(a)

(b)
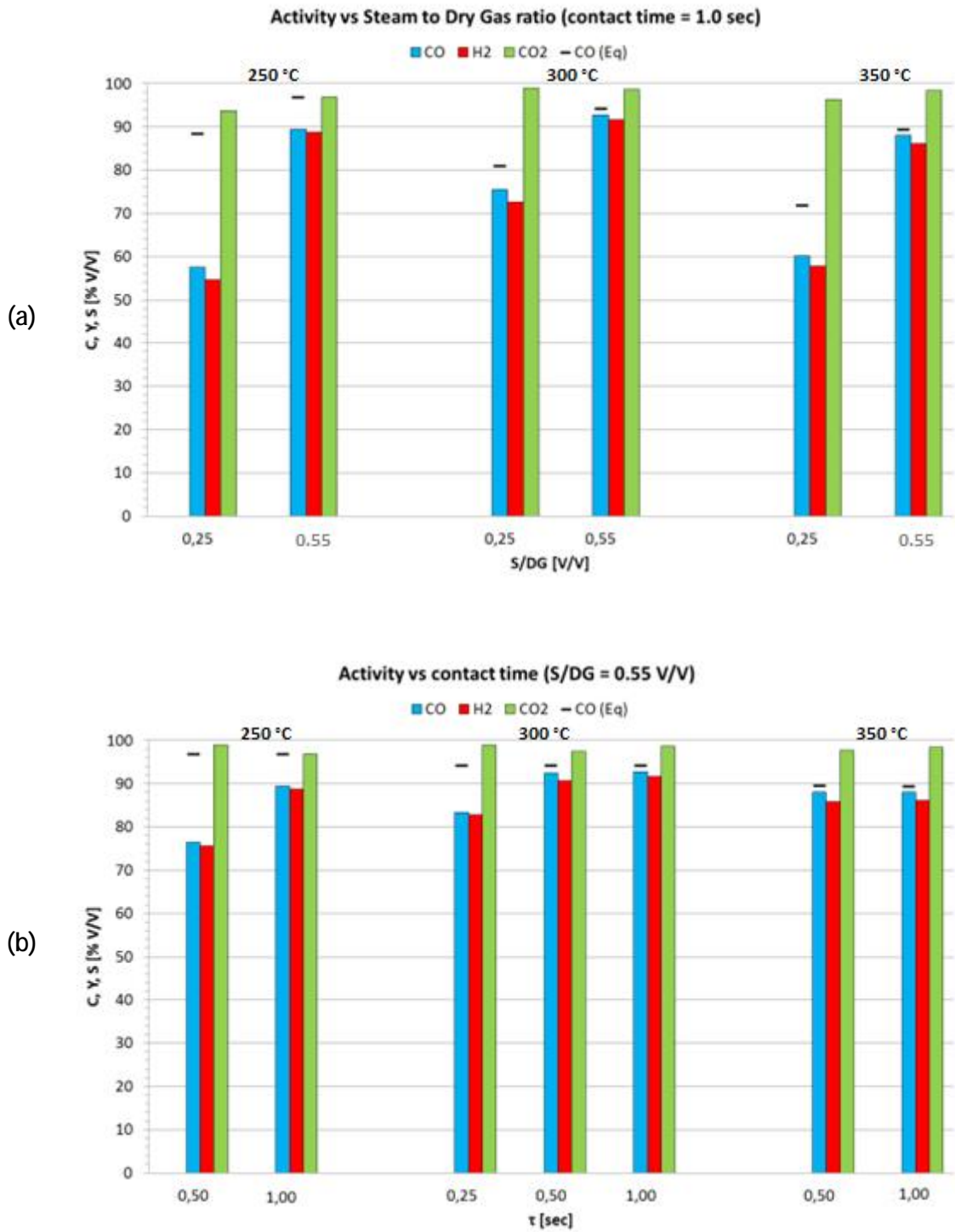
Figure 4.5 Activity of ZAC13c as a function of S/DG (a) and contact time (b)

The catalyst ZAC13c shows a good catalytic activity at all the temperatures. The decrease of S/DG ratio (Fig. 4.5a), from 0.55 to 0.25 v/v, worsens the catalytic performances at all the temperatures: for example, at 250 °C and with a contact time (τ) of 1.00 sec, the CO conversion decreases from 89 to 58 %. At 300 °C, with reaction conditions (S/DG = 0.55 v/v; τ = 0.50 and 1.00 sec) similar to those used in the industrial plants, the CO conversion reaches the equilibrium values (Fig. 4.5b). At higher temperature (350 °C), the contact time has a slight influence on the catalytic performances, while at 300 °C and 0.25 sec, a remarkable reduction of CO conversion may be observed. At 250 °C, the catalyst is sensitive to changes of the contact time, and the CO conversion decreases from 89 to 76 % as the contact time reduces from 1.00 to 0.50 sec (Fig. 4.6). The yield of H_2 shows the same trends of CO conversion in all operating conditions, together with high selectivity in CO_2 (> 97 %), allowing to exclude the presence of significant side reactions.
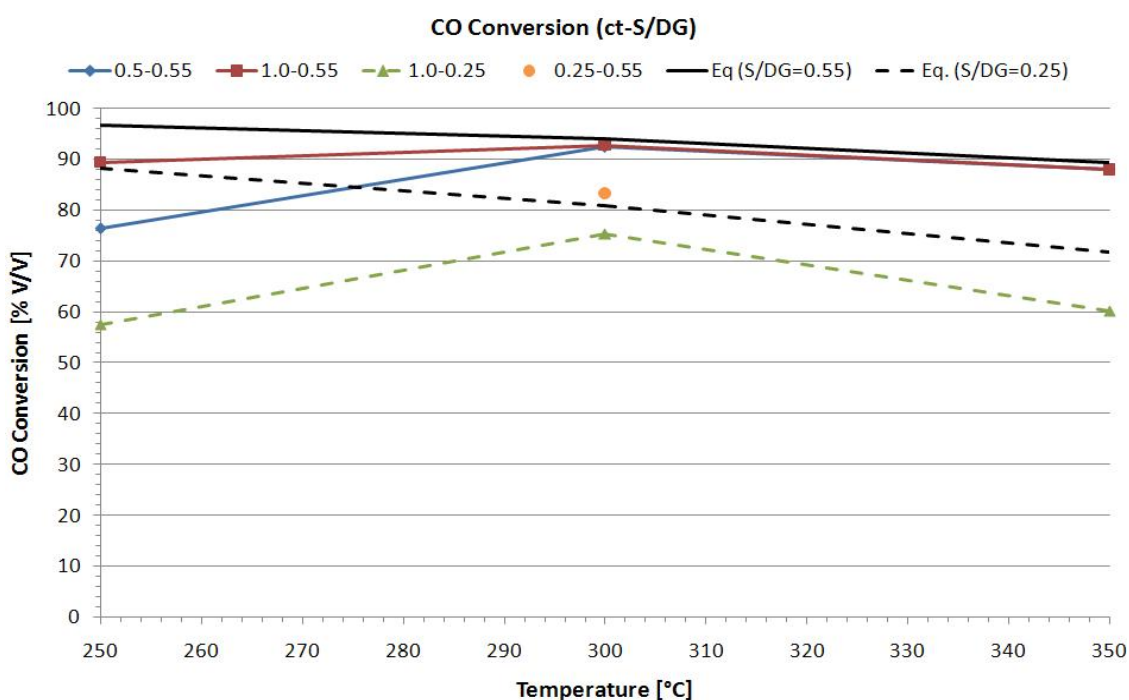

Figure 4.6 CO conversion of ZAC13c at different contact time, S/DG and temperature values.
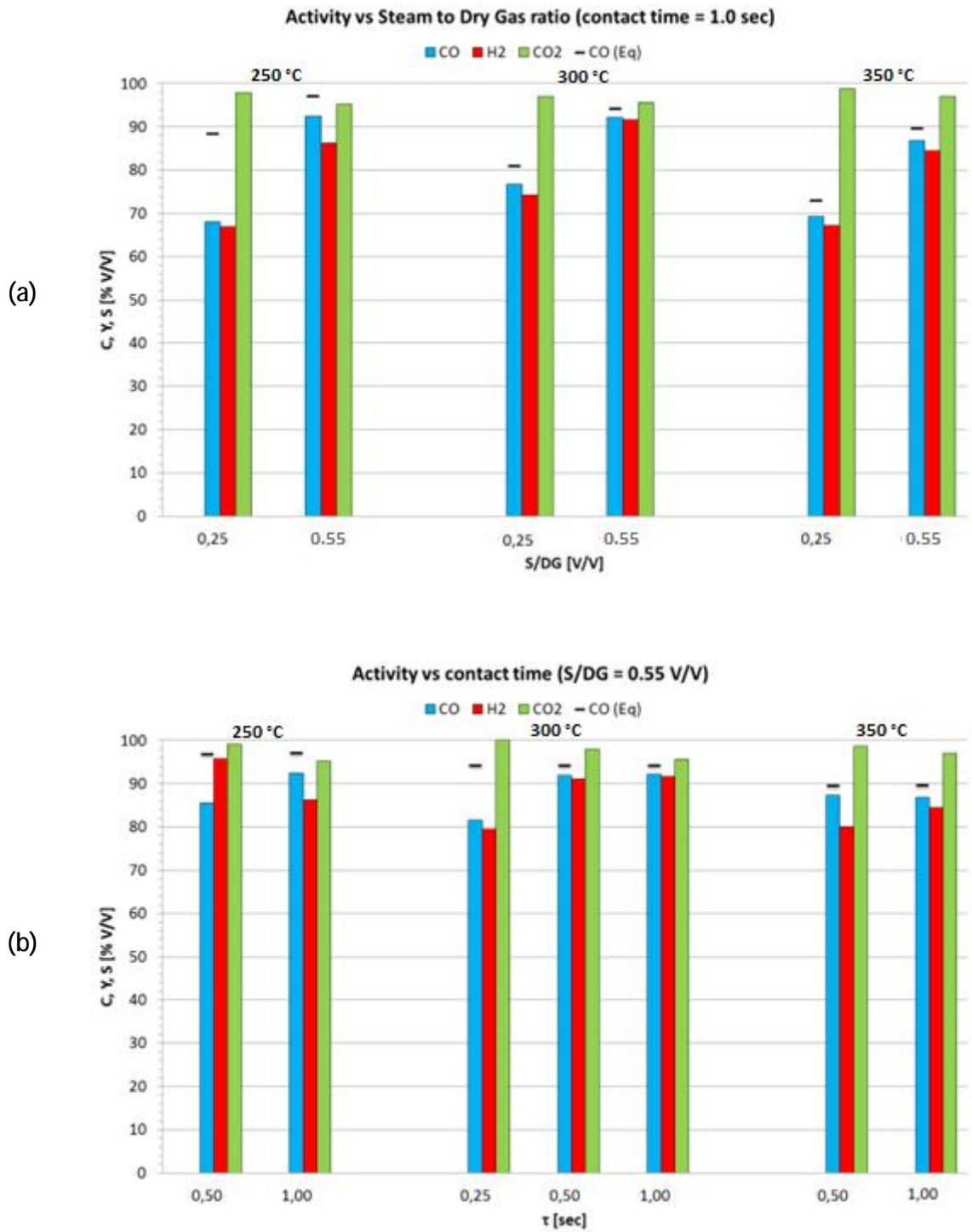
(a)

(b)

Figure 4.7 Activity of ZAC23c as a function of S/DG (a) and contact time (b)

The catalyst ZAC23c, in which the Cu content is two times higher than that in ZAC13c, shows an improvement in catalytic activity at 250 °C, with 86 % of CO conversion compared to 76 % in ZAC13c (S/DG=0.55 v/v; τ=0.50 sec) (Table 4.4). As for ZAC13c, the decrease of S/DG ratio (Fig. 4.7a) affects negatively the catalytic performances, the CO conversion decreasing from 92 to 68 % when the S/DG changes from 0.55 to 0.25 v/v (T = 250 °C). At higher temperature, the influence of S/DG on the activity is lower than for ZAC13c, and CO conversion and H_2 yield achieve the equilibrium values. Unlike to that previously reported for ZAC13c, the contact time has a lower influence on the catalytic performances at 250 °C (Fig. 4.7b), with the CO conversion almost unchanged (≈ 93 %) as the contact time reduces from 1.00 to 0.50 sec. At 300 °C, significant decreases in CO conversion and H_2 yield are observed only at very low contact time (0.25 sec) (Fig. 4.8). Considering the trends of both CO conversion and H_2 yield, no evidence of side reactions is observed also for this catalyst.
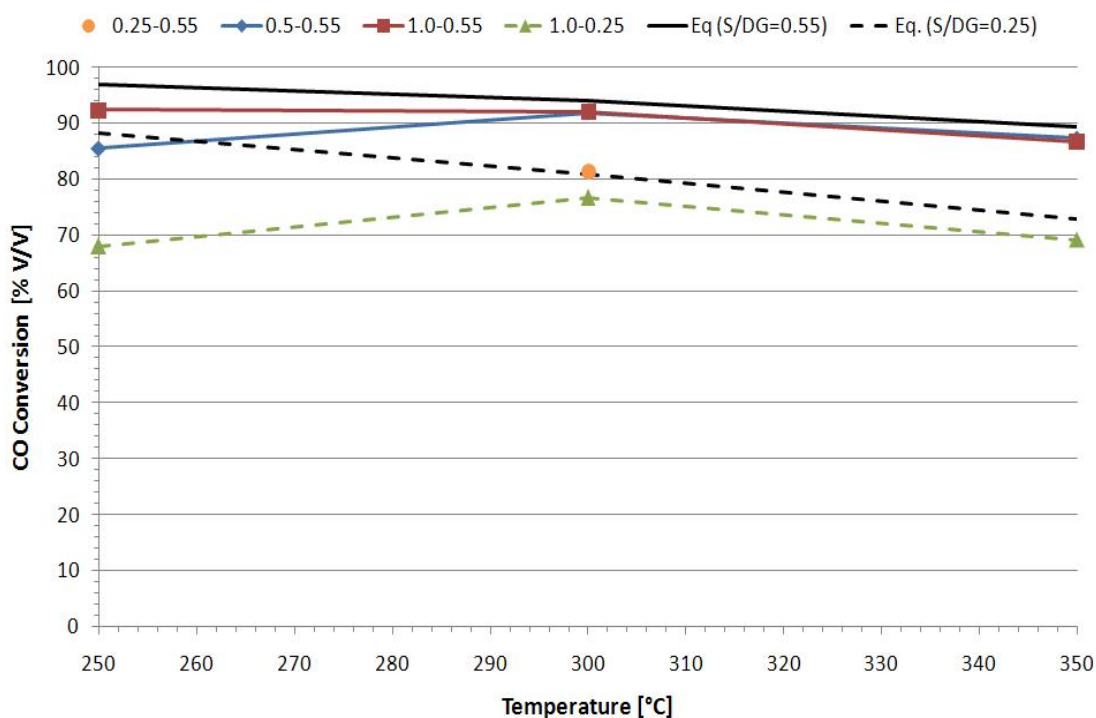

Figure 4.8 CO conversion of ZAC23c at different contact time, S/DG and temperature values.

The catalyst ZAC33c, in which the Cu content is three times higher than that in the first catalyst (ZAC13c), turns down the hypothesis on a further improvement in the catalytic performances at 250 °C with the Cu content (Table 4.4). The sample shows a catalytic activity far from the equilibrium values (Fig. 4.9), and the effects of the S/DG ratio and contact time on the catalytic performances are similar at all the temperatures. At 350 °C, the reduction of the catalytic activity, decreasing the S/DG ratio from 0.55 to 0.25 v/v (τ = 1.00 sec), is more remarkable than in the previous catalysts (from 75 to 57 % of CO conversion). Unlike ZAC13c and ZAC23c, where the CO conversion tends to decrease at higher temperature, the CO conversion of this catalyst achieves the highest value at 350 °C (S/DG = 0.55 v/v; τ = 1.00 sec); being always the activity far from the equilibrium, the temperature affect kinetically the reaction rate.
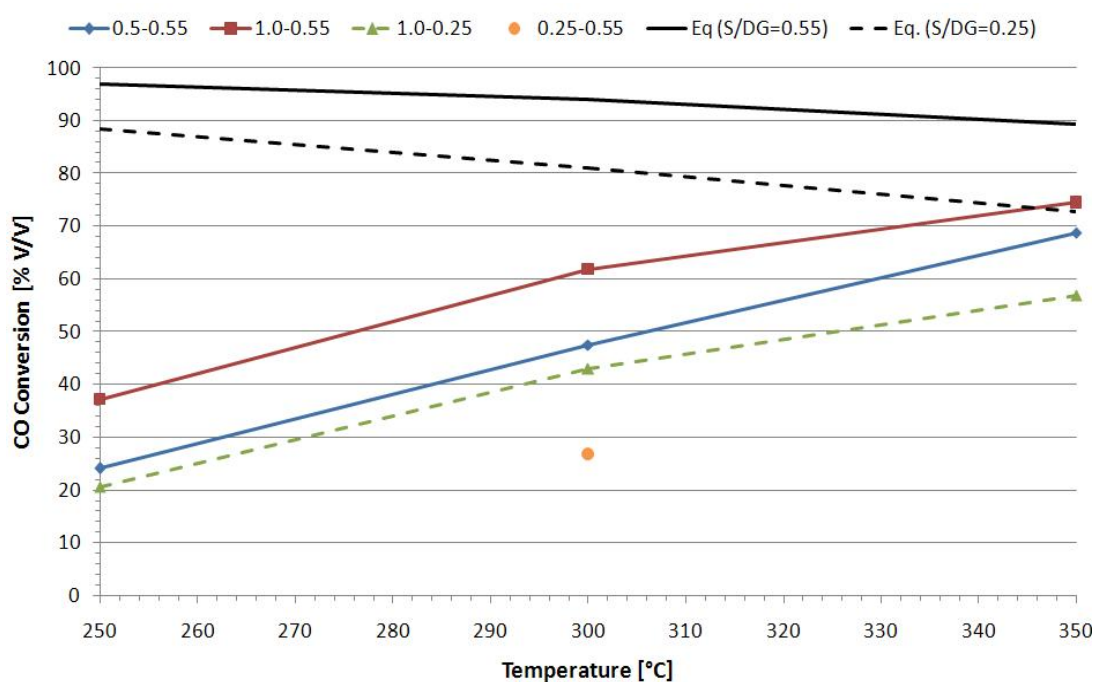

Figure 4.9 CO conversion of ZAC33c at different contact time, S/DG and temperature values.

4.1.3 Stability of the catalysts

The outlet gas composition as a function of the reaction time is an industrial important parameter to evaluate the catalyst stability; therefore, it was studied the deactivation of the catalysts over 100 h at 300 °C, using S/DG of 0.25 v/v and contact time

of 1.0 sec. All the samples exhibit a good stability over the test; as an example, for the ZAC13c, the gas mixture remains constant and closed to the equilibrium value; in fact, after more than 100 h of Time On Stream (TOS), the quantity of CO increases only of about 0.7 % (Fig. 4.10).
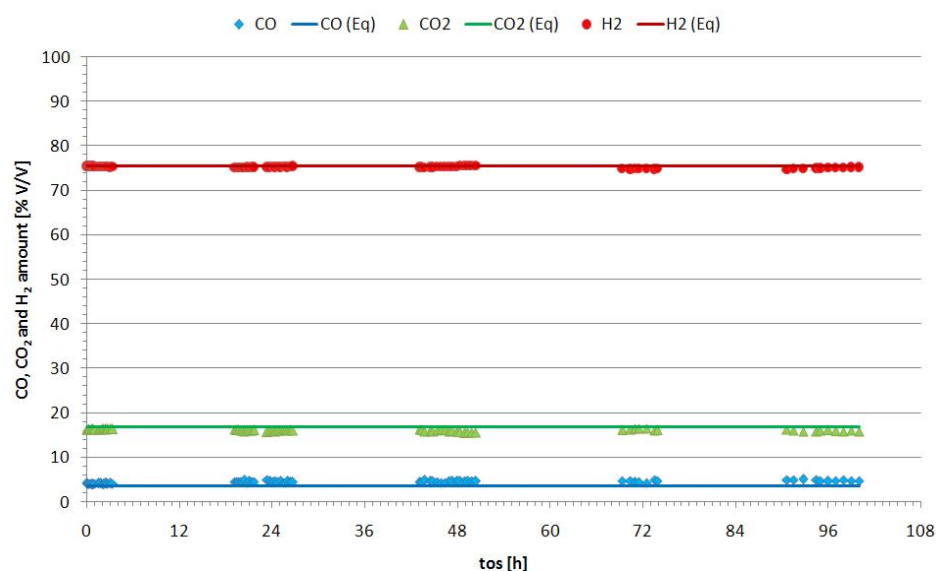

Figure 4.10 Stability of the ZAC13c catalyst (T = 300 °C; P = 15 bar; S/DG = 0.25 v/v; τ= 1.0 sec).

4.1.4 Preliminary conclusions

a)   The BET surface area decreases by increasing the Cu content, both before and after reaction. However, this parameter does not seem critical for the catalytic activity.

b)   The trend of metallic Cu area values (Fig. 4.11) evidences that the catalytic activity does not depend only on this parameter, but also on the synergetic interactions between Cu and ZnO [24], which favors the stabilization of formate-type intermediates by spillover [11,25].

c)   The ZAC23c catalyst represents the best compromise between increase of metallic Cu surface area and decrease of Zn content to maintain constant the M^{II}/M^{III} ratio. A further increase in Cu content worsens the CO conversion, due to the formation of large metallic Cu particles, with a low Cu dispersion, while the lower activity of ZAC13c may be attributed to the smaller metallic Cu area.
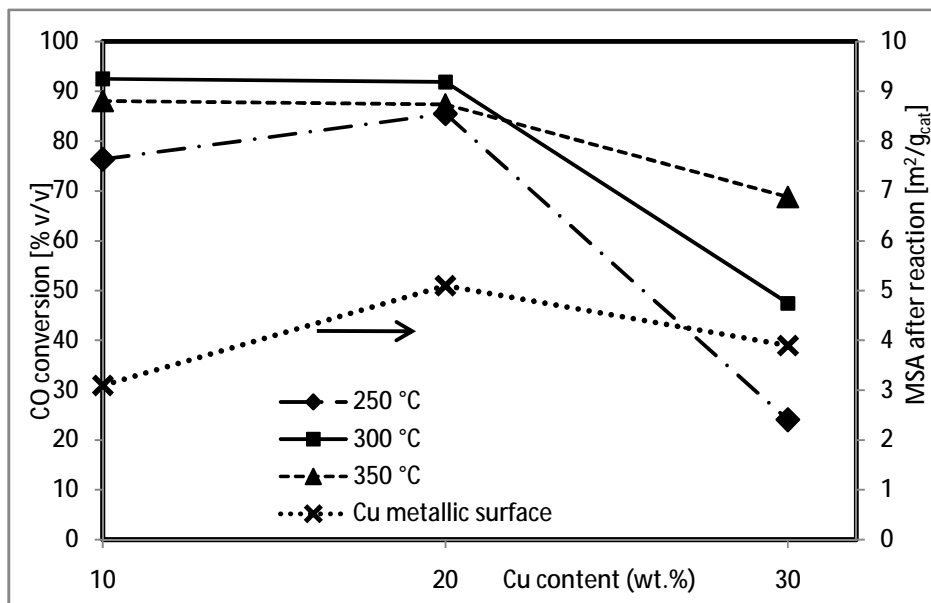
Figure 4.11 Effect of Cu loading on the WGS activity over the Cu/ZnO/Al$_2$O$_3$ catalysts. (Reaction conditions: H$_2$/CO/CH$_4$/CO$_2$ = 72.0/18.8/4.6/4.6 v/v; P = 15 bar; S/DG = 0.55 v/v; contact time = 0.5 sec; T = 250, 300 and 350 °C).

4.2   Role of Al content

4.2.1   Characterization of HT-type precursors and catalysts

Two catalysts with different Al content (25.0 and 33.3 mol % of Al for ZAC23c and ZAC22c, respectively) were prepared starting from HT-type precursors, maintaining the Cu content constant (20 wt.%). The XRD patterns of the precursors (Fig. 4.12) show the presence of a HT-type phase in both samples, while ZnO is observed only for HT-ZAC23c. It is reported that, in the Cu-based HT-type precursor, a Cu^{2+}/M^{II} ratio ≤ 1.00 and a M^{III}/M^{II} ratio in the range 0.20–0.33 are important factors to obtain pure HT-type precursors [9]. Despite that, co-precipitation conditions are critical factors to prepare pure HT-type phases, and may give rise to other phases, such as observed for HT-ZAC23c. The sharp and symmetrical HT-type reflections suggest the presence of well-organized HT-type structure in both samples [9]. After calcination (Fig. 4.13), it may be observed the decomposition of the HT-type precursors to mixed oxides without any presence of segregated Cu-containing species. The broader profile of the calcined HT-ZAC22c suggests a better dispersion of Cu

and ZnO particles than in the sample with lower Al content, in agreement with the smaller particle size (Table 4.5) [21,26]. Moreover, both precursors show similar BET surface area values (Table 4.5), suggesting that this parameter does not significantly depend on M^{II}/M^{III} ratio in the HT-type precursors. The BET surface area of both samples (Table 4.6) increases after calcination [9], with a higher value for the sample obtained from a pure HT-type precursor (ZAC22c).
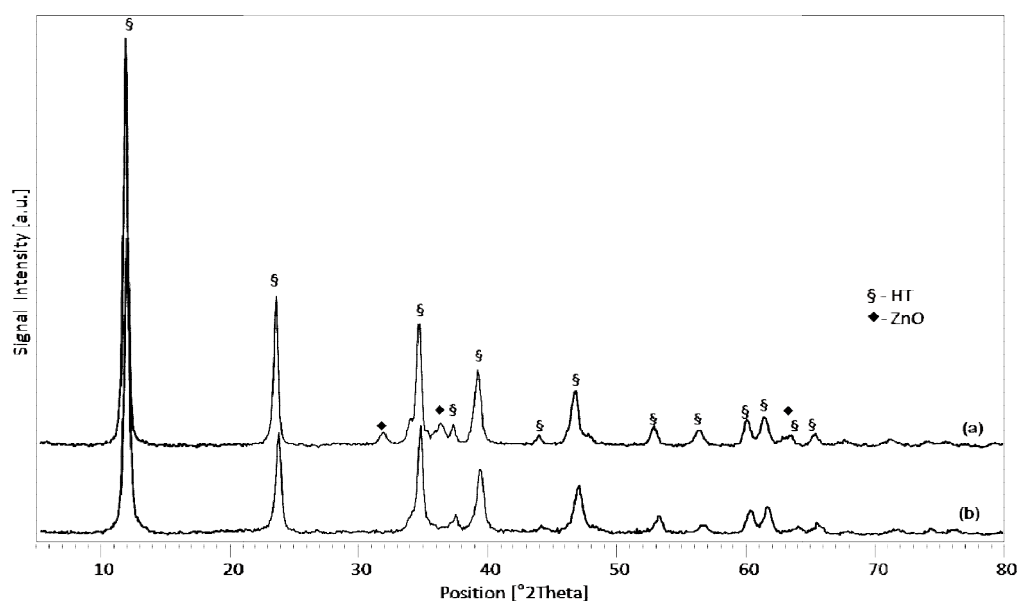

Figure 4.12 XRD patterns of the HT-type precursors: (a): HT-ZAC23c; (b): HT-ZAC22c.

After reaction, both samples show an increase of crystallinity with the presence of metallic Cu, evidencing sintering phenomena during the reaction and a surface passivation of the large Cu^0 particles during the unloading (Fig. 4.13), with more intense Cu metallic and ZnO reflections for ZAC23c. Moreover, the BET surface area values (Table 4.6) of ZAC23c and ZAC22c decrease by about 20-30 % after reaction. Both these results suggest more significant sintering phenomena in ZAC23c than in ZAC22c. The Cu surface area remains practically unchanged after reaction, evidencing that HT-type phases are good precursors to obtain thermally stable Cu-containing species. The higher Cu and BET surface area values for ZAC22c let us hypothesize a high catalytic activity (see next section 4.2.2).
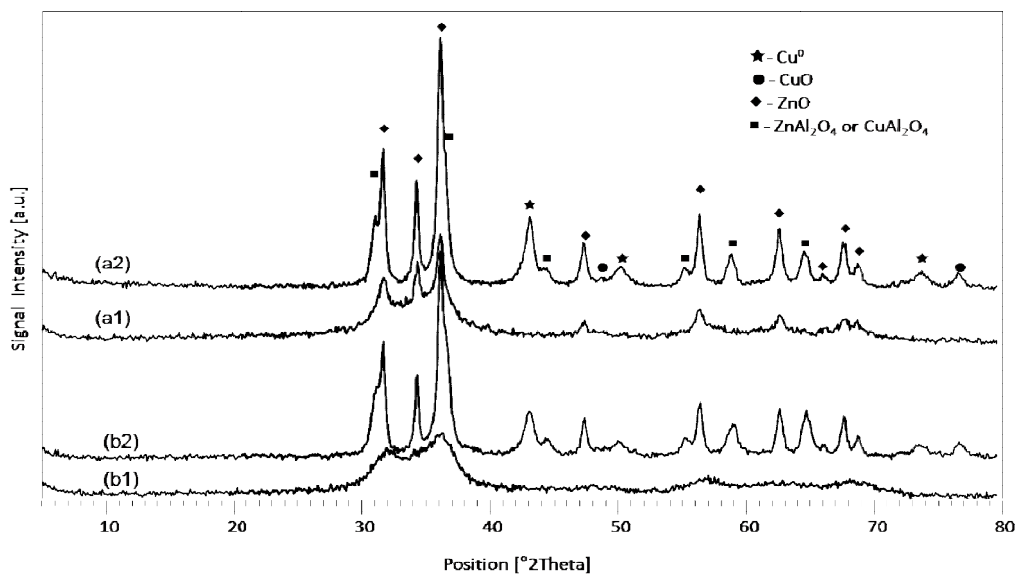
Figure 4.13 XRD patterns of the calcined HT-precursors before and after reaction: (a1): ZAC23c before reaction; (a2): ZAC23c after reaction; (b1): ZAC22c before reaction; (b2): ZAC22c after reaction.

Table 4.5 Characterization of the HT-type precursors.

Sample	M^{II}/M^{III}	Al (mol %)	Phase detected by XRD	$d_{HT}(003)$ (nm)	BET surface area (m^2/g)
HT-ZAC23c	3	25.0	HT and ZnO	33	32
HT-ZAC22c	2	33.3	HT	24	36

Table 4.6 Characterization of the calcined HT-type precursors (before and after reaction).

Sample		Phase detected by XRD	BET surface area (m^2/g)	Cu surface area (m^2/g_{cat})	Cu surface area (m^2/g_{Cu})	D_{Cu} (%)	Pore volume (cm^3/g)	Pore diameter (nm)
ZAC23c	before	ZnO-type	48	4.9	24.5	3.8	0.35	28
	after	ZnO, spinel, CuO (trace), Cu^0	34	5.1	25.5	3.9	0.35	34
ZAC22c	before	ZnO-type	54	7.1	35.5	9.2	0.35	23
	after	ZnO, spinel, CuO (trace), Cu^0	43	6.8	34.0	9.2	0.37	28

Figure 4.14 shows that the pore size distribution of both catalysts before reaction is bimodal, with the first peak at about 3-4 nm and the second one between 30 and 40 nm. After reaction, the smaller pores disappear in both samples, with a decrease of the second peak and a shift towards higher diameters evident only in ZAC23c. The average diameter (Table 4.6) increases in both samples after reaction. These results, together with the decrease of BET surface area after reaction, are due to sintering phenomena and possible structure rearrangement related to Cu reduction. This is confirmed by the XRD patterns (Fig. 4.13), that show more significant sintering phenomena in ZAC23c, which exhibits higher pore diameter and lower BET surface area after reaction. The adsorption isotherms (type IV) and hysteresis loop (type H4) (not shown), together with the pore size distributions, confirm that the catalysts contain mainly mesopores [28].
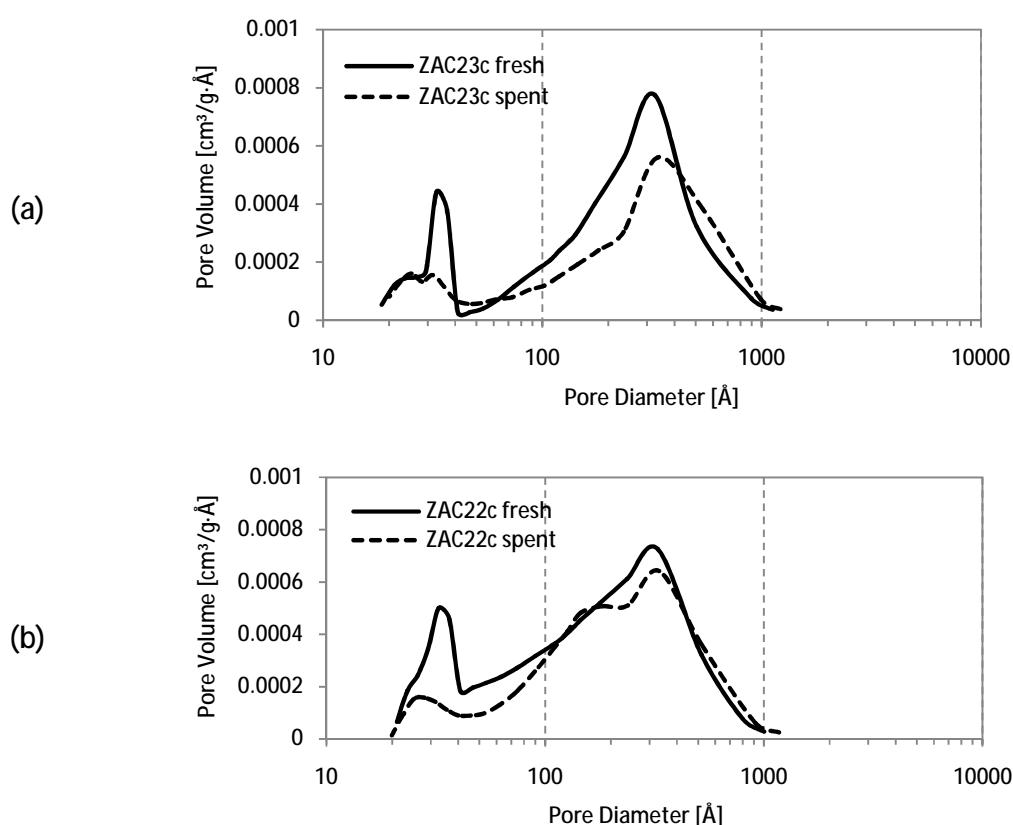
(a)

(b)

Figure 4.14 BJH pore distribution of the calcined HT-type precursors before (fresh) and after (spent) reaction: (a) – ZAC23c; (b) – ZAC22c.

4.2.2 Catalytic activity

The WGS activity data for the catalysts with the same Cu content (20 wt.%) are summarized in Table 4.7. The catalytic performances of ZAC23c were previously reported in section 4.1.2: the CO conversion achieves the equilibrium values at 300 and 350 °C and 1 sec of contact time; the S/DG ratio worsens significantly the catalytic performances only at 250 °C, while the contact time has a low effect. The ZAC22c catalyst (Fig 4.15) exhibits an excellent catalytic activity, achieving the equilibrium values of CO conversion almost at all the temperatures with the higher values of contact time ($\geq$ 0.50 sec). A defect of steam (Fig. 4.16a) has a negative effect on the activity: the CO conversion decreases from 96 to 77 % as the S/DG ratio decreases from 0.55 to 0.25 v/v (τ = 1.00 sec; T =250 °C).

As for ZAC23c, the kinetic factors (Fig. 4.16b) do not seem to influence the catalytic activity: at 300 °C and 0.55 v/v of S/DG, the decrease of the value of contact time to 0.25 sec gives rise only to a small decrease of CO conversion (from 91 to 86 %). The same trends of CO conversion and H_2 yield in all operating conditions, together with the high selectivity in CO_2 ($\geq$ 97 %), confirm that no contribution of side reactions occurs in this catalyst. Compared with the ZAC23c catalyst (Table 4.7), ZAC22c shows a higher catalytic activity at 250 °C, with similar catalytic performances at 300 and 350 °C.
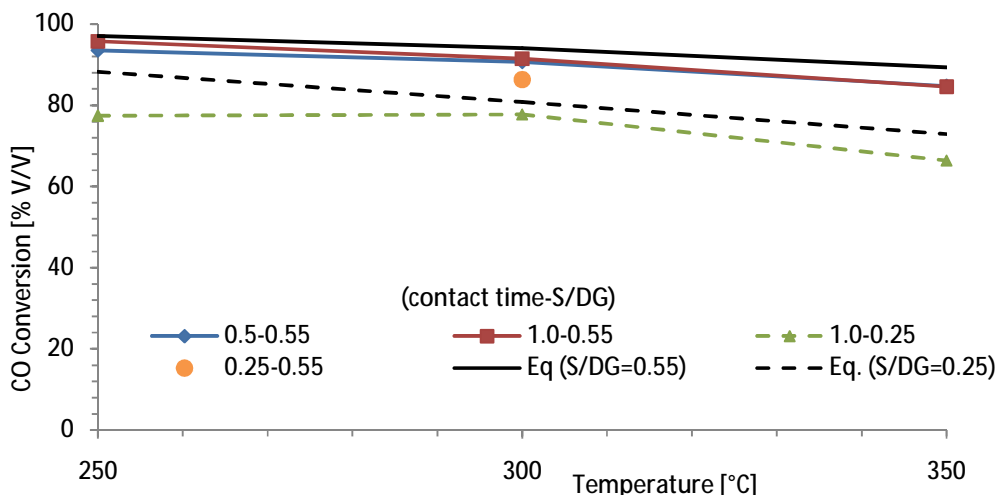

Figure 4.15 CO conversion of ZAC22c at different contact time, S/DG and temperature values.
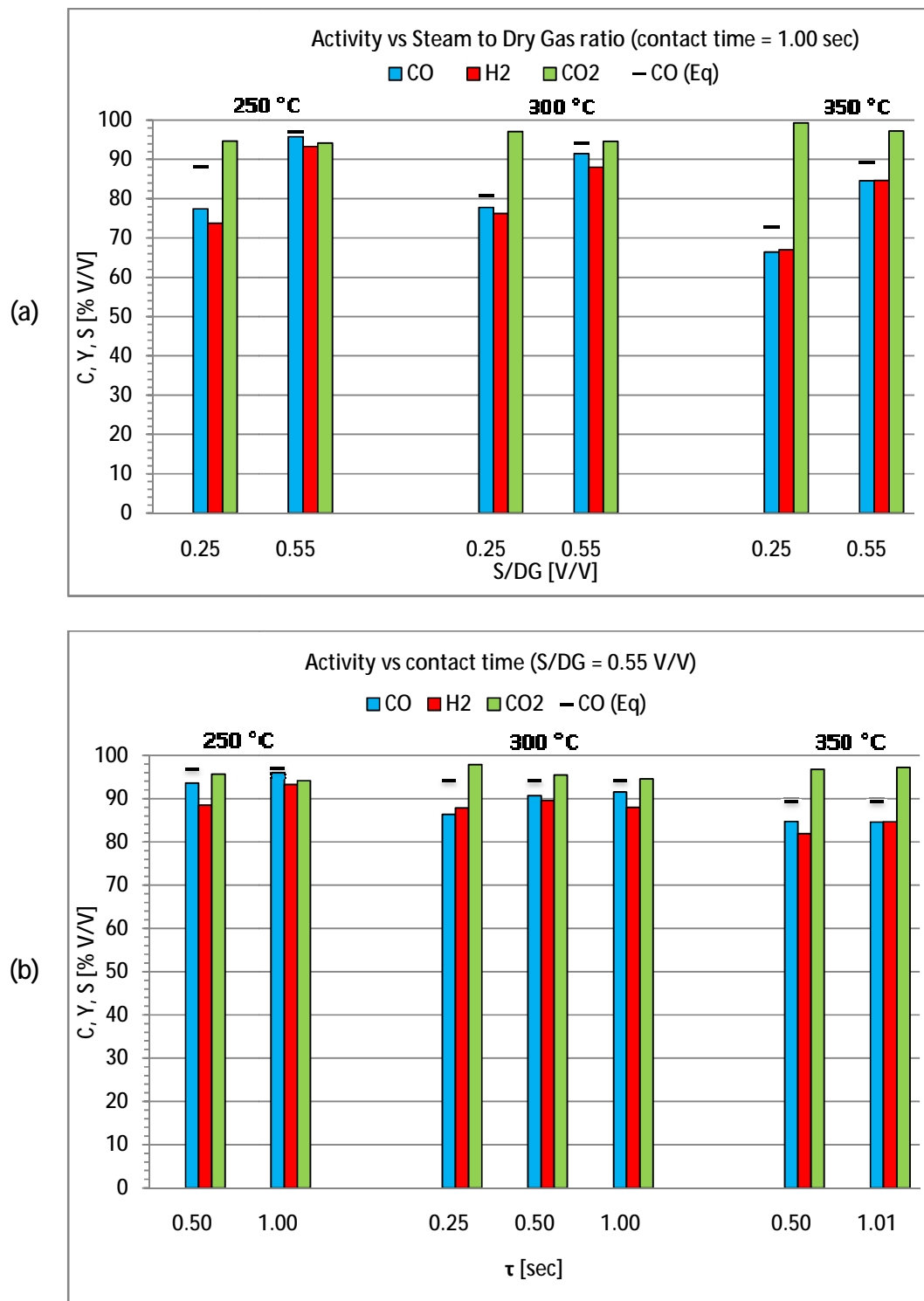
Figure 4.16 Activity of ZAC22c as a function of S/DG (a) and contact time (b) values.

Table 4.7 CO conversion and H_2 yield for the catalysts with different Al content.

	T	[°C]	250	250	250	300	300	300	300	350	350	350
	S/DG	[V/V]	0.55	0.25	0.55	0.55	0.55	0.25	0.55	0.55	0.25	0.55
	τ	[sec]	0.50	1.00	1.00	0.25	0.50	1.00	1.00	0.50	1.00	1.00
ZAC23c	CO Conv.	[%]	86	68	92	82	92	77	92	87	69	87
	H_2 Yield	[%]	86	67	86	80	91	74	92	80	67	84
ZAC22c	CO Conv.	[%]	94	77	96	86	91	78	92	85	66	85
	H_2 Yield	[%]	89	74	93	88	90	76	88	82	67	85

4.2.3 Preliminary conclusions

a) Increasing Al content results in an increase of the purity of HT-type precursor, enhancing the Cu dispersion in the calcined catalyst [1,10], and giving rise to the superior catalytic performances for ZAC22c, mainly at 250 °C (Fig. 4.17), while at higher temperatures, the CO conversion achieves the equilibrium values for both samples.

b) Synergetic interactions of Cu with ZnO and spinel favor the Cu dispersion during reaction and the resistance to the sintering [10,27]. The sample ZAC22c represents the best compromise between Zn and Al contents to obtain high activity also at low temperature, improving the stability at the middle temperature.
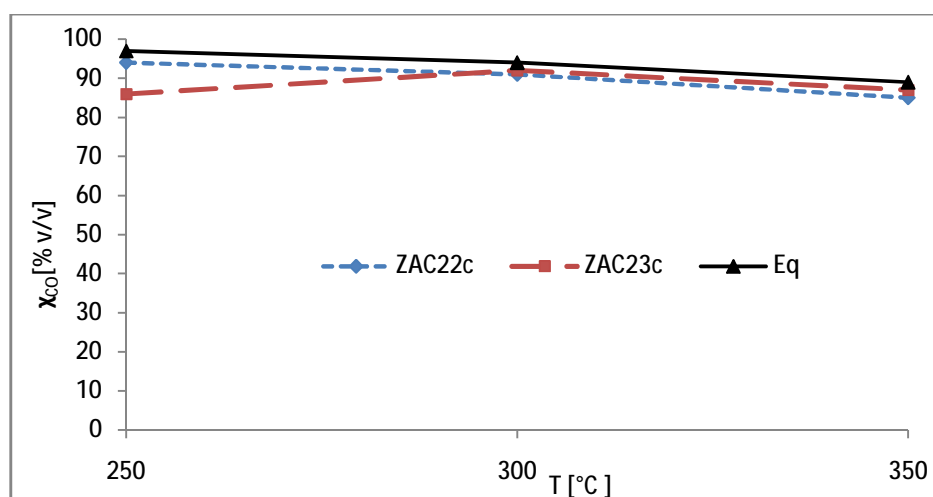

Figure 4.17 CO conversion (χ_{CO}) with temperature. (Reaction conditions: $H_2/CO/CH_4/CO_2$ = 72.0/18.8/4.6/4.6 v/v; P = 15 bar; S/DG = 0.55 v/v; contact time = 0.50 sec).

4.3   Role of ZnO

4.3.1   Characterization of HT-type precursors and catalysts

In order to confirm the role of ZnO, the sample ZAC23cM1 was prepared as the ZAC23c one, but replacing most of Zn in the HT-type precursor by Mg, which is reported as a good stabilizer, but not active in the WGS reaction [13,29].

The XRD patterns of two dried precipitates (HT-ZAC23c and HT-ZAC23cM1) (Fig. 4.18) show the presence of a HT-type phase in both samples, while the ZnO reflections are observed only for HT-ZAC23c, may be due to a change of the preparation conditions, which results in a different purity of the phases as previously reported in section 4.2. The broader profile of HT-ZAC23cM1 indicates a lower crystallinity than in HT-ZAC23c, which may be related to structural changes due to the partial replacement of Zn^{2+} by Mg^{2+} cations in the HT-type structure. The introduction of Mg significantly increases the BET surface area of the HT-type precursor (Table 4.8), and reduces the average crystal size by about five times. After calcination, the HT-type precursors decompose to mixed oxides in both samples (Fig. 4.19); ZnO-type phase is observed only for ZAC23c, while ZAC23cM1 presents quasi-amorphous mixed oxide phase, suggesting that the introduction of Mg significantly improves particle dispersion of both precursor and calcined sample [30].
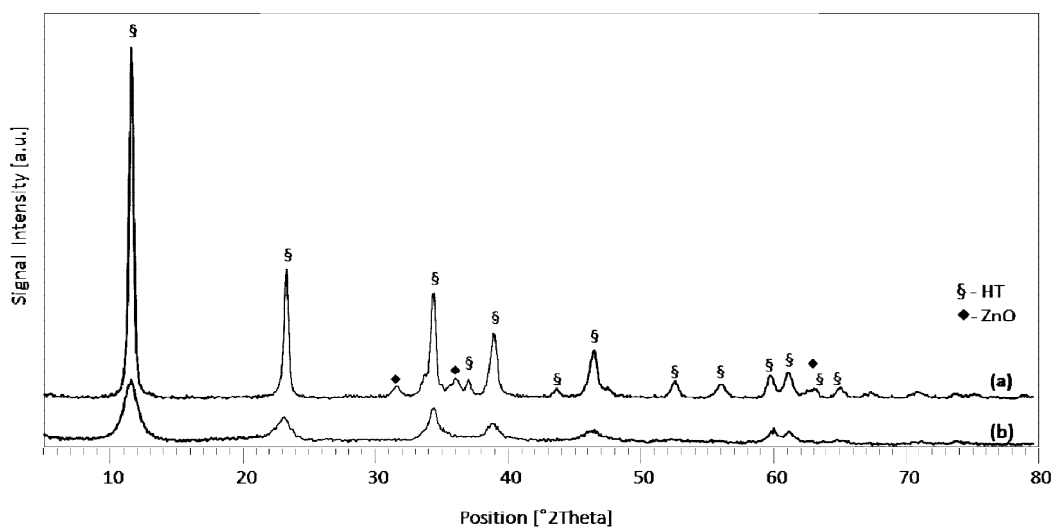

Figure 4.18 XRD patterns of the HT-type precursors: (a): HT-ZAC23c; (b): HT-ZAC23cM1.

Table 4.8 Characterization of the HT-type precursors.

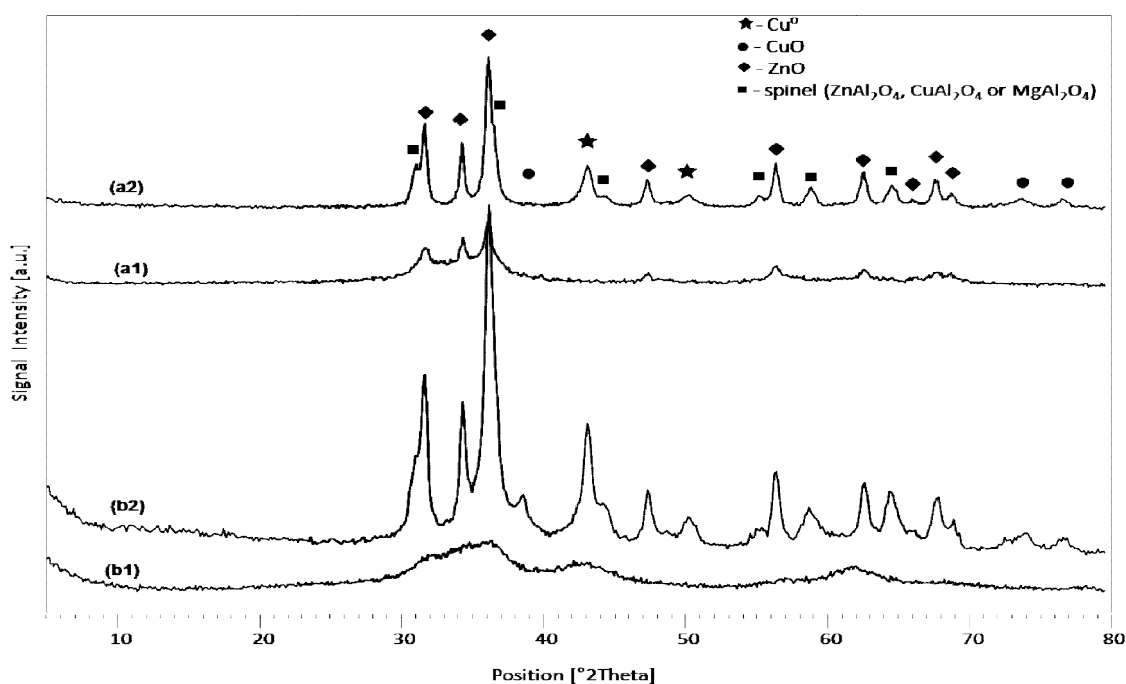| Sample	Zn/Mg (at. ratio)	Phase detected by XRD	$d_{HT}(003)$ (nm)	BET surface area (m^2/g)
HT-ZAC23c	–	HT and ZnO	33	32
HT-ZAC23cM1	1	HT	7	128

Figure 4.19 XRD patterns of the calcined HT-type precursors before and after reaction: (a1): ZAC23c before reaction; (a2): ZAC23c after reaction; (b1): ZAC23cM1 before reaction; (b2): ZAC23cM1 after reaction.

After reaction, both samples show the further presence of metallic Cu (Fig. 4.19), evidencing sintering phenomena during the reaction and a surface passivation of large Cu^0 particles during the unloading. The BET and Cu surface area values of ZAC23cM1 (Table 4.9) are about three times higher than those of the sample without Mg before reaction, although a drastic decrease of 60-80 % occurs after reaction. It seems that the introduction of Mg enhances significantly the dispersion and the surface area before reaction, although the catalyst is prone to sintering and phase segregation during

reaction. On the contrary, Cu dispersion and surface area of ZAC23c remain almost unchanged after reaction, suggesting that ZnO improves the thermal resistance of the catalyst [10,27].

Table 4.9 Characterization of the calcined HT-type precursors (before and after reaction).

Sample		Phase detected by XRD	BET surface area (m^2/g)	Cu surface area (m^2/g_{cat})	Cu surface area (m^2/g_{Cu})	D_{Cu} (%)	Pore volume (cm^3/g)	Pore diameter (nm)
ZAC23c	before	ZnO-type	48	4.9	24.5	3.8	0.35	28
	after	ZnO, spinel, CuO (trace), Cu^0	34	5.1	25.5	3.9	0.35	34
ZAC23cM1	before	mixed oxides	138	13.8	68.9	10.6	0.46	9
	after	ZnO, spinel, CuO (trace), Cu^0	52	3.0	15.1	2.3	0.29	16

The pore size distribution of ZAC23cM1 before reaction (Fig. 4.20) is bimodal, with mainly 7-10 nm pores and a small peak around 3-4 nm, showing that Mg promotes an uniform distribution of pores. After reaction, the 3-4 nm pores remain practically unchanged, while the 7-10 nm ones diminish and shift towards higher diameters. While the average pore diameter increases, the total pore volume decreases after reaction (Table 4.9), suggesting a partial collapse of smaller pores with formation of larger ones and consequent decrease of the surface area. The decrease of porosity parameters after reaction is more pronounced in ZAC23cM1 than in ZAC23c, suggesting that the pore structure is more fragile in the sample with Mg. The pore size distributions, together with the adsorption isotherms (type IV) and hysteresis loop (type H4) (not shown), indicate the mesoporous structure of both catalysts [28].
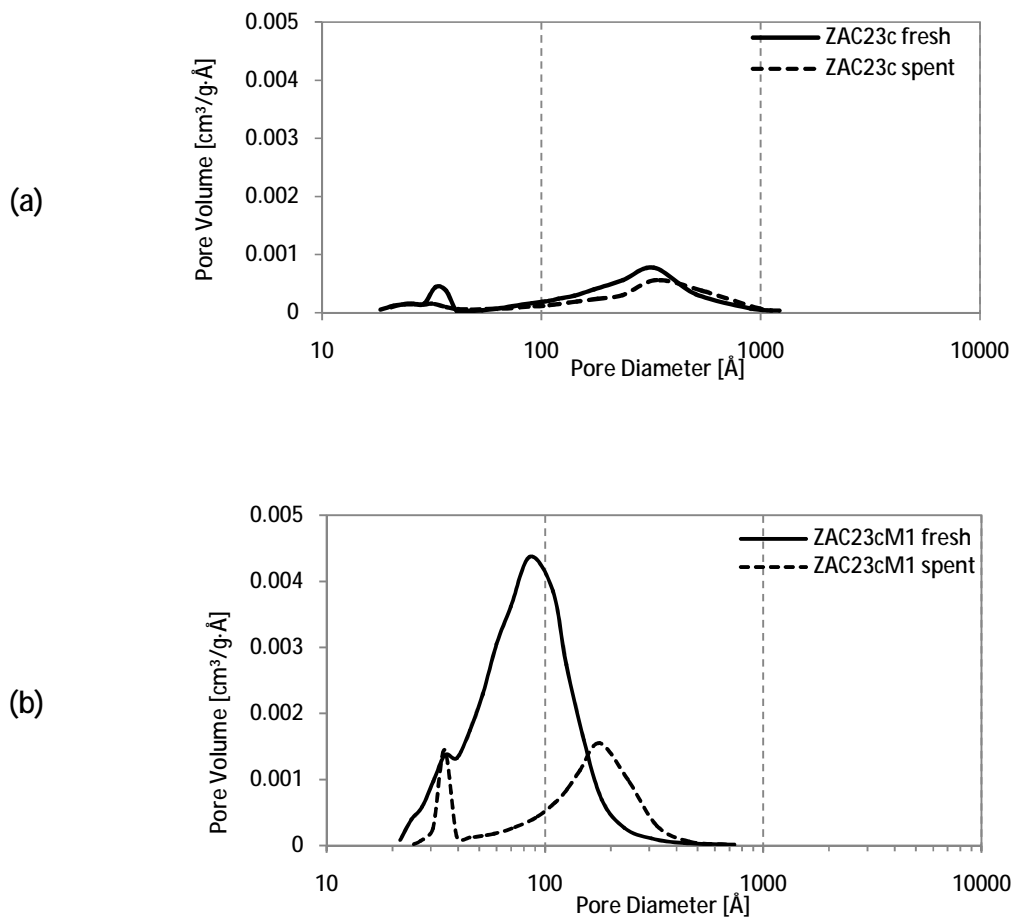
Figure 4.20 BJH pore distribution of the calcined HT-type precursors before (fresh) and after (spent) reaction: (a) - ZAC23c; (b) - ZAC23cM1.

4.3.2 Catalytic activity

The activity data are summarized in Table 4.10, in which for sake of comparison also the data for ZAC23c are reported. The ZAC23cM1 catalyst shows poor catalytic performances at all temperatures, with the CO conversion values far away from the equilibrium values (Fig. 4.21). With a contact time of 1 sec and S/DG of 0.55 v/v, the activity varies unusually with the temperature: the CO conversion drastically decreases by about 50 % as the temperature increases from 250 to 300 °C, while a further increase of temperature enhances the CO conversion.

The excess of steam affects the catalytic activity of ZAC23cM1 differently at each temperature (Fig. 4.22a): at 250 °C, moving S/DG ratio from 0.25 to 0.55 v/v (τ = 1 sec) increases the CO conversion by about two times, while at 300 °C the excess of steam worsens the CO conversion; finally at 350 °C, the CO conversion is almost constant (≈70 %). The catalytic performances of ZAC23cM1 are sensitive also to changes of the contact time (Fig. 4.22b): increasing the contact time from 0.50 to 1.00 sec (S/DG = 0.55 v/v), the CO conversion increases from 74 to 83 % at 250 °C, while at 300 °C a remarkable reduction of CO conversion may be observed; at 350 °C, again the contact time positively affects the CO conversion, which increases by 25 % ca. A high CO_2 selectivity (≥ 97 %), together the same trends of CO conversion and H_2 yield , suggests that side reactions are almost absent.
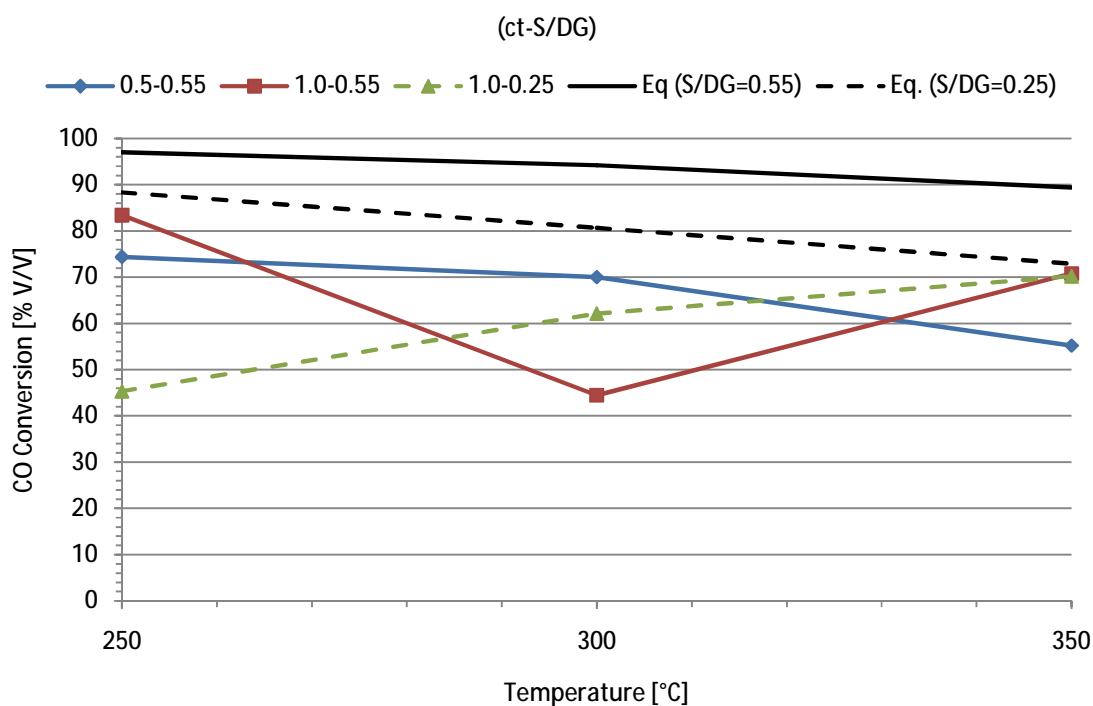

Figure 4.21 CO conversion of ZAC23cM1 at different contact time, S/DG and temperature values.
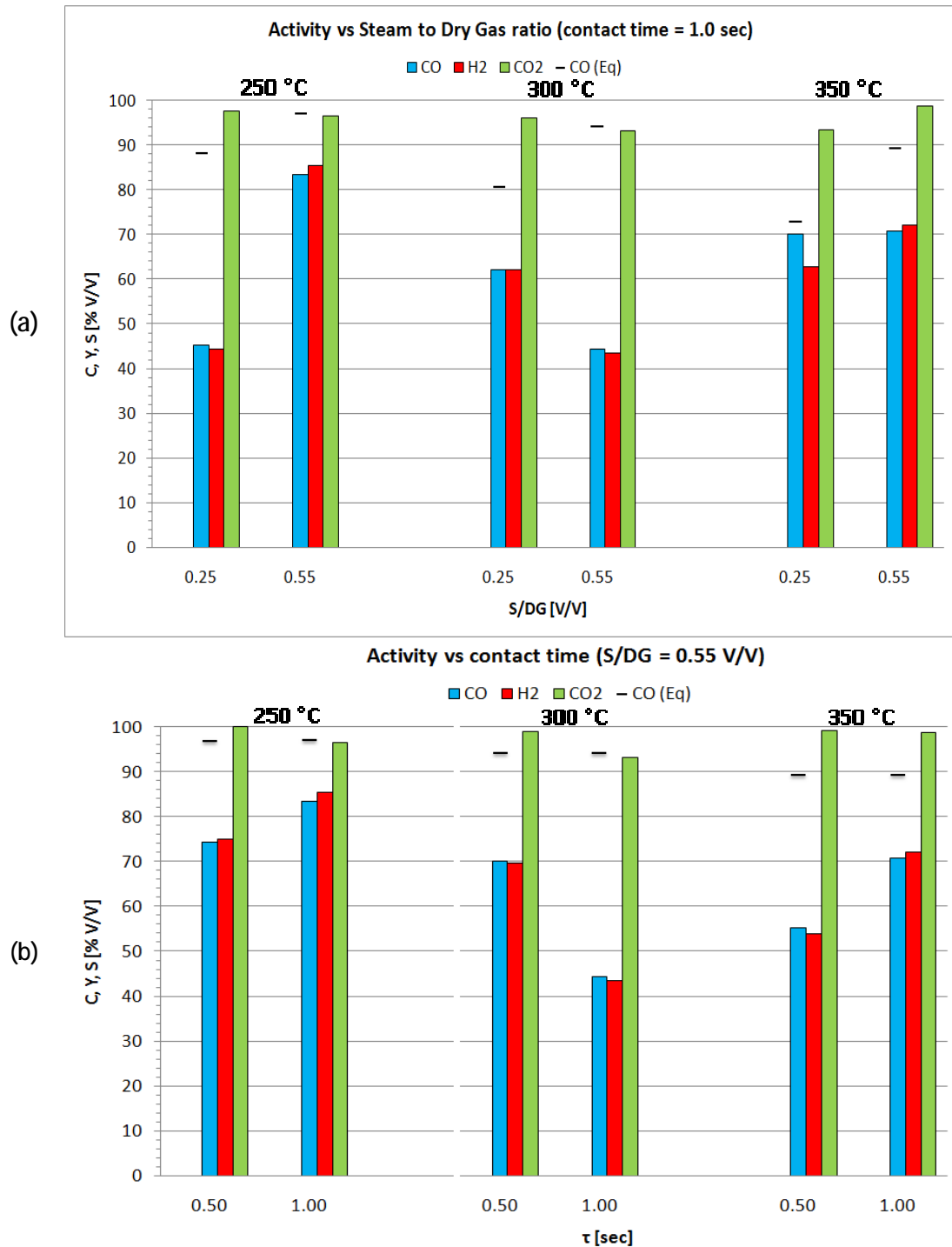
Figure 4.22 Activity of ZAC23cM1 as a function of S/DG (a) and contact time (b) values.

Table 4.10 CO conversion and H_2 yield for the catalysts with different Al contents.

	T	[°C]	250	250	250	300	300	300	350	350	350
	S/DG	[V/V]	0.55	0.25	0.55	0.55	0.25	0.55	0.55	0.25	0.55
	τ	[sec]	0.50	1.00	1.00	0.50	1.00	1.00	0.50	1.00	1.00
ZAC23c	CO Conv.	[%]	86	68	92	92	77	92	87	69	87
	H_2 Yield	[%]	86	67	86	91	74	92	80	67	84
ZAC23cM1	CO Conv.	[%]	74	45	83	70	62	44	55	70	71
	H_2 Yield	[%]	75	44	86	70	62	44	54	63	72

4.3.3 Preliminary conclusions

Substitution of 50 % (at. ratio) Zn by Mg enhances significantly the physical properties (Table 4.9), while worsens the catalytic performances, compared to those of the sample without Mg (Fig. 4.23). This result confirms that ZnO plays important role on the catalytic performances, improving the activity and stability by means of synergetic interactions with Cu. These effects are more and more significant by increasing the reaction temperature and may be attributed to the lower stability of the Mg-containing sample.
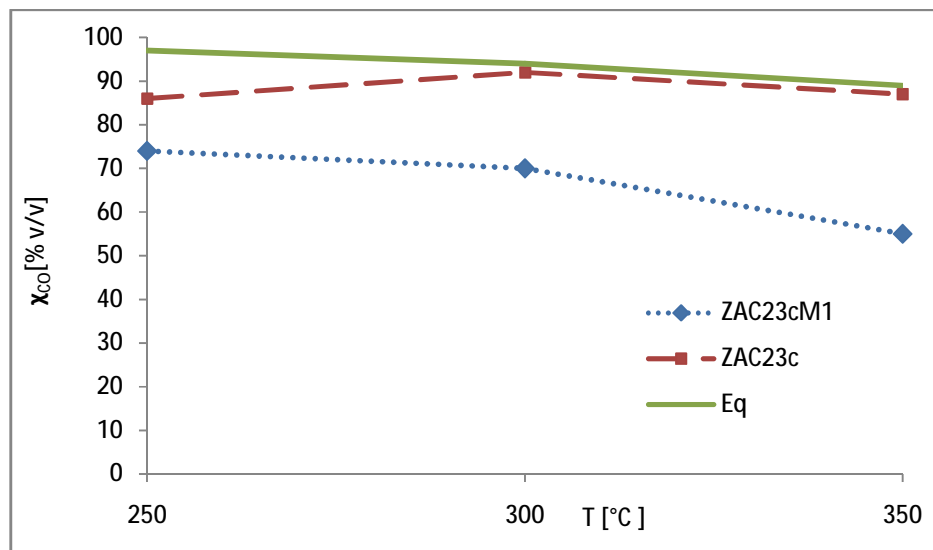

Figure 4.23 CO conversion (χ_{CO}) with temperature. (Reaction conditions: $H_2/CO/CH_4/CO_2$ = 72.0/18.8/4.6/4.6 v/v; P = 15 bar; S/DG = 0.55 v/v; contact time = 0.50 sec).

References

[1]   M.J.L. Ginés, N. Amadeo, M. Laborde, C.R. Apesteguía, *Appl. Catal.* A 131 (1995) 283.

[2]   R.G. Herman, K. Klier, G.W. Simmons, B.P. Finn, J.B. Bulko, *J. Catal.* 56 (1979) 407.

[3]   T. Shido, Y. Iwasawa, *J. Catal.* 129 (1991) 343.

[4]   J.C. Frost, *Nature* 334 (1988) 577.

[5]   J.A. Rodriguez, P. Liu, J. Hrbek, J. Evans, M. Perez, *Angew. Chem. Int. Ed.* 46 (2007) 1329.

[6]   J.B. Park, J. Graciani, J. Evans, D. Stacchiola, S.D. Senanayake, L. Barrio, P. Liu, J.F. Sanz, J. Hrbek, J.A. Rodriguez, *J. Am. Chem. Soc.* 132 (2010) 356.

[7]   P.V.D.S. Gunawardana, H.C. Lee, D.H. Kim, *Int. J. Hydr. En.* 34 (2009) 1336.

[8]   K. Sekizawa, S.-Ichi Yano, K. Eguchi, H. Arai, *Appl. Catal.* A 169 (1998) 291.

[9]   F. Cavani, F. Trifirò, A. Vaccari, *Catal. Today* 11 (1991) 173.

[10]   M.M.V.M. Souza, K.A. Ferreira, O. R. de Macedo Neto, N.F.P. Ribeiro, M. Schmal, *Catal. Today* 133–135 (2008) 750.

[11]   W. Fu, Z. Bao, W. Ding, K. Chou, Q. Li, *Catal. Comm.* 12 (2011) 505

[12]   F. Basile, A. Vaccari, in *Layered Double Hydroxides: Present and Future (V. Rives Ed.),* Nova Science, New York (USA), 2001.

[13]   K. Nishida, D. Li, Y. Zhan, T. Shishido, Y. Oumi, T. Sano, K. Takehira, *Appl. Clay Sci.* 44 (2009) 211

[14]   Y. Okamoto, K. Fukino, T. Imanaka, S. Teranishi, *J. Phys. Chem.* 87 (1983) 3740.

[15]   W.R.A.M. Robinson, J.C. Mol, *Appl. Catal.* 60 (1990) 61.

[16]   G.L. Castiglioni, A. Vaccari, G. Fierro, M. Inversi, M. Lo Jacono, G. Minelli, I. Pettiti, P. Porta, M.Gazzano, *Appl. Catal.* 123 (1995) 123.

[17]   J. Als-Nielsen, G. Grübel, B.S. Clausen, *Nucl. Instr. Meth. Phys. Res.* B 97 (1995) 522.

[18]   T.L. Reitz, P.L. Lee, K.F. Czaplewski, J.C. Lang, K.E. Popp, H.H. Kung, *J. Catal.* 199 (2001) 193.

[19]   H.P. Klug, L.E. Alexander, *X-Ray Diffraction Procedures*, Wiley, New York (USA), 1974.

[20]   I. Melian-Cabrera, M.L. Granados, J.L.G. Fierro, *J. Catal.* 210 (2002) 273.

[21]   T. Shishido, M. Yamamoto, D. Li, Y. Tian, H. Morioka, M. Honda, T. Sano, K. Takehira, *Appl. Catat.* A 303 (2006) 62.

[22]   R.T. Figueiredo, A.L.D. Ramos, H.M.C. Andrade, J.L.G. Fierro, *Catal. Today* 107–108 (2005) 671.

[23]   M. Ferrandon, E. Bjornbom, *J. Catal.* 200 (2001) 148.

[24]   S. Gusi, F. Trifirò, A. Vaccari, G. Del Piero, *J. Catal.* 94 (1985) 120.

[25]   J.M. Campbell, J. Nakamura, C.T. Campbell, *J. Catal.* 136 (1992) 24.

[26]   I. Atake, K. Nishida, D. Li, T. Shishido, Y. Oumi, T. Sano, K. Takehira, *J. Mol. Catal. A: Chemical* 275 (2007) 130.

[27]   E.M. Fuentes, A.C.F. Júnior, T.F. Silva, J.M. Assaf, , M.C. Rangel, *Catal. Today* 171 (2011) 290.

[28]   IUPAC Reporting physisorption data for gas/solid systems, *Pure Appl. Chem.* 57 (1985) 603.

[29] T. Shishido, M. Yamamoto, I. Atake, D. Li, Y. Tian, H. Morioka, M. Honda, T. Sano, K. Takehira, *J. Mol. Catal. A: Chemical* 253 (2006) 270.

[30] Z. Ni, A. Chen, C. Fang, L. Wang, W. Yu, *J. Phys. Chem. Solids* 70 (2009) 632.

5. Conclusions

The catalysts prepared starting from HT-type precursors show good homogeneity and high values of physical properties, which worsen by increasing the Cu content. Among the catalysts with different Cu contents, the ZAC23c catalyst, with 20 wt.% of Cu, represents the best compromise to obtain high catalytic activity and stability. In fact, the catalytic performances depend on both metallic Cu surface area and synergetic interactions between Cu and ZnO

The increase of the Al content enhances the homogeneity of the precursors, leading to a higher Cu dispersion and consequent better catalytic performances. The ZAC22c catalyst, with 20 wt.% of Cu and a molar ratio M^{II}/M^{III} of 2, shows a high activity also at 250 °C and a good stability at middle temperature. It may be considered an optimum catalyst for the WGS reaction at middle temperature (about 300 °C).

By replacing 50 % (at. ratio) of Zn by Mg (which is not active in the WGS reaction), better physical properties were observed, although associate with poor catalytic performances. This result confirms the important role of ZnO on the catalytic performances, favoring synergetic interactions with metallic Cu.

Acknowledgements